DESIGN AND ANALYSIS OF THREE-DIMENSIONAL PHONONIC BAND GAP STRUCTURES WITH EMBEDDED INERTIAL AMPLIFICATION MECHANISMS

by

Semih TANIKER

B.S., Mechanical Engineering, Boğaziçi University, 2008

M.S., Mechanical Engineering, Boğaziçi University, 2011

Submitted to the Institute for Graduate Studies in
Science and Engineering in partial fulfillment of
the requirements for the degree of
Doctor of Philosophy

Graduate Program in
Boğaziçi University
2015

DESIGN AND ANALYSIS OF THREE-DIMENSIONAL PHONONIC BAND GAP STRUCTURES WITH EMBEDDED INERTIAL AMPLIFICATION MECHANISMS

APPROVED BY:

Assoc. Prof. Çetin Yılmaz (Thesis Supervisor)	.....
Prof. Çağatay Başdoğan	.....
Assist. Prof. Halil İbrahim Baştürk	.....
Assist. Prof. Evren Samur	.....
Assoc. Prof. Arda Deniz Yalçınkaya	.....

DATE OF APPROVAL: 03.06.2015

ACKNOWLEDGEMENTS

I would like to thank Assoc. Prof. Çetin Yılmaz for all the help and support. I feel lucky for being one of his students.

I would like to thank Prof. Çağatay Başdoğan, Assist. Prof. Halil İbrahim Baştürk, Assist. Prof. Evren Samur and Assoc. Prof. Arda Deniz Yalçınkaya for participating in my thesis committee.

I would like to thank the assistants and colleagues at the Mechanical Engineering Department of Boğaziçi University.

Finally, I would like to thank my family for their support.

This work was supported by TUBITAK Grant No. 110M663.

ABSTRACT

DESIGN AND ANALYSIS OF THREE-DIMENSIONAL PHONONIC BAND GAP STRUCTURES WITH EMBEDDED INERTIAL AMPLIFICATION MECHANISMS

In this study, three-dimensional (3D) phononic band gap structures are investigated. First, infinite and finite periodic simple cubic, body centered cubic and face centered cubic lattices with and without inertial amplification mechanisms are considered. These 3D lattices are modeled with mass and spring elements that are parametrically varied to observe their effects on band gap (stop band) limits. When inertial amplification mechanisms are used in the infinite periodic lattices, wide low frequency band gaps are generated. Moreover, wide and deep phononic gaps are obtained by using moderate amount of unit cells in the case of finite periodic lattices. Then, 3D phononic band gap structures are formed using distributed parameter inertial amplification mechanisms. The resonance and antiresonance frequencies that characterize the first vibration stop band of the building block mechanism are obtained analytically and by finite element method. The mechanism is optimized to yield wide vibration stop bands in an octahedron and a 2×3 array of octahedrons. Furthermore, these structures are manufactured using a 3D polymer printer and their experimental frequency responses are obtained. Structural damping is added to the finite element model in order to match the resonant peak magnitudes of the numerical and experimental frequency response results. Moreover, a new inertial amplification mechanism is designed by adding constraining beams that reduce the degree of freedom of the initial mechanism. Consequently, ultra wide band gaps at low frequencies are attained. To sum up, it is demonstrated that the 3D structures built with inertial amplification mechanisms are capable of isolating excitations in longitudinal and two transverse directions in a very wide frequency range.

ÖZET

ATALET ARTIRIM MEKANİZMASI GÖMÜLÜ ÜÇ BOYUTLU FONON BANT ARALIĞI YAPILARININ TASARIMI VE İNCELENMESİ

Bu çalışmada, üç-boyutlu fonon bant aralığı yapıları incelenmektedir. İlk olarak, sonsuz ve sonlu periyodik basit kübik, gövde merkezli kübik ve yüzey merkezli kübik kristal kafesler, atalet artırım mekanizmaları ile ve bunlar olmadan incelenmiştir. Bu üç-boyutlu kafes yapılar, bant aralığı (söndürme bandı) üzerindeki etkilerini görebilmek için parametreleri değiştirilebilen kütle ve yay elemanlar kullanılarak modellenmiştir. Atalet artırım mekanizmaları sonsuz periyodik kafes yapılarda kullanıldığında geniş ve düşük frekanslı bant aralığı oluşturulmuştur. Dahası, makul sayıda birim hücre kullanılarak sonlu periyodik yapılar oluşturulduğunda da derin ve geniş fonon bant aralıkları elde edilmiştir. Daha sonra, üç-boyutlu fonon bant aralığı yapıları dağıtık parametreli atalet artırım mekanizmaları kullanılarak oluşturulmuştur. Yapı taşı mekanizmaların, ilk titreşim söndürme bandının özelliklerini tanımlayan rezonans ve antirezonans frekansları analitik olarak ve sonlu elemanlar yöntemi kullanılarak elde edilmiştir. Bu mekanizma sekizyüzlü ve 2×3 sekizyüzlü dizgide geniş titreşim bant aralığı vermesi için optimize edilmiştir. Üstelik bu yapılar üç-boyutlu polimer yazıcılar kullanılarak üretilmiş ve deneysel frekans yanıtları elde edilmiştir. Sayısal ve deneysel frekans yanıtı sonuçlarındaki rezonans tepe değerlerini eşleştirmek için sonlu elemanlar modeline yapısal sönümleme eklenmiştir. Dahası, ilk mekanizmanın serbestlik derecesini azaltan kısıtlayıcı kirişler eklenerek yeni bir atalet artırım mekanizması tasarlanmıştır. Bunun sonucunda düşük frekanslarda çok geniş bant aralığı elde edilmiştir. Özetleyecek olursak, atalet artırım mekanizmaları ile oluşturulan üç-boyutlu yapıların, çok geniş frekans aralığında, boyuna ve iki enine yöndeki tahrikleri engelleyebildiği gösterilmiştir.

TABLE OF CONTENTS

ACKNOWLEDGEMENTS . . . iii
ABSTRACT . . . iv
ÖZET . . . v
LIST OF FIGURES . . . viii
LIST OF TABLES . . . xvii
LIST OF SYMBOLS . . . xviii
LIST OF ACRONYMS/ABBREVIATIONS . . . xix
1. INTRODUCTION . . . 1
1.1. Band Gap Generation Methods . . . 1
1.1.1. Bragg Scattering . . . 2
1.1.2. Local Resonance . . . 2
1.1.3. Inertial Amplification . . . 3
1.2. Types of Periodic Lattices . . . 5
1.2.1. 2D Periodic Lattices . . . 5
1.2.2. Cubic Lattices . . . 8
1.2.3. Truss Structures . . . 10
1.3. Contributions of This Ph.D. Thesis . . . 11
1.4. Applications . . . 12
1.5. Organization of Thesis . . . 12
2. THEORY . . . 13
2.1. Bloch Theorem . . . 13
2.2. 1D Periodic Lattice with Uniform Masses and Springs . . . 14
2.3. 1D Periodic Lattice with Varying Masses and Uniform Springs . . . 15
2.4. Dispersion Relation . . . 16
2.5. Reciprocal Lattice . . . 17
2.6. Inertial Amplification Mechanism . . . 19
2.7. Normalized Bandwidth . . . 21
3. DESIGN AND ANALYSIS OF 3D LUMPED PARAMETER MODELS . . . 22
3.1. SC Lattice . . . 22

3.2. SC Lattice with Inertial Amplification Mechanism 24
3.3. BCC Lattice 28
3.4. BCC Lattice with Inertial Amplification Mechanism 34
3.5. FCC Lattice 40
3.6. FCC Lattice with Inertial Amplification Mechanism 44
4. DESIGN AND ANALYSIS OF 3D DISTRIBUTED PARAMETER MODELS 50
4.1. BCC Lattice 50
4.1.1. Design of the Building Block Mechanisms 50
4.1.2. Distributed Parameter Model of the BCC Lattice 54
4.2. Octahedron Structure 57
4.2.1. Analytical Model of the Building Block Mechanism 58
4.2.2. Computational Model of the Building Block Mechanism 63
4.2.3. Optimization of the Building Block Mechanism 64
4.2.4. Modification of the Building Block Mechanism for 3D Assembly 68
4.2.5. Octahedron Structure 72
4.2.6. 2×3 Array of Octahedron Structures 73
5. DESIGN AND ANALYSIS OF THE INERTIAL AMPLIFICATION MECHANISMS WITH ULTRA WIDE BAND GAP 76
5.1. Optimization of the Inertial Amplification Mechanism with the Constraining Thick Beams 80
5.2. Optimization of the Inertial Amplification Mechanism with the Constraining Slender Beams Considering Manufacturing Constraints 84
6. MANUFACTURING AND EXPERIMENTAL VERIFICATION 89
6.1. Manufacturing of the Octahedron Structures 89
6.2. Experimental Verification of the Octahedron Structures 91
6.3. Manufacturing of the Ultra Wide Band Gap Structure 93
6.4. Experimental Verification of the Ultra Wide Band Gap Structure . . . 96
7. CONCLUSIONS 99
REFERENCES 102

LIST OF FIGURES

Figure 1.1. Periodically varying (a) material and (b) geometry in order to create band gap using Bragg scattering method. 2

Figure 1.2. Locally resonant sonic materials. 3

Figure 1.3. Translational amplification mechanism. 4

Figure 1.4. LADD cell. 4

Figure 1.5. Triangular honeycomb, hexagonal honeycomb and Kagome lattice. 5

Figure 1.6. 2D array of lumped parameter inertial amplification mechanisms. . 6

Figure 1.7. Topology optimized finite structure. 6

Figure 1.8. 2D spring-mass array. 7

Figure 1.9. Chiral composite element which is designed for airfoils. 7

Figure 1.10. Unit cells of cubic lattices. 8

Figure 1.11. Phononic band structures of cubic lattices. 9

Figure 1.12. 2D truss. 10

Figure 1.13. 3D box truss. 11

Figure 2.1. An infinitely periodic array of masses m with uniform distance a. . 13

Figure 2.2. A 1D periodic lattice with uniform masses and springs. 14

Figure 2.3. Band structure of a 1D periodic lattice with uniform masses and springs. Here, $m = 1$, $k = 1$ and $a = 1$. 15

Figure 2.4. A 1D periodic lattice with varying masses and uniform springs. . . 15

Figure 2.5. Band structure of a 1D periodic lattice with varying masses and uniform springs. Here, $m_1 = 1$, $m_2 = 2$, $k = 1$ and $a = 1$. 16

Figure 2.6. Phase and group velocities on a dispersion curve. 17

Figure 2.7. Direct lattice of a 2D periodic structure. 18

Figure 2.8. Reciprocal lattice of the 2D periodic structure and first Brillouin zone. 19

Figure 2.9. Direct and reciprocal lattices of periodic structures. 20

Figure 2.10. Lumped parameter inertial amplification mechanism. 20

Figure 3.1. SC unit cell. 22

Figure 3.2. Phononic band structure of the SC lattice. 24

Figure 3.3. Inertial amplification mechanism. 24

Figure 3.4. Inertial amplification mechanism formed with $2m_a$ and m. 26

Figure 3.5. SC unit cell with embedded inertial amplification mechanisms. . . 26

Figure 3.6. Phononic band structure of the SC lattice with inertial amplification mechanism. 27

Figure 3.7. Lumped parameter BCC unit cell. 29

Figure 3.8. Phononic band structure of the BCC lattice in the case of $m_c = m/4$ and $k_c = k$. 30

Figure 3.9. Phononic band structure plots for decreasing values of m_c and k_c. 31

Figure 3.10. Effect of m_c/m_{total} on the band gap of the infinite periodic BCC lattice. 32

Figure 3.11. 4×2×2 array of BCC unit cells. 33

Figure 3.12. Frequency response plots of 4×2×2, 4×4×4 and 8×8×8 arrays of BCC unit cells. 34

Figure 3.13. BCC unit cell with inertial amplification mechanism. 35

Figure 3.14. Phononic band structure of the BCC lattice with inertial amplification mechanism. Here, band gap starts at 0.218 and there is no upper limit. 36

Figure 3.15. Effect of amplifier mass ratio ($22m_a/m_{total}$) on the band gap of the infinite periodic BCC lattice. $k_a/k = 10$, $\theta = \pi/18$ and $m/m_c = 1$. 36

Figure 3.16. Frequency response plots of 4×2×2, 4×4×4 and 8×8×8 arrays of BCC unit cells with inertial amplification mechanism. 37

Figure 3.17. 4×2×2 array of BCC unit cells with inertial amplification mechanism. 38

Figure 3.18. FRF plot of the 8×8×8 BCC lattice with inertial amplification where $k_a/k = 10$, $\theta = \pi/18$, $m_c/m_{total} = 1/5$, $m/m_{total} = 1/5$ and $22m_a/m_{total} = 3/5$. 39

Figure 3.19. FCC unit cell, where m is the corner mass, m_c denotes the face centered masses, k is the stiffness of the edge springs and k_c is the stiffness of the springs between the face centers and the corners. Edge length of the cube is l. 40

Figure 3.20. Phononic band structure of the FCC lattice. It is seen that there is a band gap between 0.635-1.191 Hz. 42

Figure 3.21. Effect of m_c/m_{total} on the band gap of the infinite periodic FCC lattice. 43

Figure 3.22. Frequency response plots of 4×2×2, 4×4×4 and 8×8×8 arrays of FCC unit cells. 44

Figure 3.23. FCC unit cell with inertial amplification mechanism. 44

Figure 3.24. Phononic band structure of the FCC lattice with inertial amplification mechanism. 46

Figure 3.25. Effect of amplifier mass ratio ($30m_a/m_{total}$) on the band gap of the infinite periodic FCC lattice. $k_a/k = 10$, $\theta = \pi/18$ and $m/3m_c = 1$. 47

Figure 3.26. Frequency response plots of 4×2×2, 4×4×4 and 8×8×8 arrays of FCC unit cells with inertial amplification mechanism. 48

Figure 3.27. FRF plot of the 8×8×8 FCC lattice with inertial amplification where $k_a/k = 10$, $\theta = \pi/18$, $3m_c/m_{total} = 1/5$, $m/m_{total} = 1/5$ and $30m_a/m_{total} = 3/5$. 49

Figure 4.1. Inertial amplification mechanism. Here, l_i and t_i are length and thickness of the ith beam for $i = 1, 2, 3$. 51

Figure 4.2. (a-d) First 4 mode shapes of the inertial amplification mechanism with length $\sqrt{3}l/2$. (e) Frequency response of the mechanism with length $\sqrt{3}l/2$. 52

Figure 4.3. (a-d) First 4 mode shapes of the inertial amplification mechanism with length l. (e) Frequency response of the mechanism with length l. 53

Figure 4.4. BCC lattice with distributed parameter inertial amplification mechanism. 54

Figure 4.5. (a) 21^{st}, (b) 22^{nd} and (c) 26^{th} mode shapes of the BCC structure. 56

Figure 4.6. Frequency response plot of the distributed parameter BCC structure. 57

Figure 4.7. (a) The inertial amplification mechanism, and its (b) first, (c) second and (d) third vibration modes. 58

Figure 4.8. (a) Quarter of the inertial amplification mechanism. (b) First mode of the mechanism. Here, α is the angle of the third beam segment, y is the input and x is the output displacement. 59

Figure 4.9. Finite element model of the inertial amplification mechanism. . . . 63

Figure 4.10. (a) Rigid link mechanism equivalent of half of the inertial amplification mechanism showing O_2 as the instant center of rotation for link 1 and the ground link. (b) Half of the mechanism in the second mode and (c) in the third mode. 64

Figure 4.11. First four mode shapes of the optimized inertial amplification mechanism. 66

Figure 4.12. (a) Frequency response of the finite periodic inertial amplification mechanism with various number of unit cells. (b) Band structure of the infinitely periodic inertial amplification mechanism. Here, a represents the length of the mechanism. 69

Figure 4.13. The octahedron structure formed using the uniform thickness optimized inertial amplification mechanisms. 70

Figure 4.14. First three mode shapes of the optimized mechanism with fixed-free BCs. 71

Figure 4.15. (a) The optimized mechanism that can only be used for 1D or 2D assembly. (b) The optimized mechanism with its two ends modified for 3D assembly. 72

Figure 4.16. (a) The octahedron structure formed using the optimized inertial amplification mechanisms with modified ends. (b) Frequency response of the octahedron structure. 74

Figure 4.17. (a) 2×3 array of octahedron structures. (b) Frequency response of the 2×3 array of octahedron structures. 75

Figure 5.1. First and second mode shapes of the inertial amplification mechanism. 76

Figure 5.2. Rigid link equivalent of the inertial amplification mechanism. Here, $DOF = 3$. 77

Figure 5.3. Rigid link equivalent of the modified inertial amplification mechanism. Here, $DOF = 1$. 77

Figure 5.4. The inertial amplification mechanism with the constraining slender beams. 78

Figure 5.5. First and second mode shapes of the inertial amplification mechanism with the constraining slender beams. 78

Figure 5.6. The inertial amplification mechanism with the constraining thick beams. 79

Figure 5.7. First and second mode shapes of the inertial amplification mechanism with the constraining thick beams. 79

Figure 5.8. Inertial amplification mechanism with constraining thick beams which optimized under m_{tot}, k_{tot} and l_{tot} constraints. Here, t_i and l_i are thickness and length of the ith beam segment, respectively. . 80

Figure 5.9. First and second mode shapes of the inertial amplification mechanism with constraining thick beams which is optimized under m_{tot}, k_{tot} and l_{tot} constraints. 81

Figure 5.10. Inertial amplification mechanism with constraining thick beams which is optimized without m_{tot} and k_{tot} constraints. 82

Figure 5.11. First and second mode shapes of the inertial amplification mechanism with constraining thick beams which is optimized without m_{tot} and k_{tot} constraints. 82

Figure 5.12. Frequency response of the inertial amplification mechanism with constraining thick beams which is optimized without m_{tot} and k_{tot} constraints. 83

Figure 5.13. Dimensions of the inertial amplification mechanism with constraining slender beams. Here, y is the input and x is the output displacement. Also, t_i and l_i represent the thickness and length of the ith beam segment. 84

Figure 5.14. First and second vibration modes of the optimized inertial amplification mechanism using 2D model. 85

Figure 5.15. (a) Band structure of the infinitely periodic array. (b) Frequency responses of finite periodic arrays with various number of unit cells. (c) Finite periodic array with 4 unit cells. 86

Figure 5.16. First, second and third vibration modes of the optimized inertial amplification mechanism using 3D shell model. 88

Figure 6.1. Manufacturing of the octahedron structure with 3D printer. 89

Figure 6.2. (a) Equilateral triangles and (b) the octahedron structure. 90

Figure 6.3. The 2×3 array of the octahedron structures. 90

Figure 6.4. Experimental setup of the octahedron structure. 91

Figure 6.5. Experimental and numerical frequency responses of the octahedron structure in longitudinal direction. 92

Figure 6.6. Experimental setup of the 2×3 array of octahedron structures. . . 92

Figure 6.7. Experimental and numerical frequency responses of the 2×3 octahedron array in longitudinal direction. Here, the numerical FRF result is obtained (a) for the undamped case and (b) for $\eta = 0.03$. 94

Figure 6.8. Frequency responses of the 2×3 octahedron array in longitudinal (x) and two transverse (y and z) directions. (a) FEM results for $\eta = 0.03$, (b) experimental results. 95

Figure 6.9. The prototype of the inertial amplification mechanism with ultra wide band gap. 96

Figure 6.10. Excitation and measurement points for the ultra wide band gap structure. 96

Figure 6.11. Experimental setup for the ultra wide band gap structure. 97

Figure 6.12. Experimental and numerical frequency response results of the ultra wide band gap structure. 98

LIST OF TABLES

Table 4.1. Mesh convergence study for the finite element model. 55

Table 4.2. Comparison of analytical and numerical resonance and antiresonance frequency results. 67

Table 4.3. Natural frequencies of the octahedron structure. 70

Table 4.4. Natural frequencies of the modified mechanism with pinned-roller boundary conditions. 72

Table 4.5. Natural frequencies of the modified mechanism with fixed-free boundary conditions. 72

Table 5.1. Band gap limits of inertial amplification mechanisms. 80

Table 5.2. Comparison of band gap limits of the optimized inertial amplification mechanisms. 83

Table 5.3. Frequency limits of the first band gap of the inertial amplification mechanism with constraining beams. 87

Table 6.1. Numerical and experimental band gap limits of the ultra wide band gap mechanism. 98

LIST OF SYMBOLS

a, a_j	Distances between two particles
b	Out-of-plane thickness
c_l	Longitudinal wave propagation speed
c_t	Transverse wave propagation speed
E	Young's modulus
k, k_a, k_c	Stiffness coefficients
k_{tot}	Total stiffness of the mechanism
l_i	Length of the ith beam segment
l_{tot}	Total length of the mechanism
m, m_a, m_c	Lumped masses
m_{tot}	Total mass of the mechanism
t_i	Thickness of the ith beam segment
u, u_j	Displacement vectors
γ	Wave vector
η	Structural damping coeffiecient
ρ	Density
ω	Angular frequency
ω_g	Midgap frequency
ω_l	Lower band gap limit
ω_u	Upper band gap limit
ω_s	Starting frequency of the band gap

LIST OF ACRONYMS/ABBREVIATIONS

1D	One Dimensional
2D	Two Dimensional
3D	Three Dimensional
BC	Boundary Condition
BCC	Body Centered Cubic
DOF	Degree of Freedom
FCC	Face Centered Cubic
FE	Finite Element
FEA	Finite Element Analysis
FEM	Finite Element Method
FRF	Frequency Response Function
HCP	Hexagonal Close Packed
LADD	Linear-to-Angular Displacement Device
SC	Simple Cubic

1. INTRODUCTION

Phononic crystals are periodic structures which prevent propagation of elastic or acoustic waves in certain frequency ranges known as phononic band gaps or stop bands. Researchers are interested in periodic structures that possess phononic band gaps for more than two decades. Stop bands can be generated in both infinite and finite periodic structures. There is no wave propagation within the stop band of an infinite periodic structure [1]. However, finite periodic structures cannot completely hinder wave propagation or vibration transmission even if they are excited within stop bands. The amount of vibration transmission in finite periodic structures can be characterized by analyzing the depth profile of the gap (stop band) in a frequency response function (FRF) plot [2,3]. Finite periodic band gap structures can be used as noise or vibration isolators, mechanical filters, acoustic lenses and elastic waveguides [4–7]. Hence, designing phononic band gap structures with wide stop bands and obtaining good isolation characteristics inside the stop bands can be beneficial for various applications.

Phononic band gaps are generally investigated in one-dimensional (1D) and two-dimensional (2D) periodic structures [8–22]. Studies that focus on analyzing or designing phononic band gaps in three-dimensional (3D) structures are quite limited in number. In most of these studies, face centered cubic (FCC) arrangement of scatterers in a host material have been considered [23–33]. However, simple cubic (SC), body center cubic (BCC) and hexagonal closed packed (HCP) arrangements have also been investigated [30–36]. There are also a few studies about 3D geometries which are specifically designed in order to obtain phononic band gap structures rather than cubic lattices [37, 38].

1.1. Band Gap Generation Methods

Band gaps (stop bands) in periodic structures are commonly generated by Bragg scattering or local resonances methods. Moreover, inertial amplification is another method to create band gaps in periodic structures. In this section, these band gap

generation methods will be explained.

1.1.1. Bragg Scattering

In the Bragg scattering method, band gap is created using periodically varying mass or stiffness. Generally, scatterers of high density materials are embedded in a low density host material to create band gaps [14, 20, 22, 24–34]. Oftentimes, face-centered cubic (FCC) arrangement of the scatterers are utilized to form band gaps [24–30]. Other arrangements such as simple cubic (SC), body-centered cubic (BCC) and hexagonal-close-packed (HCP) are also investigated [31–34]. In some studies, band structures of the lattices are tuned by utilizing piezoelectricity [20, 29, 31] or magnetic fields [14].

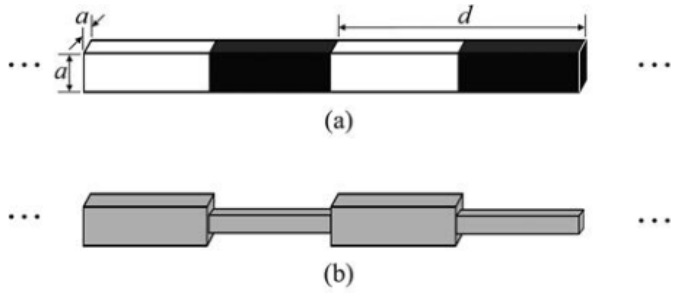


Figure 1.1. Periodically varying (a) material and (b) geometry in order to create band gap using Bragg scattering method [22].

In this method, ratio of wave speed and lattice constant determine the lowest band gap frequency [39, 40]. Thus, it is required to use high density/low modulus materials or large-sized structures in order to obtain band gaps at low frequencies.

1.1.2. Local Resonance

In the local resonance method, periodic local resonators are added to a host structure in order to create band gaps. In order to create band gaps at much lower frequencies than that can be obtained by Bragg scattering, high density materials (gold,lead, etc.) are coated with soft elastic layers (rubber) and embedded in a matrix material (epoxy) [21–23, 36, 39–45]. 1D and 2D periodic band gap structures are investigated

in [21, 22, 40, 42–45] and 3D periodic band gap structures are studied in [23, 36, 39, 41].

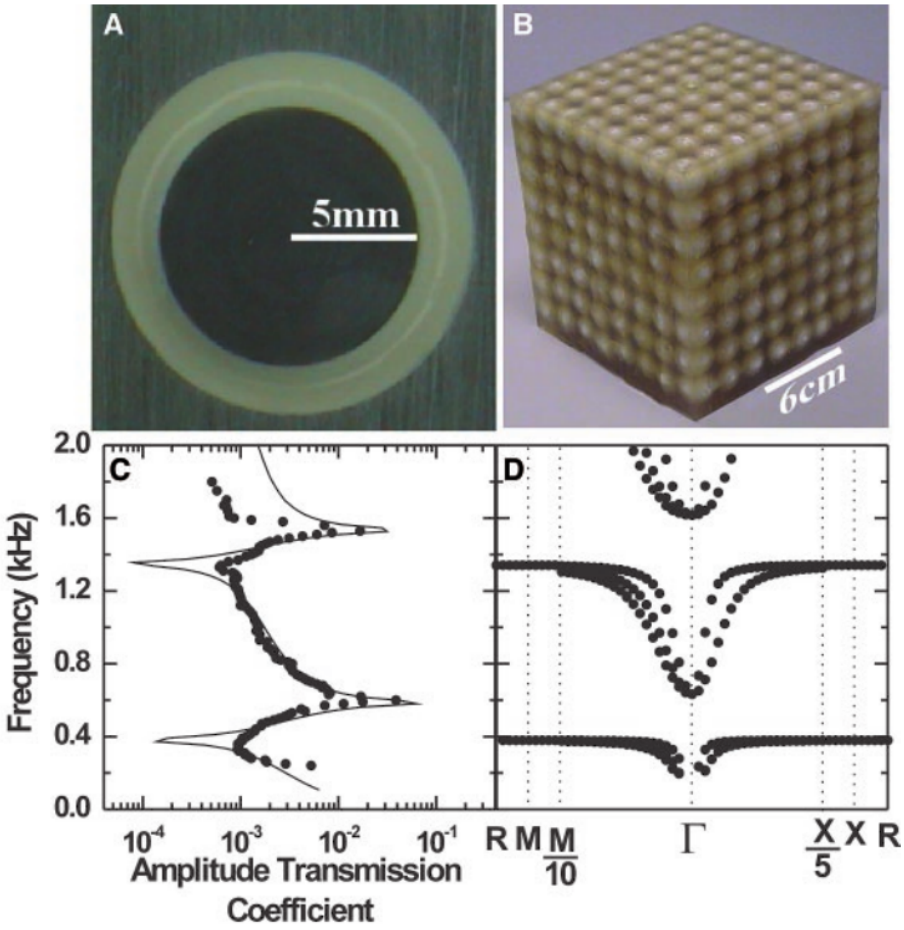


Figure 1.2. Locally resonant sonic materials [36].

However, as in Bragg scattering method, it is also hard to obtain wide low frequency band gaps using local resonance method since heavy resonators that constitute most of the total mass of the structure are needed [39, 40].

1.1.3. Inertial Amplification

A novel band gap generation method is inertial amplification. In this method phononic band gap generation is based on amplifying the effective inertia of the wave propagation medium with the use of embedded amplification mechanisms. As a result, wide phononic band gaps can be formed at low frequencies without using excessive mass on the amplification mechanisms. Advantage of the inertial amplification method is to

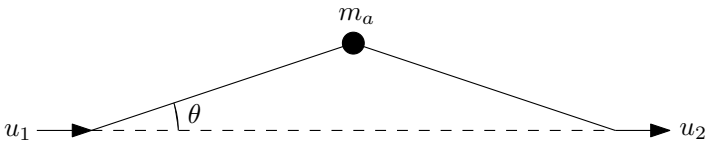


Figure 1.3. Translational amplification mechanism.

obtain wide low-frequency band gaps without increasing the total mass or decreasing the total stiffness of the lattice. In [12,13], the existence of inertial amplification induced wide and deep phononic band gaps have been shown using 2D lumped parameter periodic lattices. Distributed parameter inertial amplification mechanisms are also investigated in [46].

However, inertial amplification induced phononic band gaps in 3D lattices haven't been investigated up to this study and the first two studies were published recently within the framework of this thesis [47, 48].

The simplest translational amplification mechanism can be seen in Figure 1.3. In this amplification mechanism, displacement of the mass m_a is $(\cot\theta)/2$ times larger than the displacement of both ends relative to each other $(u_1 - u_2)$. For small θ, it is possible to obtain large inertial force amplification.

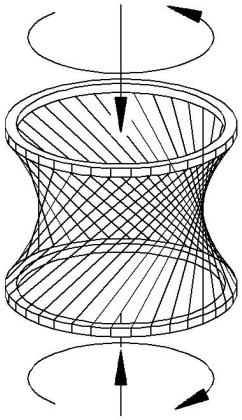


Figure 1.4. LADD cell [49].

Translational to rotary amplification is also possible using springs, twisted ropes, gears, screws or linear-to-angular displacement device (LADD) cells (see Figure 1.4).

The main purpose of using such a mechanism is create large translation or rotation using small displacements of these amplification elements. Thus, the large inertia forces could be obtained by connecting little masses to the points with large displacements [49–51].

1.2. Types of Periodic Lattices

1.2.1. 2D Periodic Lattices

2D periodic lattices are usually generated by extrusion of a planar geometry such as honeycomb and their properties only change in-plane. Most of the studies in the literature investigate wave propagation in two in-plane directions and they do not consider out-of-plane direction. In [11], band structures of different 2D periodic lattices such as triangular honeycomb, hexagonal honeycomb and Kagome lattice (see Figure 1.5) are investigated using Floquet-Bloch theory.

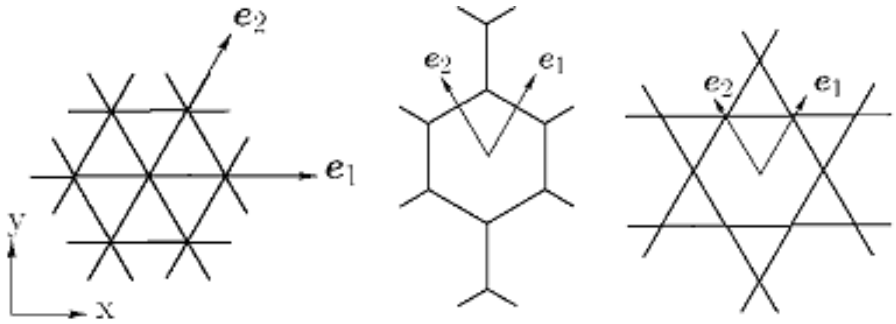


Figure 1.5. Triangular honeycomb, hexagonal honeycomb and Kagome lattice [11].

In [12], a periodic media is introduced which has a rhombus unit cell produced with inertial amplification mechanisms. In [13], a periodic media is formed with square unit cells which is composed of two inertial amplification mechanisms with different lengths. In both of the studies, it is seen that wave propagation is prevented in a wide range of frequency comparing to ones obtained with local resonance or Bragg scattering methods.

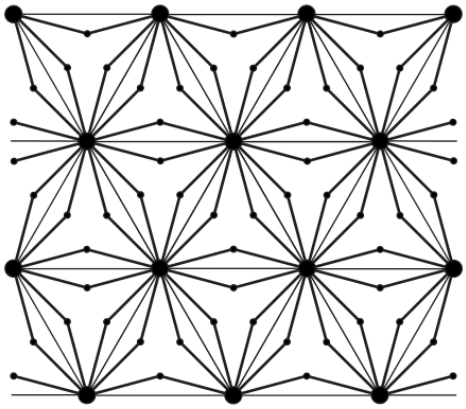


Figure 1.6. 2D array of lumped parameter inertial amplification mechanisms [12].

Piezoelectric or magneto-elastic materials are also interested for frequency filter design since it is possible to change band structure during operation. Two-dimensional periodic lattice composed of magneto-elastic square rod is investigated in [14]. Normal dispersion curve of this lattice is compared with the one in magnetic field and it is seen that band gap can be tuned by changing the applied magnetic field. In [20], the two dimensional phononic crystals are investigated in which band gaps are created with different piezoelectric and piezomagnetic inclusion in quartz and polymer matrices.

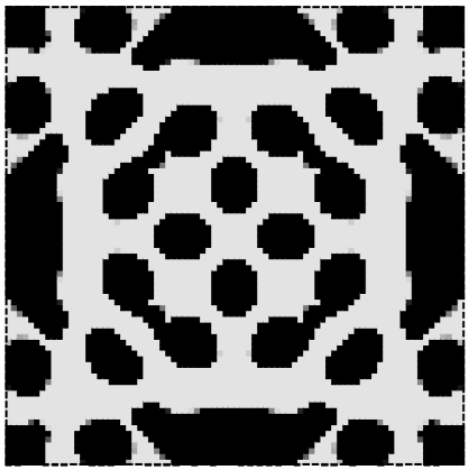


Figure 1.7. Topology optimized finite structure investigated in [10].

Shape and topology optimization of the inclusions are also common in two-dimensional lattices. In [10], topology optimization is used in order to maximize band gap of the two-dimensional infinite and finite periodic structures for a desired frequency. Square rod inclusions in air is investigated in [9] with the aim of controlling the acoustic

frequency gaps. Band structures are obtained for different angular arrangements and filling fractions and it is shown that gap width can be adjusted by rotating the square rods.

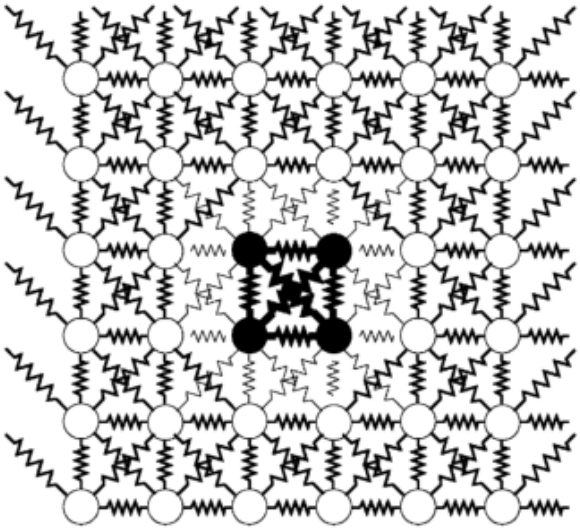


Figure 1.8. 2D spring-mass array [21].

In [21], wave propagation of one and two-dimensional finite periodic lattices composed of spring and mass elements are investigated. Band structures are given for different lattices with various spring coefficients and point mass values. It is shown how band gap structure depends on the number of unit cells, boundaries, damping and imperfections in the structure.

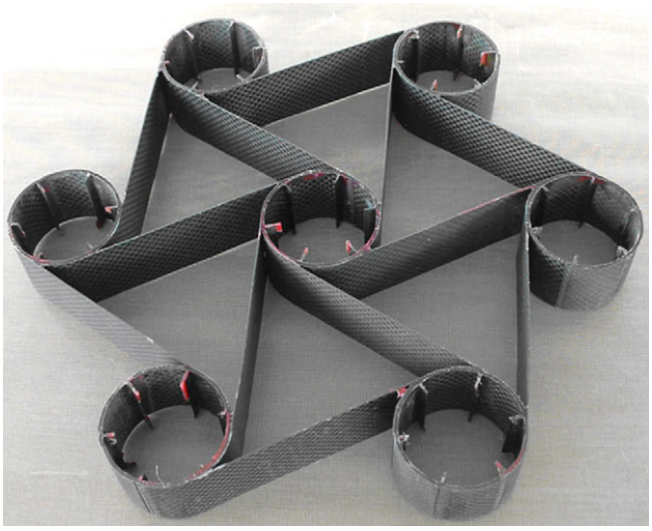
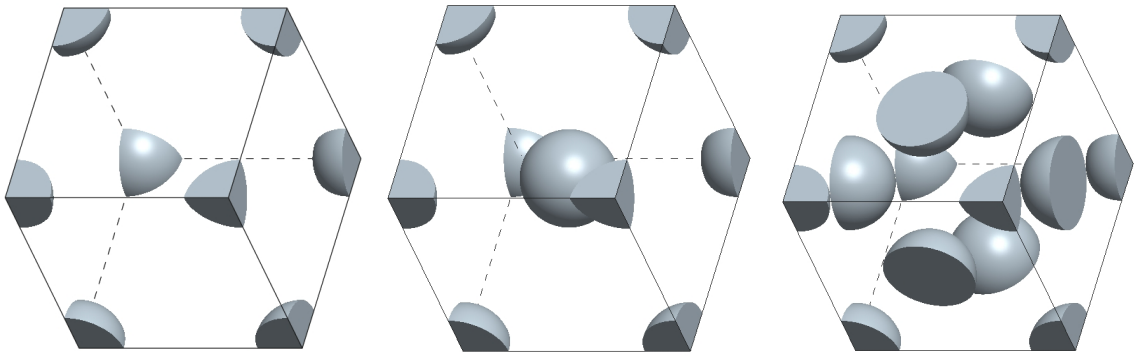


Figure 1.9. Chiral composite element which is designed for airfoils [52].

Chiral cell honeycombs are also commonly investigated in the literature. There are several lattices composed of different chiral unit cell such as hexa-chiral or tetra-chiral. In the literature, it is shown that band gap structures can be changed by changing angular orientation and relative radius of chiral cells [15, 16, 44, 45, 52, 53].

1.2.2. Cubic Lattices

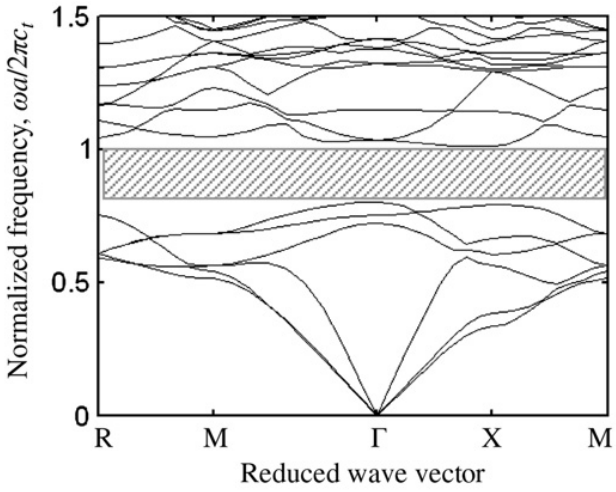
FCC, BCC and SC are commonly investigated cubic structures in the literature. Studies on three-dimensional lumped parameter structures are quite limited. High density (gold, lead, etc.) spheres embedded in epoxy using the SC, BCC and FCC structures investigated in [31,33] can be given as examples of distributed parameter 3D cubic lattices. In some of the studies, piezoelectric particles or magneto-elastic particles are also used in order to tune bang gap depending on the requirements [29, 31].



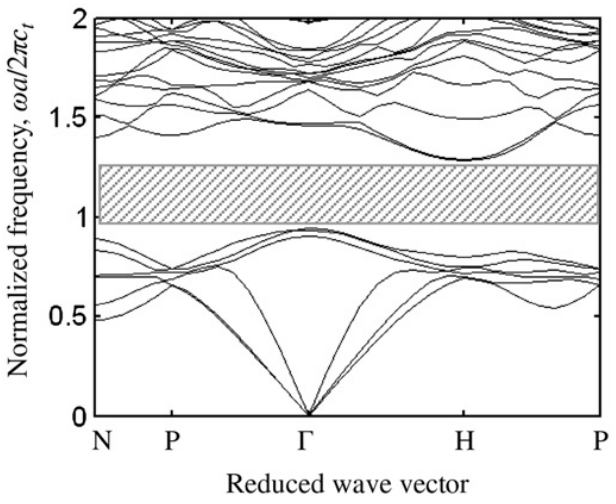
(a) SC (b) BCC (c) FCC

Figure 1.10. Unit cells of cubic lattices [54].

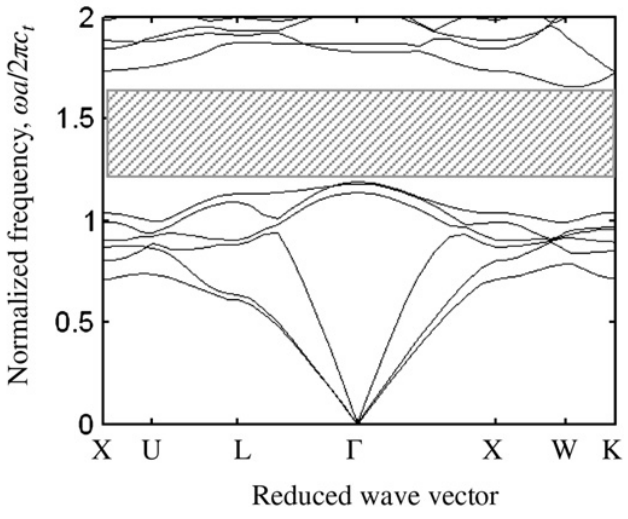
Figure 1.11 shows phononic band structures of the cubic lattices which are investigated in [31]. Lead zirconate titanate (PZT-2) and zinc oxide (ZnO) particles in polymer matrices are investigated. It is shown that band gaps obtained by BCC and FCC arrangement are larger than those of SC arrangement. It also shown that piezoelectricity on the band gaps of the PZT-2/polymer lattices are more obvious than those for the ZnO/polymer lattices.



(a) SC



(b) BCC



(c) FCC

Figure 1.11. Phononic band structures of cubic lattices [31].

In [30], wave propagation is investigated in a FCC structure formed with gold spheres embedded in a silicon matrix. Large band gaps are obtained for specific directions only. No band gap obtained for all directions. Also wave propagation along the [001] direction of a HCP structure consisting of stainless steel balls immersed in water is investigated and reasonable band gap is obtained for this specific direction only.

Although opals are generally used for photonic stop bands, the vibrational properties of opal films assembled from closely packed silica spheres are investigated in [55]. Wave propagation in finite number of opal films are investigated in [111] direction only. The study claims that the existence of large band gaps is insensitive to the presence of defects and therefore opals can be used for future applications of nano acoustic devices.

1.2.3. Truss Structures

Vibration of truss structures are commonly investigated in the literature since they are extensively used for bridges, roofs, electricity pylons, etc. Generally extruded two-dimensional truss structures are investigated. Investigation of three-dimensional trusses in different directions are rare.

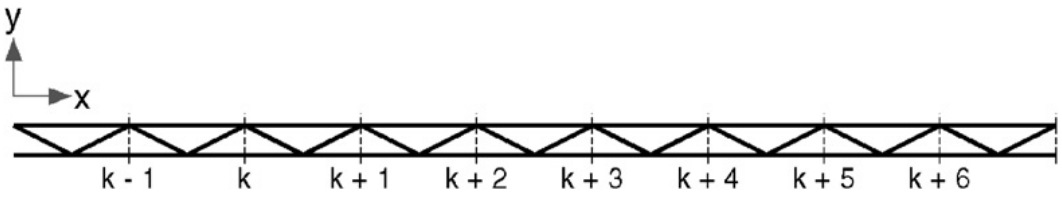


Figure 1.12. 2D truss [56].

In [56], wave propagation in truss structures are studied. Frequency response in periodic and non-periodic structures are investigated. Also in [57], the structural mechanics of the periodic pin-jointed truss is investigated by application of Bloch theorem. Pin-jointed mechanisms and load carrying structures are classified in this study.

In [58], three-dimensional truss-like structures are extruded from two-dimensional frames. Curved structures are formed using identical unit cells. The frequency response

of these structures and effects of panel curvature are investigated. It is concluded that the frequency response is more dependent to unit cell geometry than the panel curvature.

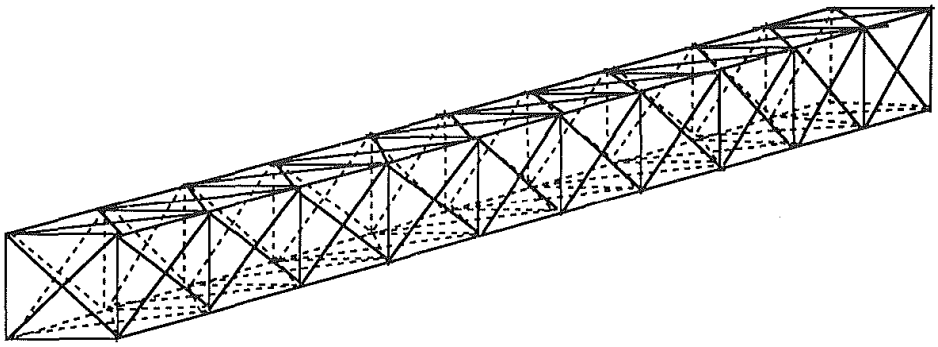


Figure 1.13. 3D box truss [59].

In [60], a three-dimensional active truss structure is built using two active piezoelectric components and experimental frequency response plots are obtained for both active and passive cases. It is concluded that vibration suppression capability of the active truss is better compared to that of the passive one. Also in [59], several two and three-dimensional truss structures are investigated. An analytical method is proposed in order reduce computational cost. The natural frequencies are obtained using analytic and numerical methods, and they are compared.

1.3. Contributions of This Ph.D. Thesis

In real life, 3D structures are excited in any direction and there are few studies about 3D band gap structures in the literature. Inertial amplification is a new method to generate phononic band gaps in periodic structures and 3D structures with inertial amplification mechanisms are designed for the first time in this study. If there are mass and stiffness constraints, it is hard to isolate low frequency vibrations using other methods. However, 3D structures built with inertial amplification mechanisms can isolate low frequency vibrations in all directions without increasing total mass or total stiffness. There was no work on 3D periodic structures with inertial amplification and the first two studies were published recently within the framework of this thesis. An article about octahedron structures is submitted in revised form to International

Journal of Solids and Structures. An article is being written about ultra wide band gap mechanisms and it is planned to be submitted in a month.

1.4. Applications

3D periodic structures built with inertial amplification mechanisms can be used as vibration isolation systems in various applications. One possible application can be in engine mount systems. Since the vibrations created by engines are in a known frequency range, it is possible to design a mechanism that can show vibration isolation in that frequency range. Moreover, the most important possible application is the use of such mechanisms in earthquake resistant structures as inertial amplification mechanisms can isolate low frequency vibrations. Furthermore, it may be possible to create active vibration isolation structures by controlling the length of the flexure hinges used in the mechanism. These active vibration isolation structures can have the ability to modify the band gap frequency range depending on the excitation.

1.5. Organization of Thesis

The aim of this study is to design three-dimensional structures which are capable of isolating vibration in all directions and in a very wide frequency range. Both lumped and distributed parameter three-dimensional phononic band gap structures are investigated. In Chapter 2, analytical methods required to obtain phononic band structure of a periodic lattice are given. In Chapter 3, lumped parameter SC, BCC and FCC lattices are investigated. In Chapter 4, distributed parameter models of a BCC lattice, an octahedron structure and a 2×3 array of octahedron structures are analyzed. The building block mechanism is optimized in order to obtain wide low frequency band gaps in the 3D structures formed with them. In Chapter 5, an ultra wide band gap structure is introduced. This ultra wide band gap structure is also optimized in order to obtain widest possible band gap. In Chapter 6, manufacturing and experimental verification of these distributed parameter structures are explained. Numerical results obtained in Chapters 4 and 5 are verified. In Chapter 7, conclusions and summary of the main contributions are given and recommendations for further work are also included.

2. THEORY

In this chapter, analytical methods required to obtain phononic band structure of a periodic lattice are given. Bloch theorem is expressed. Simple and well-known examples, periodically repeating spring mass systems are investigated in order to understand application of the Bloch theorem to the periodic lattices. Dispersion relation, direct and reciprocal lattices are explained. Then, effective inertia of an inertial amplification mechanism is calculated in order to emphasize contribution of this method. Finally, arithmetic and geometric mean normalized band gaps are defined.

2.1. Bloch Theorem

Bloch theorem is used to obtain band structure of the infinitely periodic lattices [61]. It states that the displacement of a periodically repeating particles m in all neighboring unit cells ($u^{(n+j)}$) can be expressed in terms of the displacement of the particle in one unit cell ($u^{(n)}$) as follows:

$$u^{(n+j)} = e^{i\gamma a j} u^{(n)} \tag{2.1}$$

where $u^{(n)}$ is the displacement of the n^{th} mass, $u^{(n+j)}$ is the displacement of the $(n+j)^{th}$ mass, a is the distance between each particle, $i = \sqrt{-1}$ and γ is the wave number.

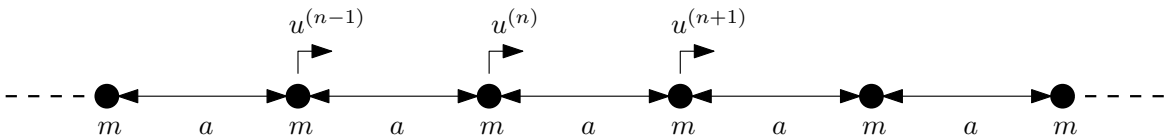


Figure 2.1. An infinitely periodic array of masses m with uniform distance a.

Using Bloch theorem, displacement of the mass (n+1) can be written in terms of $u^{(n)}$ such that

$$u^{(n+1)} = e^{i\gamma a} u^{(n)}. \tag{2.2}$$

2.2. 1D Periodic Lattice with Uniform Masses and Springs

In order to understand how the band structure of a 1D periodic lattice is obtained using Bloch theorem, it would be beneficial to show an one-dimensional periodic structure as seen in Figure 2.2. In this periodic structure there is one periodic mass m and one periodic spring k.

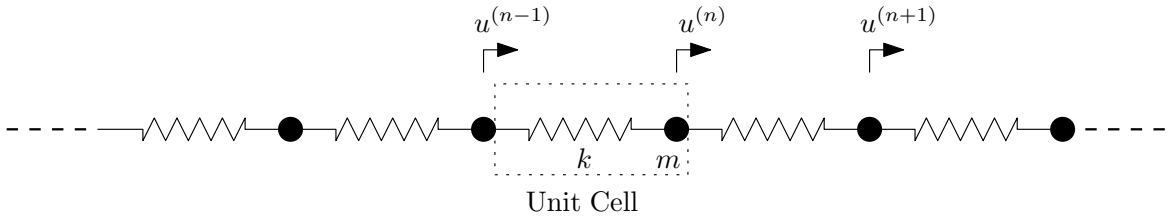


Figure 2.2. A 1D periodic lattice with uniform masses and springs.

For this case, equations of motion for the n^{th} mass can be written as:

$$-\omega^2 m u^{(n)} = -k\left(u^{(n)} - u^{(n-1)}\right) - k\left(u^{(n)} - u^{(n+1)}\right). \tag{2.3}$$

Using Bloch theorem, it is possible to write $u^{(n+1)}$ and $u^{(n-1)}$ in terms of $u^{(n)}$. After these substitutions, equation of motion of the periodic structure with uniform masses and springs can be rewritten as:

$$\omega^2 m u = k\left(2 - e^{i\gamma a} - e^{-i\gamma a}\right) u \tag{2.4}$$

If this equation is solved for ω using γ values from $-4\pi/a$ to $4\pi/a$, band structure of the 1D periodic lattice is obtained as seen in Figure 2.3.

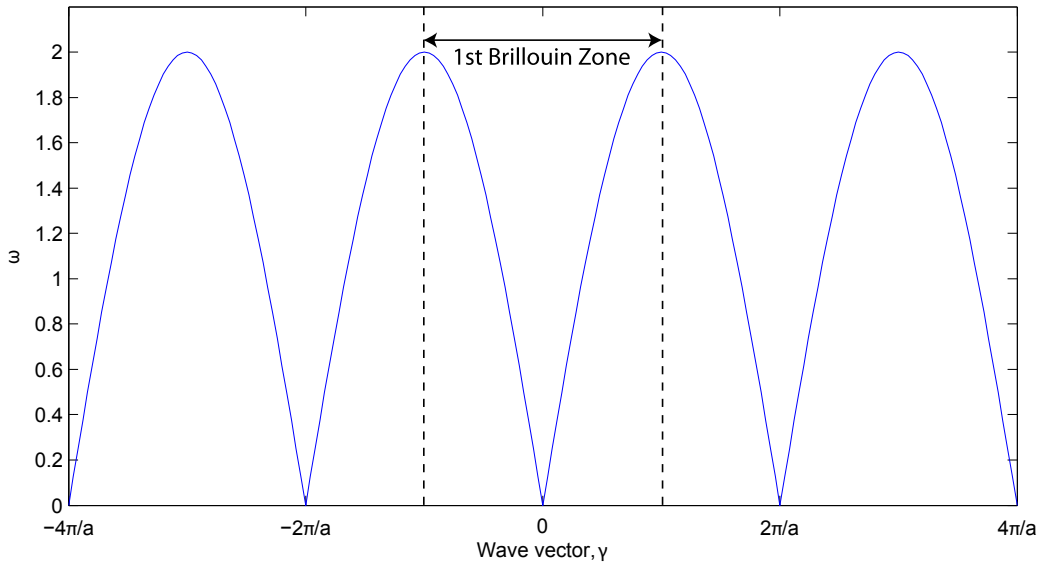


Figure 2.3. Band structure of a 1D periodic lattice with uniform masses and springs. Here, $m = 1$, $k = 1$ and $a = 1$.

2.3. 1D Periodic Lattice with Varying Masses and Uniform Springs

Instead of periodically repeating masses, it is possible to use two different masses to create a 1D periodic lattice as seen in Figure 2.4.

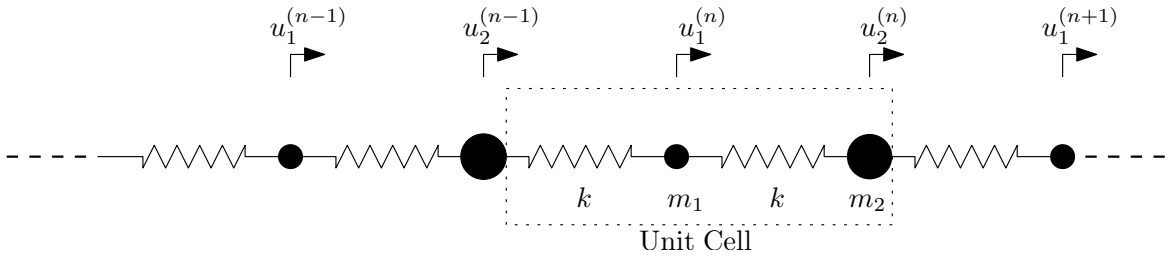


Figure 2.4. A 1D periodic lattice with varying masses and uniform springs.

For this case, equations of motion for the two different masses can be written as

$$-\omega^2 m_1 u_1^{(n)} = -k\left(u_1^{(n)} - u_2^{(n+1)}\right) - k\left(u_1^{(n)} - u_2^{(n)}\right) \tag{2.5}$$

$$-\omega^2 m_2 u_2^{(n)} = -k\left(u_2^{(n)} - u_1^{(n)}\right) - k\left(u_2^{(n)} - u_1^{(n-1)}\right) \tag{2.6}$$

In vector form, this two relation can be written as:

$$-\omega^2 \begin{bmatrix} m_1 & 0 \\ 0 & m_2 \end{bmatrix} \begin{bmatrix} u_1 \\ u_2 \end{bmatrix} = \begin{bmatrix} -2k & k\left(1+e^{i\gamma a}\right) \\ k\left(1+e^{-i\gamma a}\right) & -2k \end{bmatrix} \begin{bmatrix} u_1 \\ u_2 \end{bmatrix} \tag{2.7}$$

If this eigenvalue problem is solved for γ from $-4\pi/a$ to $4\pi/a$, band structure of the 1D periodic lattice with varying masses and uniform springs can be obtained as seen in Figure 2.5. Notice that, for this lattice, a band gap is formed between 1 and 1.41.

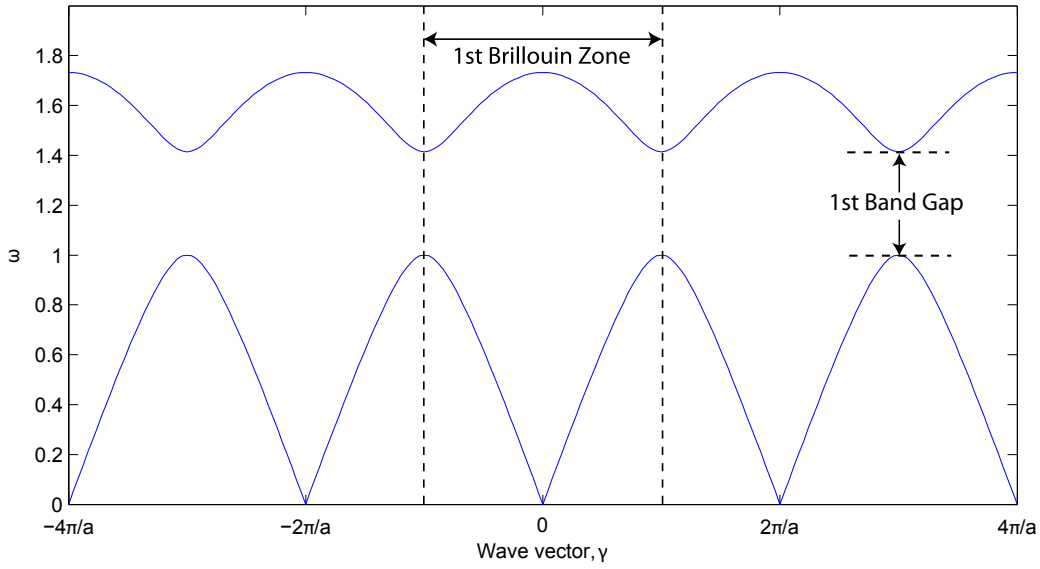


Figure 2.5. Band structure of a 1D periodic lattice with varying masses and uniform springs. Here, $m_1 = 1$, $m_2 = 2$, $k = 1$ and $a = 1$.

A band gap can also be generated by varying the stiffness elements rather than the mass elements in the lattice.

2.4. Dispersion Relation

In Figure 2.6, more detailed dispersion relation of the 1D periodic structure created using two different masses is given. In this figure, first band gap, first Brillouin zone, phase and group velocities are marked. Here, γ is the wave vector and $\omega(\gamma)$ is

the frequency as a function of wave number. For 1D case, the wave vector is named as "wave number". Slope of the lines shown in Figure 2.6 gives phase and group velocities. Phase velocity is phase difference between two vibrating point [62] and calculated as follows:

$$\text{Phase Velocity} = \frac{\omega}{\gamma} \tag{2.8}$$

Group velocity is transmission velocity of wave packets (or envelope of waves) [61] and calculated as follows:

$$\text{Group Velocity} = \frac{d\omega}{d\gamma} \tag{2.9}$$

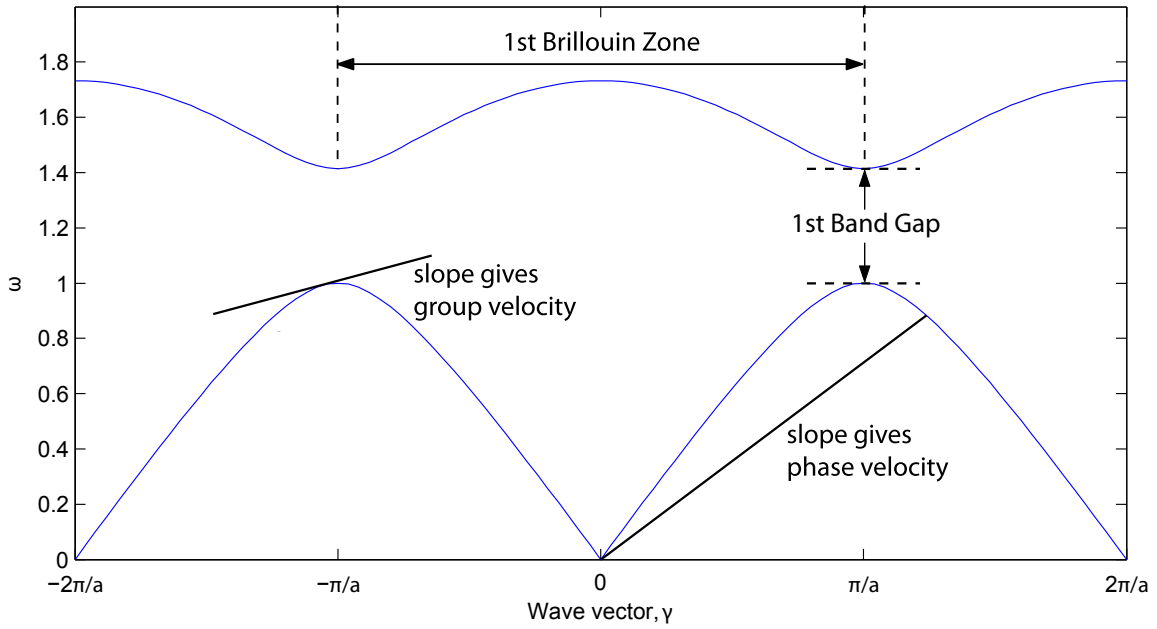


Figure 2.6. Phase and group velocities on a dispersion curve.

2.5. Reciprocal Lattice

Consider the 2D periodic lattice investigated in [63] as seen in Figure 2.7. Here, $\boldsymbol{d_1}$ and $\boldsymbol{d_2}$ are basis vectors of the "direct lattice". For each 2D periodic direct lattice

it is possible to define a "reciprocal lattice" with the basis vectors $\boldsymbol{b_1}$ and $\boldsymbol{b_2}$ such that

$$\boldsymbol{d_i} \cdot \boldsymbol{b_j} = \delta_{ij} \tag{2.10}$$

where δ_{ij} is Kronecker delta, $i = 1, 2$ and $j = 1, 2$. Notice that, in Figure 2.7, $\boldsymbol{b_1}$ is perpendicular to $\boldsymbol{d_1}$ and $\boldsymbol{b_2}$ is perpendicular to $\boldsymbol{d_2}$.

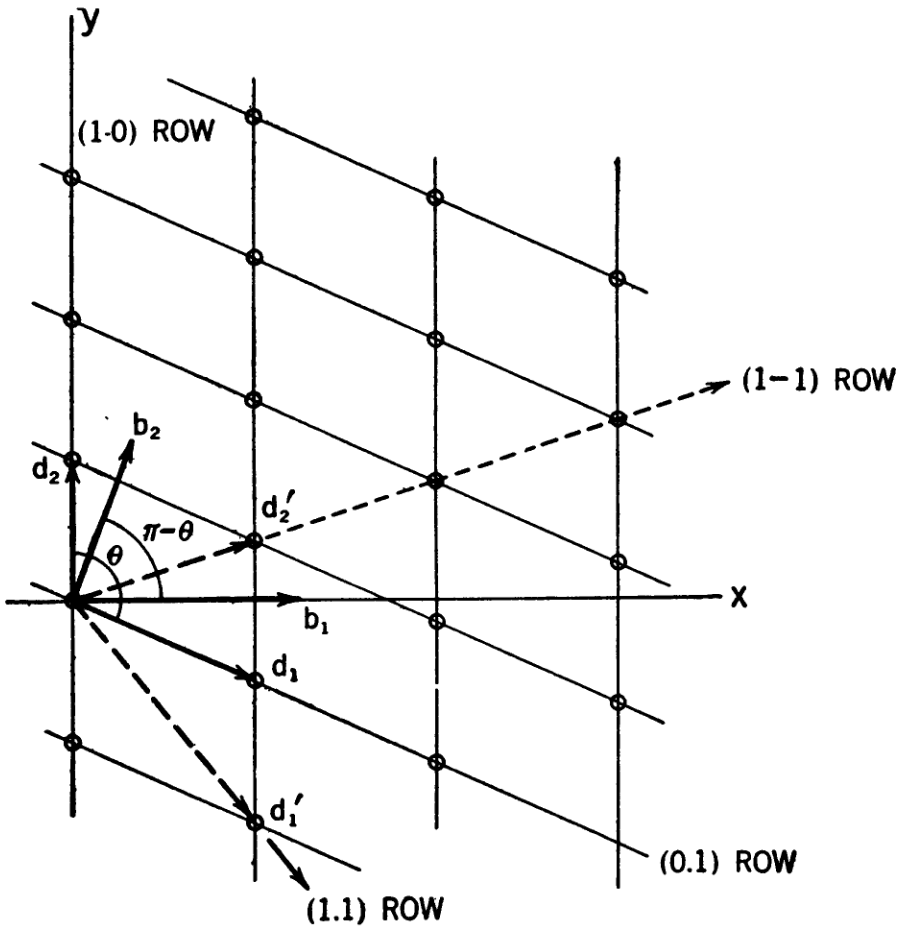


Figure 2.7. Direct lattice of a 2D periodic structure investigated in [63].

Reciprocal lattice formed with the basis vectors $\boldsymbol{b_1}$ and $\boldsymbol{b_2}$ can be seen in Figure 2.8. In a reciprocal lattice, regions or volumes bounded by lines in 2D lattices or surfaces in 3D lattices which have equivalent distance to an element and neighboring elements is called the "Brillouin zone". First Brillouin zone of the 2D periodic structure can be seen in Figure 2.8. In [61], it is stated that all independent values of the exponential $e^{i\boldsymbol{\gamma}\cdot\mathbf{a_j}}$ can be calculated using γ values on the exterior boundary of the Brillouin zone.

Thus, wave propagation in all directions for a periodic structure can be obtained by solving the equation of motion using the γ values on the exterior boundary of the Brillouin zone.

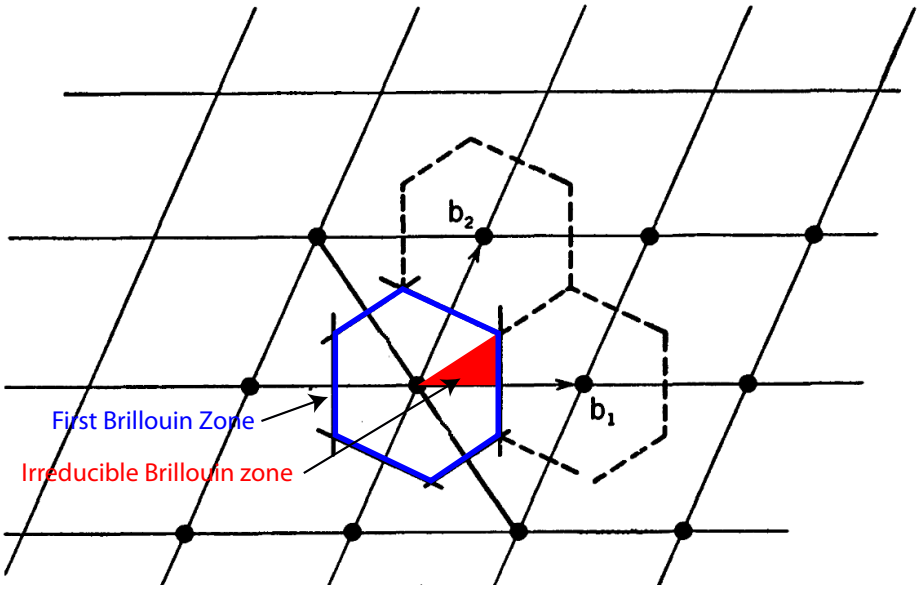
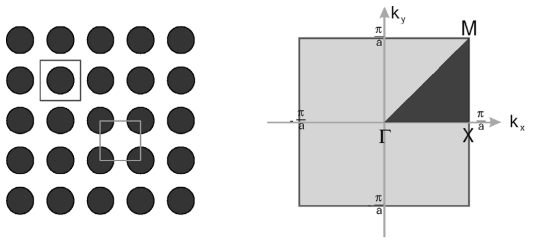


Figure 2.8. Reciprocal lattice of the 2D periodic structure investigated in [63].

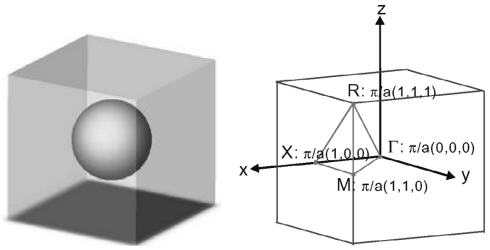
In Figure 2.9, direct and reciprocal lattices of 2D an 3D periodic structures are also given. Reciprocal lattices of 3D periodic structures will be used while investigating the band structures of the cubic lattices in Chapter 3.

2.6. Inertial Amplification Mechanism

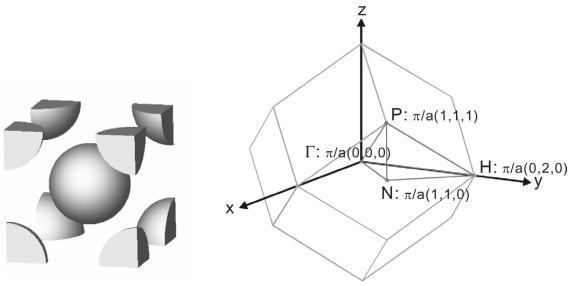
In order to understand effects of inertial amplification, it would be helpful to give an example using a simple inertial amplification mechanism as seen in Figure 2.10. In this mechanism, $\tilde{u} = \dfrac{u_1 + u_2}{2}$, $\tilde{v} = \dfrac{v_1 + v_2}{2}$ and $\tilde{w} = \dfrac{w_1 + w_2}{2}$ cause translation of unit cell with total mass $(2m + m_a)$ and, $\dfrac{|v_1 - v_2|}{2}$ and $\dfrac{|w_1 - w_2|}{2}$ cause rotation of unit cell. $\delta = \dfrac{|u_1 - u_2|}{2}$ causes compression of rod with stiffness k. During this compression, mass m_a translates $\delta \cot\theta$ in y direction. For small θ, equivalent inertia of the mass m_a may be greater than the total mass of the system $(2m + m_a)$ due to the amplification in the mechanism.



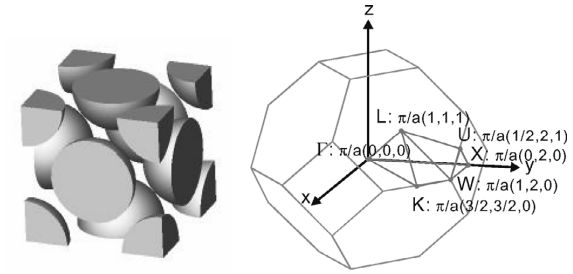
(a) 2D



(b) SC



(c) BCC



(d) FCC

Figure 2.9. Direct and reciprocal lattices of periodic structures [33].

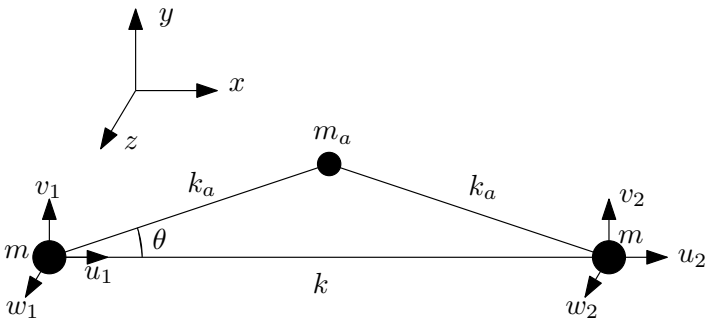


Figure 2.10. Lumped parameter inertial amplification mechanism.

2.7. Normalized Bandwidth

In this study, normalized bandwidth will be used in order to characterize band structure of different lattices. In the literature, normalized bandwidth (BW_a) of a phononic gap is generally calculated using the arithmetic mean ($\omega_g = (\omega_u + \omega_l)/2$) of the upper ($\omega_u$) and lower ($\omega_l$) limits of the gap [17, 64, 65].

$$BW_a = \frac{\Delta\omega}{\omega_g} = \frac{\omega_u - \omega_l}{(\omega_u + \omega_l)/2} \tag{2.11}$$

If the bandwidth is narrow (e.g. less than 10%), arithmetic and geometric means of the upper and lower limits of the gap give approximately the same mid-gap frequency. However, BW_a cannot be used to characterize or differentiate wide band gaps. As $\omega_u/\omega_l \to \infty$, $BW_a \to 2$. For large bandwidths, the mid-gap frequency is defined using the geometric mean [66]. One can see that as $\omega_u/\omega_l \to \infty$, $BW_g \to \infty$. Therefore, BW_g can better characterize wide band gaps. Geometric mean normalized bandwidth (BW_g) is defined as

$$BW_g = \frac{\omega_u - \omega_l}{\sqrt{\omega_u \omega_l}}. \tag{2.12}$$

3. DESIGN AND ANALYSIS OF 3D LUMPED PARAMETER MODELS

In these chapter, lumped parameter SC, BCC and FCC lattices are investigated. Lumped parameter models are appropriate to examine 3D periodic band gap structures with less computational cost comparing to distributed parameter models. Each of these lumped parameter cubic lattices are first investigated without inertial amplification mechanisms. Then, inertial amplification mechanisms are added to the each lattice in order to see effects of inertial amplification on their band gap structures.

3.1. SC Lattice

First, SC lattice is investigated. The unit cell of the SC lattice is shown in Figure 3.1. Due to periodic boundary conditions, only the mass shown in Figure 3.1 belongs to this unit cell.

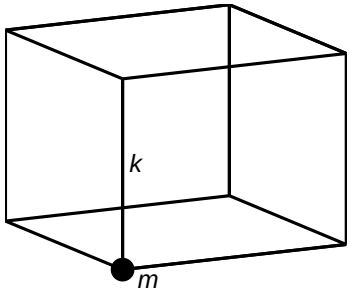


Figure 3.1. SC unit cell.

Displacement of all six points in this unit cell can be expressed using Bloch's theorem such that

$$\mathbf{u}^{(n+\mathbf{a_j})} = \mathbf{u}^{(n)} e^{i\boldsymbol{\gamma}\cdot\mathbf{a_j}} \tag{3.1}$$

where $u^{(n)}$ is the displacement of the mass m, $u_j^{(n+\mathbf{a_j})}$ is the displacement of the $(n+\mathbf{a_j})^{th}$ mass, $\mathbf{a_j}$ is the position vectors of each edge relative to the location of the mass m,

$i = \sqrt{-1}$ and $\boldsymbol{\gamma}$ is the wave vector.

In SC unit cell, 6 springs with stiffness k are attached to the mass m. Displacements of both ends of these springs can be expressed in terms of $\mathbf{u}^{(n)}$ using Equation 3.1. The equation of motion for the mass m is given in Equation 3.2.

$$\begin{aligned}\omega^2 m\mathbf{u}^{(n)} =& k\{R_1[1-e^{i\boldsymbol{\gamma}\cdot\mathbf{a_1}}]\mathbf{u}^{(n)} + R_2[1-e^{i\boldsymbol{\gamma}\cdot\mathbf{a_2}}]\mathbf{u}^{(n)} \\ &+ R_3[1-e^{i\boldsymbol{\gamma}\cdot\mathbf{a_3}}]\mathbf{u}^{(n)} + R_4[1-e^{i\boldsymbol{\gamma}\cdot\mathbf{a_4}}]\mathbf{u}^{(n)} \\ &+ R_5[1-e^{i\boldsymbol{\gamma}\cdot\mathbf{a_5}}]\mathbf{u}^{(n)} + R_6[1-e^{i\boldsymbol{\gamma}\cdot\mathbf{a_6}}]\mathbf{u}^{(n)}\}\end{aligned} \tag{3.2}$$

where $\mathbf{u}^{(n)}$ is the displacement vector for the n^{th} unit cell, $\mathbf{a_j}$ is the vector that gives the position of the end points of the springs k, $\boldsymbol{\gamma}$ is the wave vector, and $\mathbf{R_j} = \mathbf{a_j}\mathbf{a_j}^T/\|\mathbf{a_j}\|^2$.

Equation 3.2 can be simplified as

$$\omega^2 m\mathbf{u}^{(n)} = k\left\{\sum_{j=1}^{6}\mathbf{R_j}(1-e^{i\boldsymbol{\gamma}\cdot\mathbf{a_j}})\right\}\mathbf{u}^{(n)}. \tag{3.3}$$

Phononic band structure of the SC lattice is obtained when Equation 3.3 is solved for ω by using $\boldsymbol{\gamma}$ values on the exterior boundary of Brillouin zone of SC lattice along the path $R-M-\Gamma-X-M$ (see Figure 2.9b). The mass in the unit cell has 3 degrees of freedom. As a result, 3 branches will be present in the phononic band structure.

For any k and m value, a semi-infinite band gap will form above the three branches in the phononic band structure. The band gap starts when the opposite faces of the unit cell move out-of-phase. Consequently, the starting frequency of the band gap can be written as

$$\omega_s = 2\sqrt{\frac{k}{m}}. \tag{3.4}$$

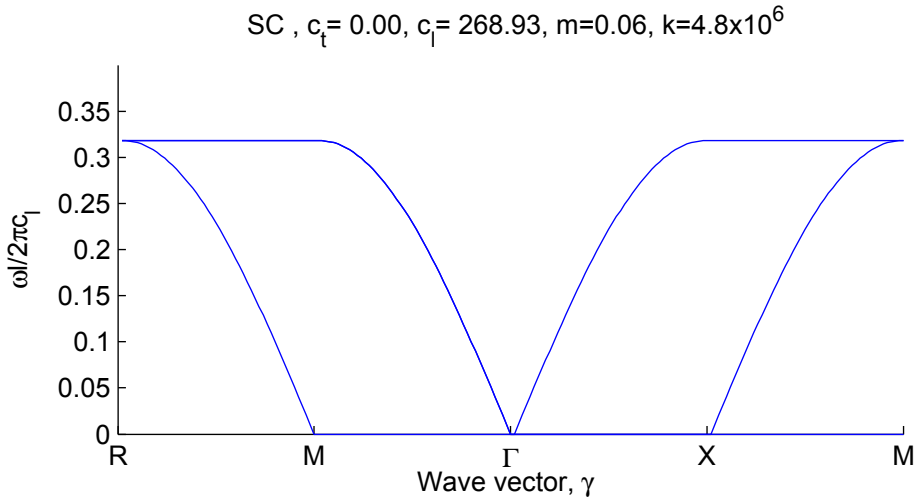


Figure 3.2. Phononic band structure of the SC lattice.

Phononic band structure for this case is shown in Figure 3.2. One can see that there is a semi-infinite band gap starting from the frequency $\omega l/2\pi c_l = 0.318$. Moreover, Equation 3.4 also gives $\omega_s l/2\pi c_l = 0.318$. Also note that the transverse wave speed c_t is zero as the unit cell depicted in Figure 3.1 cannot sustain any transverse load.

3.2. SC Lattice with Inertial Amplification Mechanism

Inertial amplification mechanism seen in Figure 3.3 is added to the SC lattice. When spring elements of the SC lattice are changed with the inertial amplification mechanism without changing overall mass of the unit cell, the starting frequency of semi-infinite band gap is expected to be smaller. First of all, equation of motion of the inertial amplification is derived in order to obtain equation of motion of the SC lattice with inertial amplification mechanism.

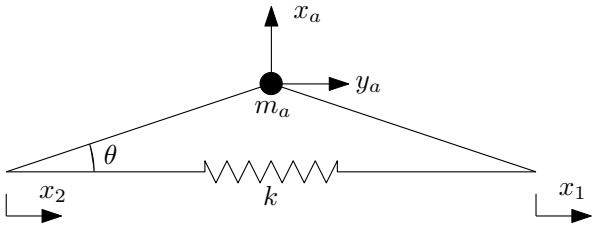


Figure 3.3. Inertial amplification mechanism.

Kinetic and potential energies of the inertial amplification mechanism seen in Figure 3.3 are

$$T = \frac{1}{2} m_a (\dot{x}_a^2 + \dot{y}_a^2) \tag{3.5}$$

and

$$V = \frac{1}{2} k (x_2 - x_1)^2. \tag{3.6}$$

If the terms $y_a = \dfrac{x_1 + x_2}{2}$ and $x_a = \dfrac{x_1 - x_2}{2 \tan\theta}$ are used in Equation 3.5, the kinetic energy of the system will be

$$T = \frac{1}{2} m_a \left(\frac{\dot{x}_1^2 + 2\dot{x}_1\dot{x}_2 + \dot{x}_2^2}{4} + \frac{\dot{x}_1^2 - 2\dot{x}_1\dot{x}_2 + \dot{x}_2^2}{4 \tan^2\theta} \right). \tag{3.7}$$

Then, equation of motion of the inertial amplification mechanism can be obtained from the Euler-Lagrange equation by using $L = T - V$ as

$$\frac{\partial}{\partial t} \left(\frac{\partial L}{\partial \dot{x}_2} \right) - \frac{\partial L}{\partial x_2} = 0 \tag{3.8}$$

where

$$\frac{\partial}{\partial t} \left(\frac{\partial L}{\partial \dot{x}_2} \right) = \frac{1}{8} m_a \left(2\ddot{x}_1 + 2\ddot{x}_2 + \frac{2\ddot{x}_2 - 2\ddot{x}_1}{\tan^2\theta} \right) \tag{3.9}$$

and

$$\frac{\partial L}{\partial x_2} = -k(x_2 - x_1). \tag{3.10}$$

Equation of motion of the inertial amplification mechanism is obtained as

$$\frac{1}{4}m_a\left(\ddot{x}_1+\ddot{x}_2+\frac{\ddot{x}_2-\ddot{x}_1}{\tan^2\theta}\right)+k(x_2-x_1)=0. \tag{3.11}$$

It is possible to apply Bloch theorem to this equation as $x_2=u$ and $x_1=ue^{i\boldsymbol{\gamma}\cdot\mathbf{a_j}}$. Then, equation of motion for the inertial amplification mechanism can be written as

$$\frac{1}{4}m_a\left(\ddot{u}e^{i\boldsymbol{\gamma}\cdot\mathbf{a_j}}+\ddot{u}+\frac{\ddot{u}-\ddot{u}e^{i\boldsymbol{\gamma}\cdot\mathbf{a_j}}}{\tan^2\theta}\right)+k(u-ue^{i\boldsymbol{\gamma}\cdot\mathbf{a_j}})=0 \tag{3.12}$$

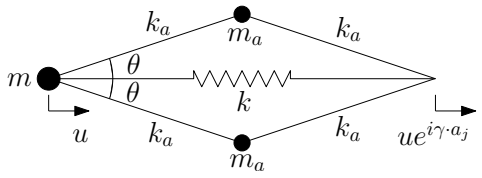


Figure 3.4. Inertial amplification mechanism formed with $2m_a$ and m.

Now, lets consider the inertial amplification mechanism formed with $2m_a$ and m as shown in Figure 3.4. Equation of motion of this system can be easily obtained as

$$\left\{m+\frac{1}{2}m_a\left(e^{i\boldsymbol{\gamma}\cdot\mathbf{a_j}}+1+\frac{1-e^{i\boldsymbol{\gamma}\cdot\mathbf{a_j}}}{\tan^2\theta}\right)\right\}\ddot{u}+k(1-e^{i\boldsymbol{\gamma}\cdot\mathbf{a_j}})u=0. \tag{3.13}$$

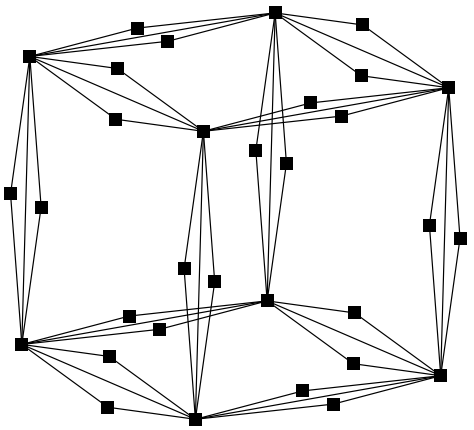


Figure 3.5. SC unit cell with embedded inertial amplification mechanisms.

The k springs in Figure 3.1 are changed with inertial amplification mechanism as shown in Figure 3.4. m in Equation 3.2 is replaced by the effective mass in Equation 3.13 and it is repeated for elements 1 to 6. Equation of motion of the infinitely periodic SC lattice with inertial amplification mechanism (see Figure 3.5) can be written as

$$\omega^2 \left\{ m + \sum_{j=1}^{6} R_j \frac{1}{2} m_a \left(e^{i\boldsymbol{\gamma}\cdot\mathbf{a_j}} + 1 + \frac{1 - e^{i\boldsymbol{\gamma}\cdot\mathbf{a_j}}}{\tan^2\theta} \right) \right\} \mathbf{u}^{(n,1)} + k \left\{ \sum_{j=1}^{6} R_j (1 - e^{i\boldsymbol{\gamma}\cdot\mathbf{a_j}}) \right\} \mathbf{u}^{(n,1)} = 0. \quad (3.14)$$

If Equation 3.14 is solved for ω by using $\boldsymbol{\gamma}$ values on the exterior boundary of Brillouin zone of SC lattice along the path $R - M - \Gamma - X - M$ (see Figure 2.9b), phononic band structure is obtained for the SC lattice with inertial amplification mechanism as seen in Figure 3.6.

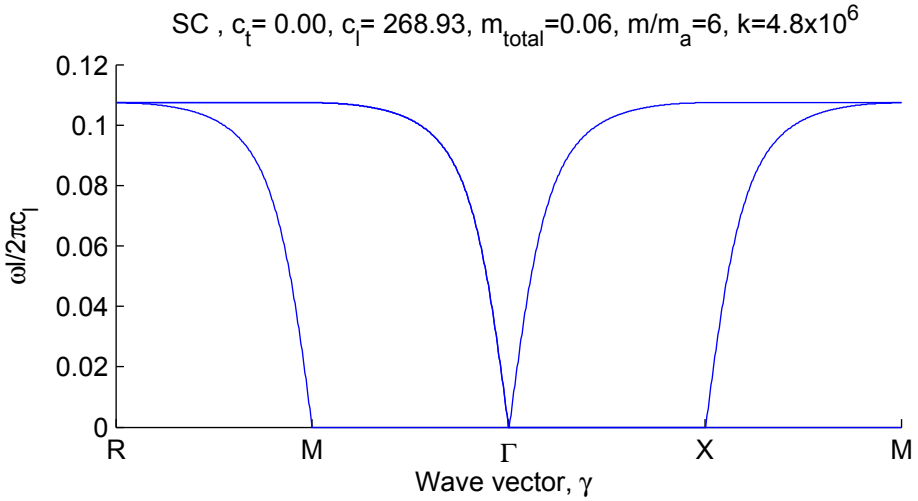


Figure 3.6. Phononic band structure of the SC lattice with inertial amplification mechanism.

If Figure 3.2 and 3.6 are compared, it is seen that starting frequency of band gap decrease from 0.32 to 0.11 with addition of inertial amplification mechanism. Moreover, the total mass of these two structures and wave propagation speed has not changed. Thus, band gap has been started at a lower frequency without changing the total mass

of the system.

For any k, m and m_a value, a semi-infinite band gap will form above the three branches in the phononic band structure. The band gap starts when the opposite faces of the unit cell move out-of-phase. As a result, the starting frequency of the band gap can be obtained as

$$\omega_s = 2\sqrt{\frac{k}{m + \frac{2m_a}{\tan^2\theta}}}. \tag{3.15}$$

In Equation 3.15, for small values of θ, effective inertia of the masses m_a becomes large. Thus, a smaller ω_s value is obtained when compared to Equation 3.4.

To exemplify the effect of inertial amplification half of the unit cell mass is utilized in the amplification mechanisms, while keeping m_{total} constant (see Figure 3.6). One can see that the starting frequency of band gap is decreased from 0.32 to 0.11 with the addition of inertial amplification mechanisms. Equation 3.15 also gives ω_s for this lattice as 0.11. Thus, the starting frequency of the band gap is lowered without changing the total mass of the system. Here, the band gap does not have an upper limit as $k_a \to \infty$. However, if k_a is finite, then there will be an upper limit as

$$\omega_u = \sqrt{\frac{2k_a}{m_a}}\sin(\theta). \tag{3.16}$$

3.3. BCC Lattice

In this section, BCC lattice without inertial amplification mechanism is investigated. Equations of this cubic lattice are derived. Unit cell of a BCC structure is seen in Figure 3.7. Point mass located at the corner is m. Mass located at the center is m_c. Center mass is connected to corners with k_c springs. Stiffness of springs located on the edges are k. Edge length of cube is l.

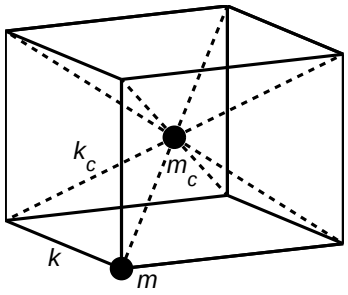


Figure 3.7. Lumped parameter BCC unit cell.

Only m and m_c shown in Figure 3.7 are belong to this unit cell. There are 6 springs with stiffness k and 8 springs with stiffness k_c connected to the mass m. There are 8 springs with stiffness k_c connected to mass m_c. Equation of motion of the mass m and m_c are given in Equations 3.17 and 3.18. In these equations, $\mathbf{u}^{(n,1)}$ and $\mathbf{u}^{(n,2)}$ are displacement vectors of the masses m and m_c in the n^{th} unit cell, $\mathbf{a_j}$ is the vector that gives the position of the end points of the springs k and k_c, $\boldsymbol{\gamma}$ is the wave vector, and $\mathbf{R_j} = \mathbf{a_j}\mathbf{a_j}^T/\|\mathbf{a_j}\|^2$. Also, $\mathbf{u}^{(n+\mathbf{a_j},1)} = e^{i\boldsymbol{\gamma}\cdot\mathbf{a_j}}\mathbf{u}^{(n,1)}$ gives the displacement of the mass m in the unit cell located $\mathbf{a_j}$ away from that unit cell and $\mathbf{u}^{(n+\mathbf{a_j},2)} = e^{i\boldsymbol{\gamma}\cdot\mathbf{a_j}}\mathbf{u}^{(n,2)}$ gives the displacement of the mass m_c in the unit cell located $\mathbf{a_j}$ away from that unit cell.

$$\begin{aligned}
\omega^2 m\mathbf{u}^{(n,1)} =& k\{R_1[1-e^{i\boldsymbol{\gamma}\cdot\mathbf{a_1}}]\mathbf{u}^{(n,1)} + R_2[1-e^{i\boldsymbol{\gamma}\cdot\mathbf{a_2}}]\mathbf{u}^{(n,1)} \\
&+ R_3[1-e^{i\boldsymbol{\gamma}\cdot\mathbf{a_3}}]\mathbf{u}^{(n,1)} + R_4[1-e^{i\boldsymbol{\gamma}\cdot\mathbf{a_4}}]\mathbf{u}^{(n,1)} \\
&+ R_5[1-e^{i\boldsymbol{\gamma}\cdot\mathbf{a_5}}]\mathbf{u}^{(n,1)} + R_6[1-e^{i\boldsymbol{\gamma}\cdot\mathbf{a_6}}]\mathbf{u}^{(n,1)}\} \\
&+ k_c\{R_7[\mathbf{u}^{(n,1)} - e^{i\boldsymbol{\gamma}\cdot\mathbf{a_7}}\mathbf{u}^{(n,2)}] + R_8[\mathbf{u}^{(n,1)} - e^{i\boldsymbol{\gamma}\cdot\mathbf{a_8}}\mathbf{u}^{(n,2)}] \\
&+ R_9[\mathbf{u}^{(n,1)} - e^{i\boldsymbol{\gamma}\cdot\mathbf{a_9}}\mathbf{u}^{(n,2)}] + R_{10}[\mathbf{u}^{(n,1)} - e^{i\boldsymbol{\gamma}\cdot\mathbf{a_{10}}}\mathbf{u}^{(n,2)}] \\
&+ R_{11}[\mathbf{u}^{(n,1)} - e^{i\boldsymbol{\gamma}\cdot\mathbf{a_{11}}}\mathbf{u}^{(n,2)}] + R_{12}[\mathbf{u}^{(n,1)} - e^{i\boldsymbol{\gamma}\cdot\mathbf{a_{12}}}\mathbf{u}^{(n,2)}] \\
&+ R_{13}[\mathbf{u}^{(n,1)} - e^{i\boldsymbol{\gamma}\cdot\mathbf{a_{13}}}\mathbf{u}^{(n,2)}] + R_{14}[\mathbf{u}^{(n,1)} - e^{i\boldsymbol{\gamma}\cdot\mathbf{a_{14}}}\mathbf{u}^{(n,2)}]\}
\end{aligned} \tag{3.17}$$

$$\begin{aligned}
\omega^2 m_c\mathbf{u}^{(n,2)} =& k_c\{R_7[\mathbf{u}^{(n,2)} - e^{i\boldsymbol{\gamma}\cdot\mathbf{a_7}}\mathbf{u}^{(n,1)}] + R_8[\mathbf{u}^{(n,2)} - e^{i\boldsymbol{\gamma}\cdot\mathbf{a_8}}\mathbf{u}^{(n,1)}] \\
&+ R_9[\mathbf{u}^{(n,2)} - e^{i\boldsymbol{\gamma}\cdot\mathbf{a_9}}\mathbf{u}^{(n,1)}] + R_{10}[\mathbf{u}^{(n,2)} - e^{i\boldsymbol{\gamma}\cdot\mathbf{a_{10}}}\mathbf{u}^{(n,1)}] \\
&+ R_{11}[\mathbf{u}^{(n,2)} - e^{i\boldsymbol{\gamma}\cdot\mathbf{a_{11}}}\mathbf{u}^{(n,1)}] + R_{12}[\mathbf{u}^{(n,2)} - e^{i\boldsymbol{\gamma}\cdot\mathbf{a_{12}}}\mathbf{u}^{(n,1)}] \\
&+ R_{13}[\mathbf{u}^{(n,2)} - e^{i\boldsymbol{\gamma}\cdot\mathbf{a_{13}}}\mathbf{u}^{(n,1)}] + R_{14}[\mathbf{u}^{(n,2)} - e^{i\boldsymbol{\gamma}\cdot\mathbf{a_{14}}}\mathbf{u}^{(n,1)}]\}
\end{aligned} \tag{3.18}$$

Equations 3.17 and 3.18 can be simplified as

$$\begin{aligned}\omega^2 m_1 \mathbf{u}^{(\mathbf{n},1)} =& k \left\{ \sum_{j=1}^{6} R_j (1 - e^{i\boldsymbol{\gamma}\cdot\mathbf{a}_j}) \right\} \mathbf{u}^{(\mathbf{n},1)} \\ &+ k_c \left\{ \sum_{j=7}^{14} R_j (\mathbf{u}^{(\mathbf{n},1)} - \mathbf{u}^{(\mathbf{n},2)} e^{i\boldsymbol{\gamma}\cdot\mathbf{a}_j}) \right\}\end{aligned} \tag{3.19}$$

$$\omega^2 m_2 \mathbf{u}^{(\mathbf{n},2)} = k_c \left\{ \sum_{j=7}^{14} R_j (\mathbf{u}^{(\mathbf{n},2)} - \mathbf{u}^{(\mathbf{n},1)} e^{i\boldsymbol{\gamma}\cdot\mathbf{a}_j}) \right\} \tag{3.20}$$

In order to obtain the phononic band structure of the BCC lattice, Equations 3.19 and 3.20 are solved for ω by using $\boldsymbol{\gamma}$ values on the exterior boundary of Brillouin zone of the BCC lattice along the path $N - P - \Gamma - H - P$ (see Figure 2.9c). In the unit cell, there are 2 masses and each mass has 3 degrees of freedom in space. Thus, the unit cell has 6 degrees of freedom. As a result, 6 natural frequencies are obtained for each $\boldsymbol{\gamma}$ value.

In the case of $m_c = \frac{m}{4}$ and $k_c = k$, band gap occurs between $0.540 - 0.712$ as seen in Figure 3.8.

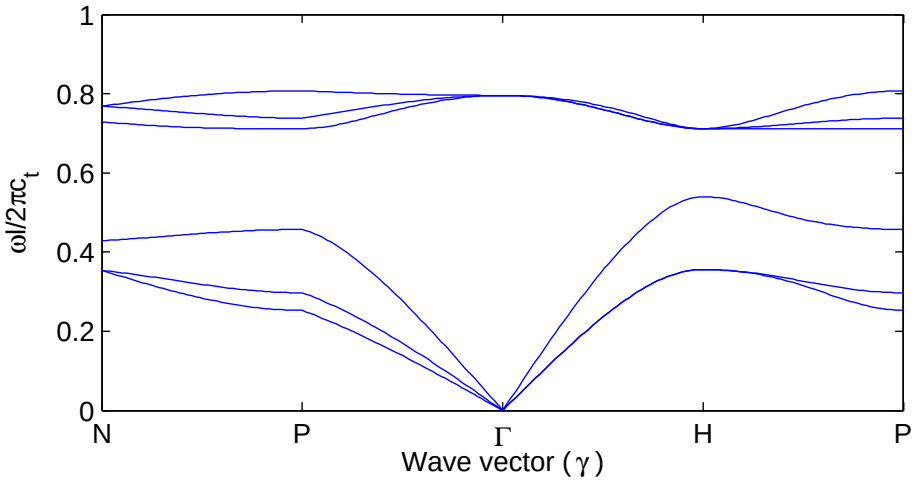


Figure 3.8. Phononic band structure of the BCC lattice in the case of $m_c = m/4$ and $k_c = k$.

Also, BCC structure turn into SC structure if the center mass and stiffness of the springs connected to it goes to zero ($m_c \to 0$, $k_c \to 0$). In Figure 3.9, it is seen that how the phononic band structure of the BCC lattice is changing with decreasing center mass and stiffness of the springs connected to it. Here, Brillouin zone of SC lattice along the path $R - M - \Gamma - X - M$ (see Figure 2.9b) is used.

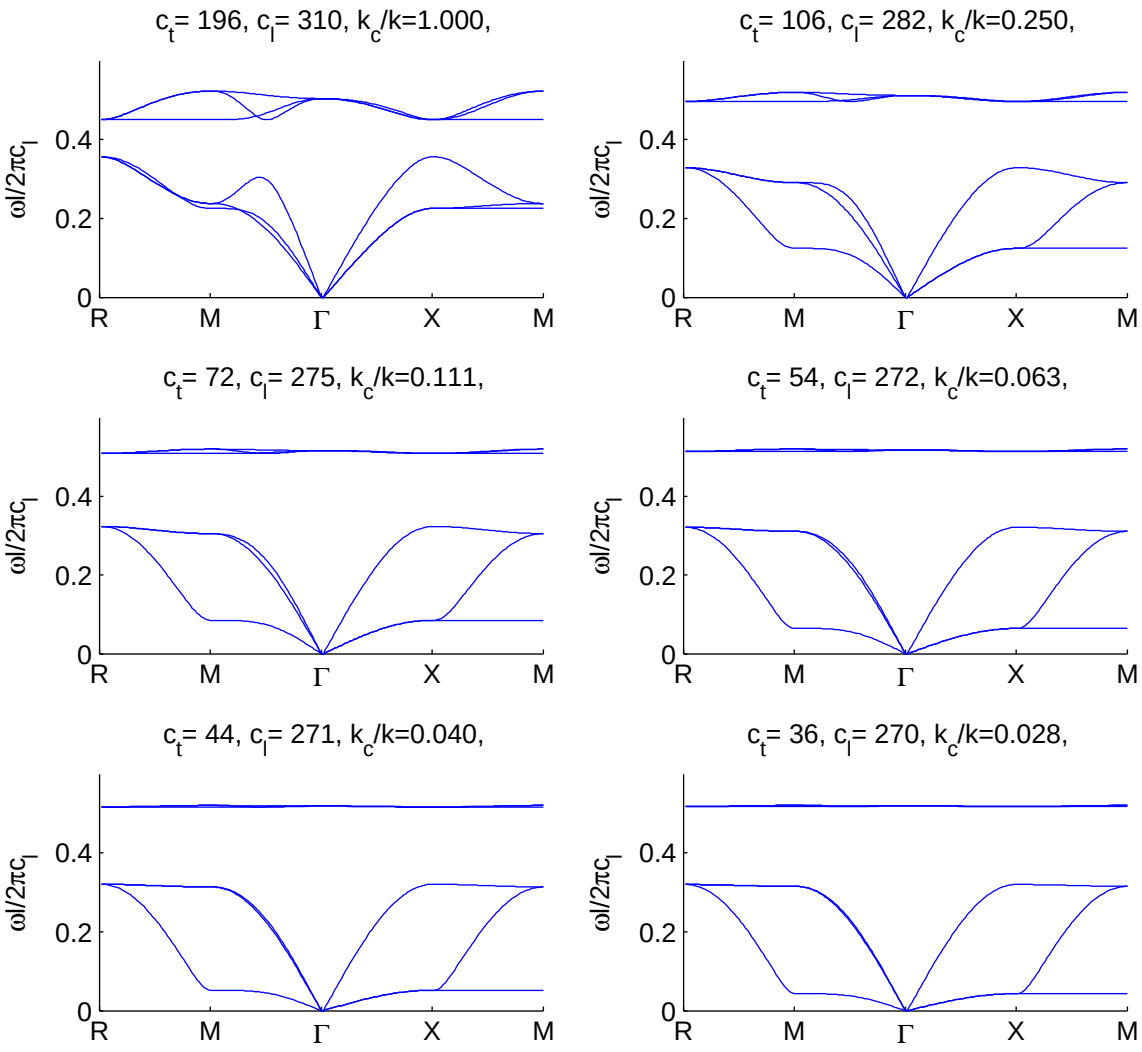


Figure 3.9. Phononic band structure plots for decreasing values of m_c and k_c.

In Figure 3.9, it is seen that transverse wave propagation speed is decreasing with decreasing k_c. Also it is observed that lower limit of the band gap gradually moved to the lower frequency.

For the selected parameters above, normalized bandwidth of the BCC lattice can be found as 0.275. However, as the m_c/m_{total} ratio changes in this lattice, band gap limits and normalized bandwidths will change. To make a detailed comparison, band gap limit and normalized bandwidth of this lattice is calculated as a function of m_c/m_{total} and shown in Figure 3.10. For the BCC lattice, no band gap occurs when m_c/m_{total} ratio is between 0.3 and 0.5. Highest normalized band gap occurs when m_c/m_{total} approaches 0 or 1. But, lower limit of the band gap cannot be below 0.319 for any m_c/m_{total} ratio.

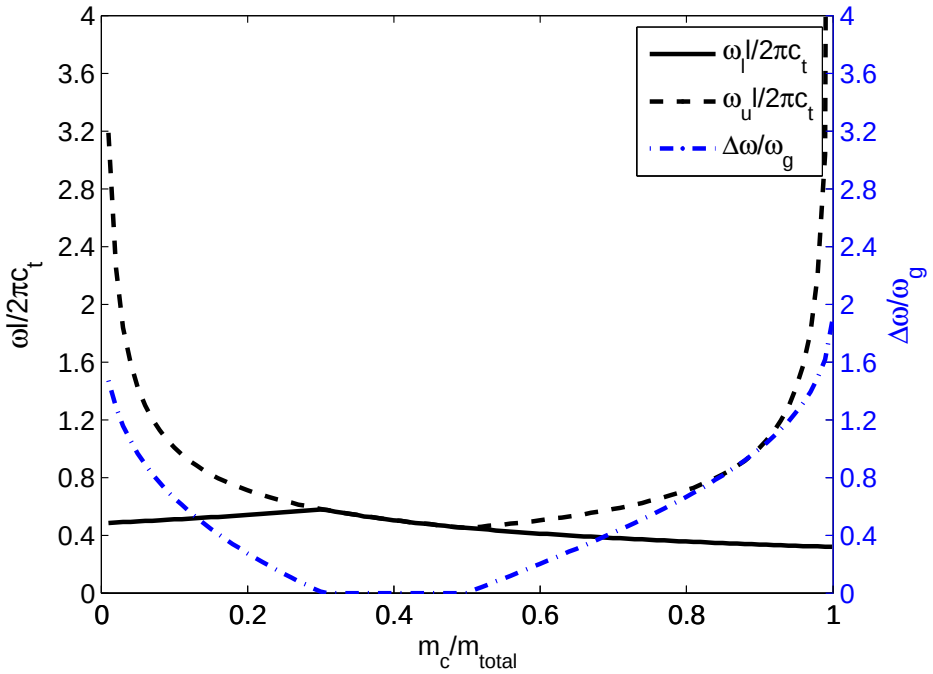


Figure 3.10. Effect of m_c/m_{total} on the band gap of the infinite periodic BCC lattice.

Then, finite periodic model of BCC lattice is created with springs and point masses in order to verify results of the infinite periodic lattice. 4×2×2, 4×4×4 and 8×8×8 arrays of BCC lattice are investigated. 4×2×2 array can be seen Figure 3.11. Excitation and measurement points are also shown in Figure 3.11. 4×4×4 and 8×8×8 arrays are also excited from the center of one face and measurements are performed from the center of opposite face.

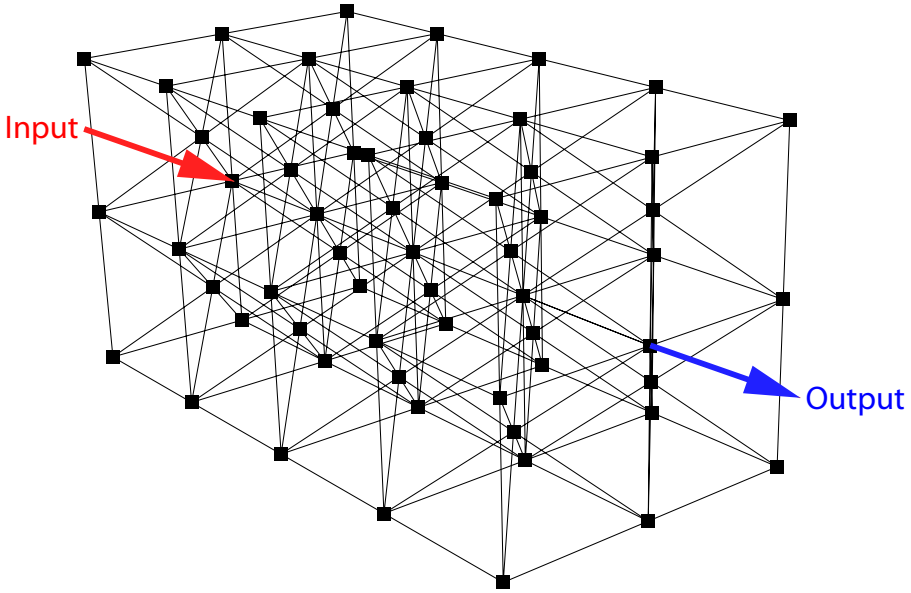


Figure 3.11. 4×2×2 array of BCC unit cells.

Frequency responses of these lattices are quantified by the frequency response function (FRF), which is defined as the output to input displacement amplitude ratio. Frequency range, where $FRF < 1$, is considered as the stop band. Frequency response plot of the 4×2×2 array of BCC unit cells is seen in Figure 3.12. Stop band obtained with this array occurs between $0.605 - 0.790$. Notice that the band gap frequency range of the infinite periodic case was $0.540 - 0.712$ (see Figure 3.8).

Behavior of finite periodic structure approaches the behavior of infinite structure if the number of unit cells in the array is increased along the excitation direction. For this reason, analysis was repeated by increasing the number of elements. First, the number of elements is increased to 64. Frequency response plot obtained from investigation of this 4×4×4 array is seen in Figure 3.12. Band gap obtained with this array occur between $0.582 - 0.735$. These frequencies are closer to the result obtained from the arrangement of infinite number of the unit cells. However, there is still some difference.

Then, the number of elements in each direction is doubled and the 8×8×8 array is investigated. Frequency response plot obtained from investigation of this 8×8×8

array is seen in Figure 3.12. Band gap occurs between $0.545-0.725$. These frequencies are very close to the result obtained for the infinite periodic case. Band gap occurs between $0.545-0.725$ but there is a local peak at 0.576. The reason for that local peak is a surface wave occuring at that frequency. On the other hand, peak height of this resonance is relatively low and it doesn't affect the transmissibility much in band gap.

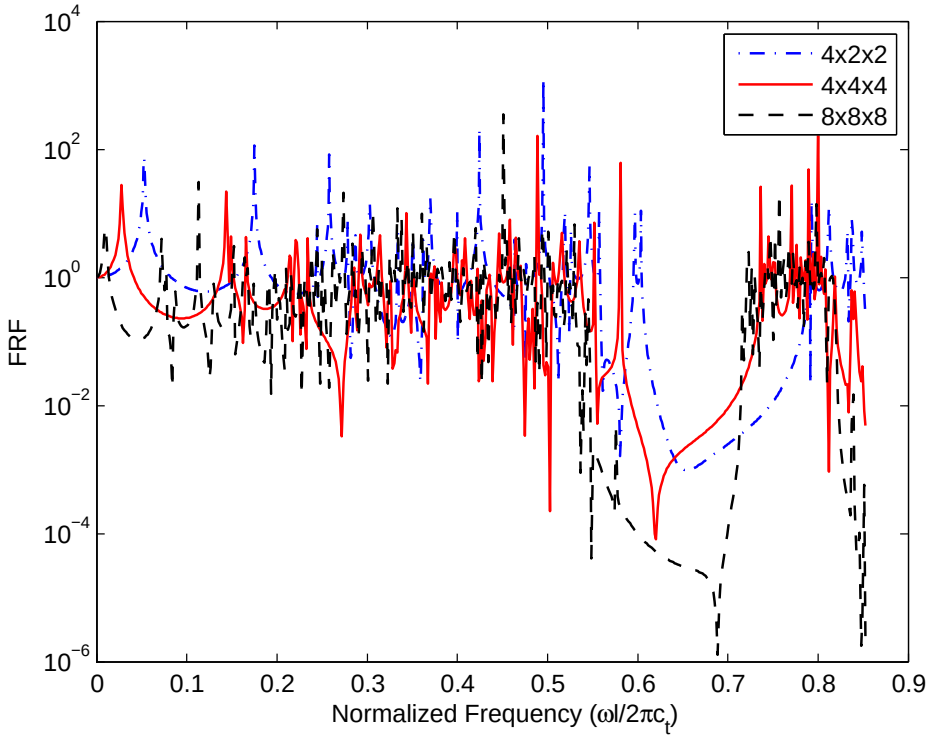


Figure 3.12. Frequency response plots of 4×2×2, 4×4×4 and 8×8×8 arrays of BCC unit cells.

3.4. BCC Lattice with Inertial Amplification Mechanism

In this section, inertial amplification mechanism is added to the BCC structure. k springs seen in Figure 3.7a are changed with the inertial amplification mechanism seen in Figure 3.7b whose length is l. k_c springs are changed with the inertial amplification mechanism whose length is $\frac{\sqrt{3}}{2}l$. Figure 3.13 shows the BCC unit cell with embedded inertial amplification mechanisms.

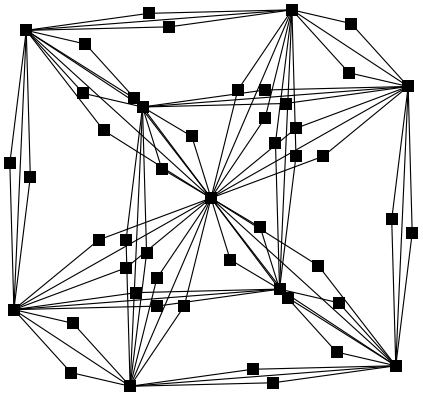


Figure 3.13. BCC unit cell with inertial amplification mechanism.

Equations of motion for the masses m and m_c are similarly obtained as in the SC unit cell by adding the effective inertia of the inertial amplification mechanism as follows:

$$-\omega^2\left\{m+\sum_{j=1}^{6}R_j\frac{1}{2}m_a\left[e^{i\boldsymbol{\gamma}\cdot\mathbf{a_j}}+1+\frac{1-e^{i\boldsymbol{\gamma}\cdot\mathbf{a_j}}}{\tan^2\theta}\right]+\sum_{j=7}^{14}R_j\frac{1}{2}m_a\left[1+\frac{1}{\tan^2\theta}\right]\right\}\mathbf{u}^{(n,1)}$$
$$-\omega^2\sum_{j=7}^{14}R_j\frac{1}{2}m_a\left[e^{i\boldsymbol{\gamma}\cdot\mathbf{a_j}}-\frac{e^{i\boldsymbol{\gamma}\cdot\mathbf{a_j}}}{\tan^2\theta}\right]\mathbf{u}^{(n,2)}+k\left\{\sum_{j=1}^{6}R_j(1-e^{i\boldsymbol{\gamma}\cdot\mathbf{a_j}})\right\}\mathbf{u}^{(n,1)}$$
$$+k_c\left\{\sum_{j=7}^{14}R_j(\mathbf{u}^{(n,1)}-\mathbf{u}^{(n,2)}e^{i\boldsymbol{\gamma}\cdot\mathbf{a_j}})\right\}=0 \quad (3.21)$$

$$-\omega^2\left\{m_c+\sum_{j=7}^{14}R_j\frac{1}{2}m_a\left[1+\frac{1}{\tan^2\theta}\right]\right\}\mathbf{u}^{(n,2)}-\omega^2\left\{\sum_{j=7}^{14}R_j\frac{1}{2}m_a\left[e^{i\boldsymbol{\gamma}\cdot\mathbf{a_j}}-\frac{e^{i\boldsymbol{\gamma}\cdot\mathbf{a_j}}}{\tan^2\theta}\right]\right\}\mathbf{u}^{(n,1)}$$
$$+k_c\left\{\sum_{j=7}^{14}R_j(\mathbf{u}^{(n,2)}-\mathbf{u}^{(n,1)}e^{i\boldsymbol{\gamma}\cdot\mathbf{a_j}})\right\}=0 \quad (3.22)$$

Phononic band structure of the BCC lattice with inertial amplification is obtained when Equations 3.21 and 3.22 are solved for ω by using $\boldsymbol{\gamma}$ values on the exterior boundary of Brillouin zone of BCC lattice along the path $N-P-\Gamma-H-P$ (see Figure 2.9c). The resulting band structure can be seen in Figure 3.14. There is a semi-infinite band gap which is formed above the 6 dispersion curves. Band gap in

Figure 3.8 occurs between $0.540 - 0.712$. Highest frequency in Figure 3.8 is 0.807. All dispersion curves are taken to lower frequencies in Figure 3.14. Here, band gap starting frequency is 0.218. Total mass of systems in Figure 3.8 and 3.14 are the same but the band gap seen in Figure 3.14 starts at much lower frequency and there is no upper limit.

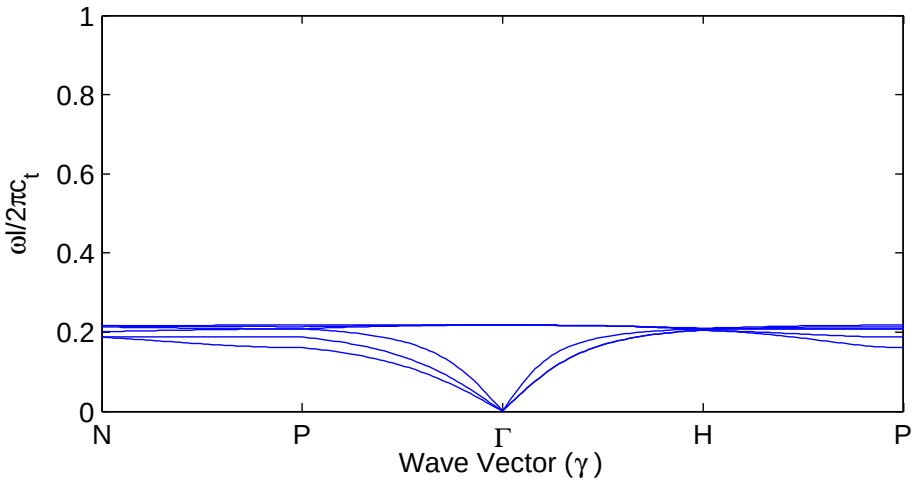


Figure 3.14. Phononic band structure of the BCC lattice with inertial amplification mechanism. Here, band gap starts at 0.218 and there is no upper limit.

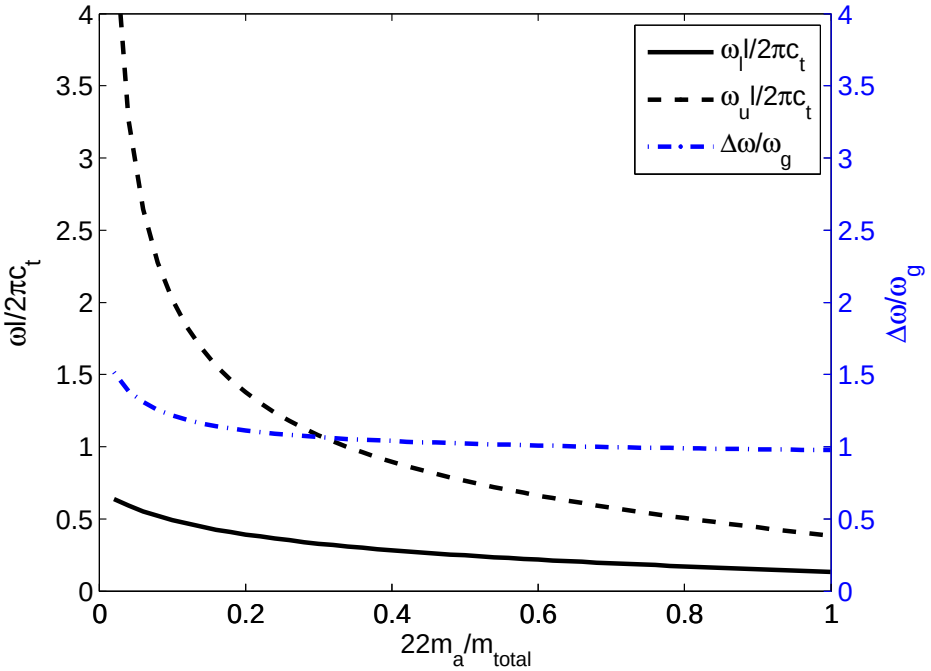


Figure 3.15. Effect of amplifier mass ratio ($22m_a/m_{total}$) on the band gap of the infinite periodic BCC lattice. $k_a/k = 10$, $\theta = \pi/18$ and $m/m_c = 1$.

Figure 3.15 shows the effect of amplifier mass ratio on the band gap of the infinite periodic BCC lattice with inertial amplification mechanism. Here, instead of rigid links, finite stiffness links are used in the inertial amplification mechanisms to show an upper limit for the band gaps. The upper limit is obtained using Equation 3.16. As amplifier mass ratio goes to one, the stop band frequency range becomes quite low, i.e., 0.132-0.383. However, the normalized bandwidth for the BCC lattice converge to 0.977, which is quite large.

Then, finite periodic 4×2×2, 4×4×4 and 8×8×8 BCC lattices with inertial amplification are investigated. These finite models are created with springs and point masses. Figure 3.17 shows the 4×2×2 BCC lattice with inertial amplification. The input and output points are placed in the center of opposite faces as in Figure 3.11.

The frequency responses of 4×2×2, 4×4×4 and 8×8×8 BCC and FCC lattices with inertial amplification are calculated as seen in Figure 3.16.

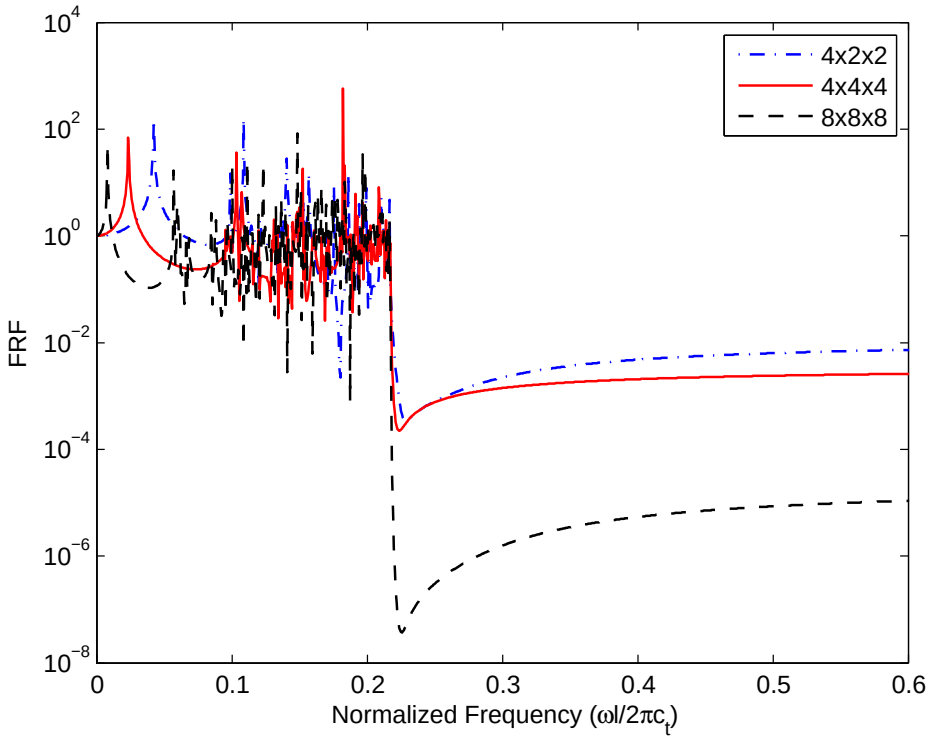
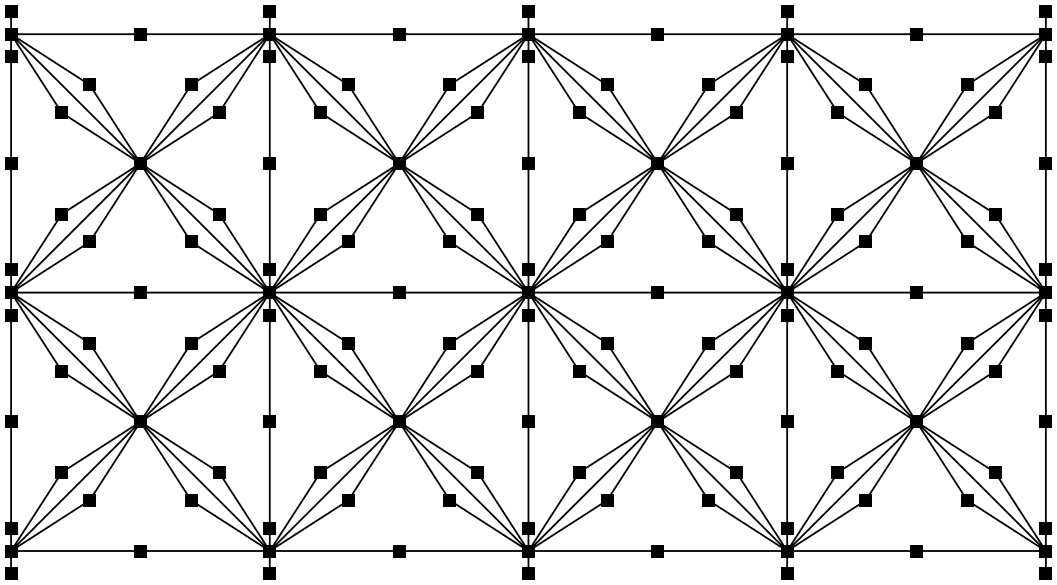
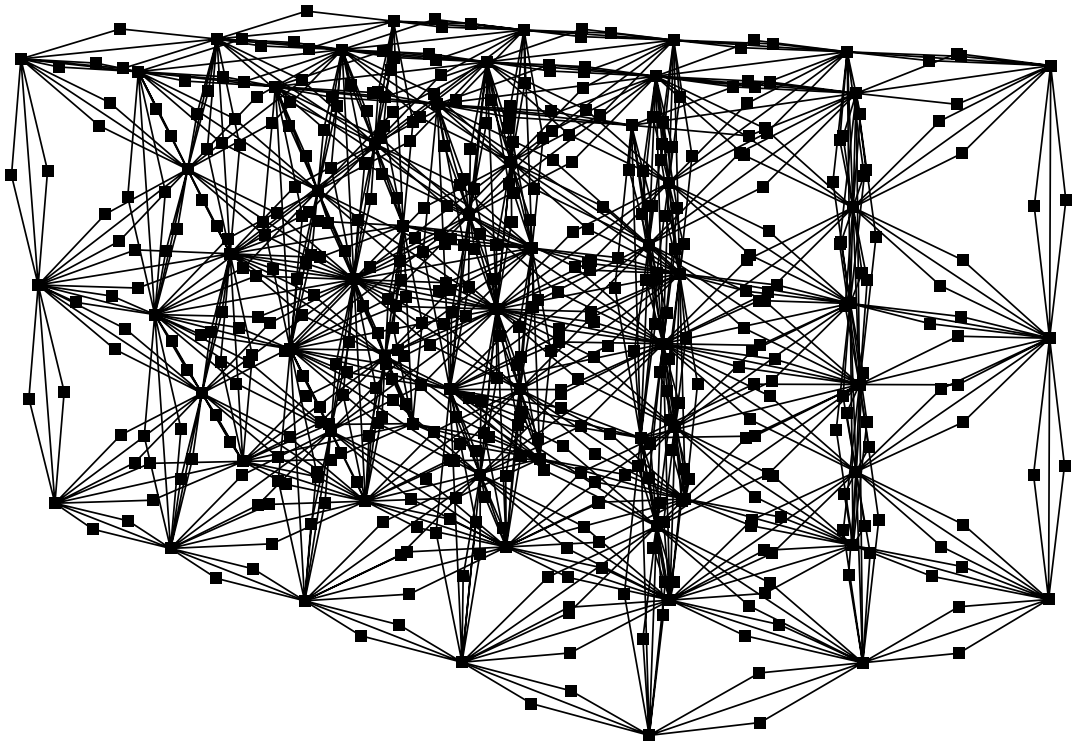


Figure 3.16. Frequency response plots of 4×2×2, 4×4×4 and 8×8×8 arrays of BCC unit cells with inertial amplification mechanism.



(a) Side View



(b) Isometric View

Figure 3.17. 4×2×2 array of BCC unit cells with inertial amplification mechanism.

Band gap starting frequencies of these lattices approach faster to those of the infinite lattices comparing to the lattices without inertial amplification mechanism. Very close results with the infinite lattice is obtained even with 4×2×2 lattice. However, increasing the number of elements especially in the direction of excitation and in the transverse directions affect the depth of the band gap. In Figure 3.16, it is seen that the depth of the band gap is gradually increasing.

Finally, the effect of finite stiffness amplification mechanisms on the upper limit of the stop band is investigated. Figure 3.18 shows the FRF plot for the 8×8×8 BCC lattice, in which the k_a/k ratio is taken as 10. For the BCC lattice, the stop band is formed in the normalized frequency range 0.207-0.661. Note that Equation 3.16 also gives the upper limit as 0.661. Moreover, the normalized bandwidth for the BCC lattice is 1.046. To sum up, wide and deep stop bands are obtained with the use of moderately stiff inertial amplifiers in this lattice.

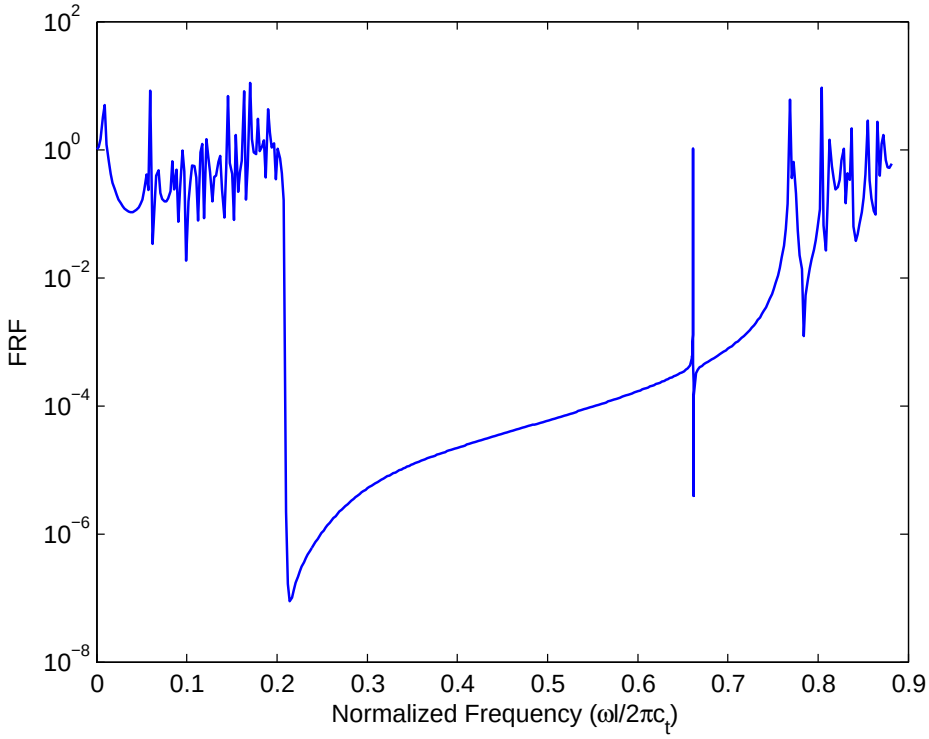


Figure 3.18. FRF plot of the 8×8×8 BCC lattice with inertial amplification where $k_a/k = 10$, $\theta = \pi/18$, $m_c/m_{total} = 1/5$, $m/m_{total} = 1/5$ and $22m_a/m_{total} = 3/5$.

3.5. FCC Lattice

In this section, FCC lattice without inertial amplification mechanism is investigated. Consider the unit cell of the FCC lattice seen in Figure 3.19. If there are infinitely many unit cells, only the masses shown in Figure 3.19 belong to this unit cell. Thus, $m_{total} = m + 3m_c$. Moreover, as in the BCC lattice, it is assumed that stiffness of the springs are inversely proportional to their lengths, hence $k/k_c = \sqrt{2}/2$.

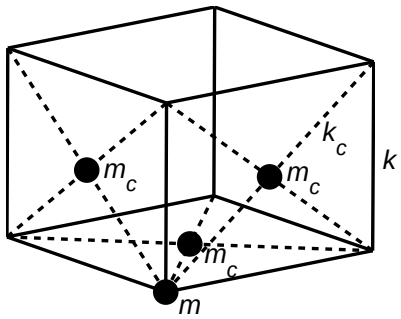


Figure 3.19. FCC unit cell, where m is the corner mass, m_c denotes the face centered masses, k is the stiffness of the edge springs and k_c is the stiffness of the springs between the face centers and the corners. Edge length of the cube is l.

Equations of motion for the masses $m_1 = m$ and $m_2 = m_3 = m_4 = m_c$ are given in Equations 3.23-3.26, respectively.

$$\begin{aligned}
\omega^2 m_1 \mathbf{u}^{(n,1)} =& k\{R_1[1 - e^{i\boldsymbol{\gamma}\cdot\mathbf{a_1}}]\mathbf{u}^{(n,1)} + R_2[1 - e^{i\boldsymbol{\gamma}\cdot\mathbf{a_2}}]\mathbf{u}^{(n,1)} \\
&+ R_3[1 - e^{i\boldsymbol{\gamma}\cdot\mathbf{a_3}}]\mathbf{u}^{(n,1)} + R_4[1 - e^{i\boldsymbol{\gamma}\cdot\mathbf{a_4}}]\mathbf{u}^{(n,1)} \\
&+ R_5[1 - e^{i\boldsymbol{\gamma}\cdot\mathbf{a_5}}]\mathbf{u}^{(n,1)} + R_6[1 - e^{i\boldsymbol{\gamma}\cdot\mathbf{a_6}}]\mathbf{u}^{(n,1)}\} \\
&+ k_c\{R_7[\mathbf{u}^{(n,1)} - e^{i\boldsymbol{\gamma}\cdot\mathbf{a_7}}\mathbf{u}^{(n,2)}] + R_8[\mathbf{u}^{(n,1)} - e^{i\boldsymbol{\gamma}\cdot\mathbf{a_8}}\mathbf{u}^{(n,2)}] \\
&+ R_9[\mathbf{u}^{(n,1)} - e^{i\boldsymbol{\gamma}\cdot\mathbf{a_9}}\mathbf{u}^{(n,2)}] + R_{10}[\mathbf{u}^{(n,1)} - e^{i\boldsymbol{\gamma}\cdot\mathbf{a_{10}}}\mathbf{u}^{(n,2)}] \\
&+ R_{11}[\mathbf{u}^{(n,1)} - e^{i\boldsymbol{\gamma}\cdot\mathbf{a_{11}}}\mathbf{u}^{(n,3)}] + R_{12}[\mathbf{u}^{(n,1)} - e^{i\boldsymbol{\gamma}\cdot\mathbf{a_{12}}}\mathbf{u}^{(n,3)}] \\
&+ R_{13}[\mathbf{u}^{(n,1)} - e^{i\boldsymbol{\gamma}\cdot\mathbf{a_{13}}}\mathbf{u}^{(n,3)}] + R_{14}[\mathbf{u}^{(n,1)} - e^{i\boldsymbol{\gamma}\cdot\mathbf{a_{14}}}\mathbf{u}^{(n,3)}] \\
&+ R_{15}[\mathbf{u}^{(n,1)} - e^{i\boldsymbol{\gamma}\cdot\mathbf{a_{15}}}\mathbf{u}^{(n,4)}] + R_{16}[\mathbf{u}^{(n,1)} - e^{i\boldsymbol{\gamma}\cdot\mathbf{a_{16}}}\mathbf{u}^{(n,4)}] \\
&+ R_{17}[\mathbf{u}^{(n,1)} - e^{i\boldsymbol{\gamma}\cdot\mathbf{a_{17}}}\mathbf{u}^{(n,4)}] + R_{18}[\mathbf{u}^{(n,1)} - e^{i\boldsymbol{\gamma}\cdot\mathbf{a_{18}}}\mathbf{u}^{(n,4)}]\}
\end{aligned} \tag{3.23}$$

$$\begin{aligned}\omega^2 m_2 \mathbf{u}^{(n,2)} =& k_c\{R_7[\mathbf{u}^{(n,2)} - e^{i\boldsymbol{\gamma}\cdot\mathbf{a_7}}\mathbf{u}^{(n,1)}] + R_8[\mathbf{u}^{(n,2)} - e^{i\boldsymbol{\gamma}\cdot\mathbf{a_8}}\mathbf{u}^{(n,1)}] \\ &+ R_9[\mathbf{u}^{(n,2)} - e^{i\boldsymbol{\gamma}\cdot\mathbf{a_9}}\mathbf{u}^{(n,1)}] + R_{10}[\mathbf{u}^{(n,2)} - e^{i\boldsymbol{\gamma}\cdot\mathbf{a_{10}}}\mathbf{u}^{(n,1)}]\}\end{aligned} \tag{3.24}$$

$$\begin{aligned}\omega^2 m_3 \mathbf{u}^{(n,3)} =& k_c\{R_{11}[\mathbf{u}^{(n,3)} - e^{i\boldsymbol{\gamma}\cdot\mathbf{a_{11}}}\mathbf{u}^{(n,1)}] + R_{12}[\mathbf{u}^{(n,3)} - e^{i\boldsymbol{\gamma}\cdot\mathbf{a_{12}}}\mathbf{u}^{(n,1)}] \\ &+ R_{13}[\mathbf{u}^{(n,3)} - e^{i\boldsymbol{\gamma}\cdot\mathbf{a_{13}}}\mathbf{u}^{(n,1)}] + R_{14}[\mathbf{u}^{(n,3)} - e^{i\boldsymbol{\gamma}\cdot\mathbf{a_{14}}}\mathbf{u}^{(n,1)}]\}\end{aligned} \tag{3.25}$$

$$\begin{aligned}\omega^2 m_4 \mathbf{u}^{(n,4)} =& k_c\{R_{15}[\mathbf{u}^{(n,4)} - e^{i\boldsymbol{\gamma}\cdot\mathbf{a_{15}}}\mathbf{u}^{(n,1)}] + R_{16}[\mathbf{u}^{(n,4)} - e^{i\boldsymbol{\gamma}\cdot\mathbf{a_{16}}}\mathbf{u}^{(n,1)}] \\ &+ R_{17}[\mathbf{u}^{(n,4)} - e^{i\boldsymbol{\gamma}\cdot\mathbf{a_{17}}}\mathbf{u}^{(n,1)}] + R_{18}[\mathbf{u}^{(n,4)} - e^{i\boldsymbol{\gamma}\cdot\mathbf{a_{18}}}\mathbf{u}^{(n,1)}]\}\end{aligned} \tag{3.26}$$

Equations 3.23-3.26 can be simplified as

$$\begin{aligned}\omega^2 m_1 \mathbf{u}^{(\mathbf{n},1)} =& k\left(\sum_{j=1}^{6} R_j\left[1 - e^{i\boldsymbol{\gamma}\cdot\mathbf{a}_j}\right]\right)\mathbf{u}^{(\mathbf{n},1)} \\ &+ k_c\left\{\sum_{j=7}^{10} R_j\left[\mathbf{u}^{(\mathbf{n},1)} - \mathbf{u}^{(\mathbf{n},2)}e^{i\boldsymbol{\gamma}\cdot\mathbf{a}_j}\right]\right. \\ &+ \sum_{j=11}^{14} R_j\left[\mathbf{u}^{(\mathbf{n},1)} - \mathbf{u}^{(\mathbf{n},3)}e^{i\boldsymbol{\gamma}\cdot\mathbf{a}_j}\right] \\ &\left.+ \sum_{j=15}^{18} R_j\left[\mathbf{u}^{(\mathbf{n},1)} - \mathbf{u}^{(\mathbf{n},4)}e^{i\boldsymbol{\gamma}\cdot\mathbf{a}_j}\right]\right\}\end{aligned} \tag{3.27}$$

$$\omega^2 m_2 \mathbf{u}^{(\mathbf{n},2)} = k_c\left(\sum_{j=7}^{10} R_j\left[\mathbf{u}^{(\mathbf{n},2)} - \mathbf{u}^{(\mathbf{n},1)}e^{i\boldsymbol{\gamma}\cdot\mathbf{a}_j}\right]\right) \tag{3.28}$$

$$\omega^2 m_3 \mathbf{u}^{(\mathbf{n},3)} = k_c\left(\sum_{j=11}^{14} R_j\left[\mathbf{u}^{(\mathbf{n},3)} - \mathbf{u}^{(\mathbf{n},1)}e^{i\boldsymbol{\gamma}\cdot\mathbf{a}_j}\right]\right) \tag{3.29}$$

$$\omega^2 m_4 \mathbf{u}^{(\mathbf{n},4)} = k_c\left(\sum_{j=15}^{18} R_j\left[\mathbf{u}^{(\mathbf{n},4)} - \mathbf{u}^{(\mathbf{n},1)}e^{i\boldsymbol{\gamma}\cdot\mathbf{a}_j}\right]\right) \tag{3.30}$$

In order to obtain the phononic band structure of the FCC lattice, Equations 3.27-3.30 are solved for ω by using $\boldsymbol{\gamma}$ values on the exterior boundary of Brillouin zone of FCC lattice along the path $X-U-L-\Gamma-X-W-K$ (see Figure 2.9d). In the unit cell, there are 4 masses and each mass has 3 degrees of freedom in space. Thus, the unit cell has 12 degrees of freedom. As a result, 12 natural frequencies are obtained for each $\boldsymbol{\gamma}$ value giving 12 branches in the band structure plot.

m/m_{total} ratio is again taken as 4/5, however, as there are $3m_c$'s in the unit cell, $3m_c/m_{total} = 1/5$. The phononic band structure for this case is computed and shown in Figure 3.20. Here, a band gap is formed in the normalized frequency range 0.635-1.191. Note that, there are two flat branches (each composed of three coinciding branches) at $\omega = 0$ and $\omega l/2\pi c_t = 1.191$ corresponding to the out-of-plane and in-plane resonances of the masses in the face centers, respectively. The in-plane resonance frequency occurs at $\omega = \sqrt{2k_c/m_c}$.

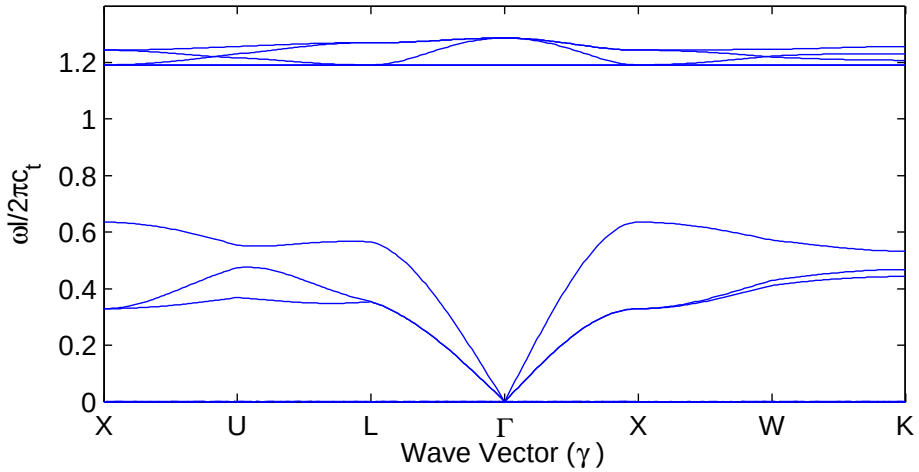


Figure 3.20. Phononic band structure of the FCC lattice. It is seen that there is a band gap between 0.635-1.191 Hz.

For the selected parameters above, normalized bandwidth of the FCC lattice can be found as 0.609. However, as the m_c/m_{total} ratio changes in these lattices, band gap limits and normalized bandwidths will change. To make a detailed comparison, band gap limits and normalized bandwidths of these lattices are calculated as a function of m_c/m_{total} and shown in Figure 3.21. For the FCC lattice, no band gap occurs when

$3m_c/m_{total}$ ratio is above 0.46. Highest normalized band gap occurs when $3m_c/m_{total}$ approaches 0. However, lower limit of the band gap cannot be below 0.589 for any $3m_c/m_{total}$ ratio.

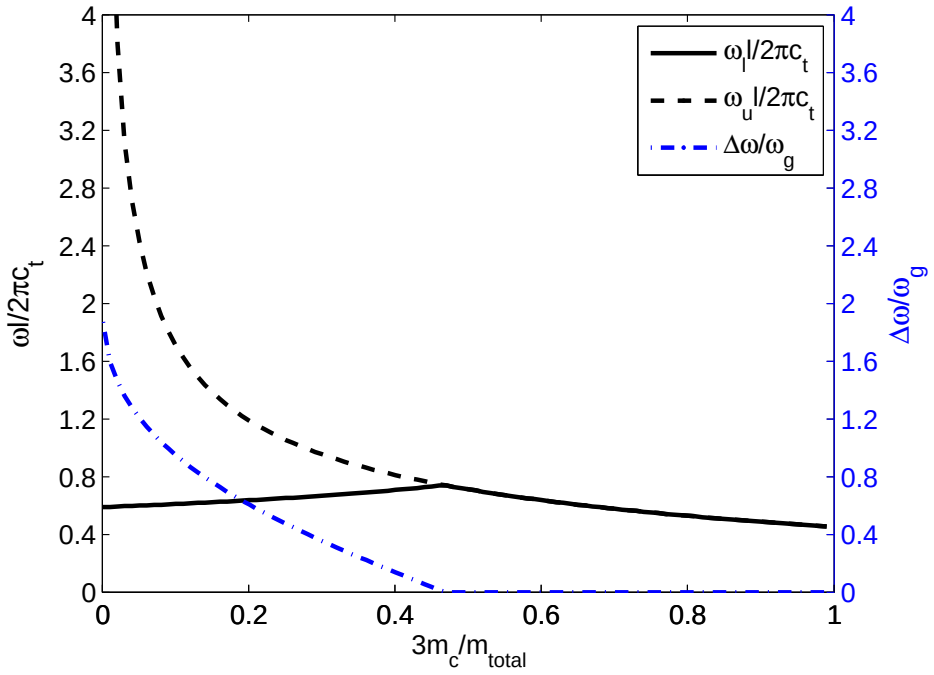


Figure 3.21. Effect of m_c/m_{total} on the band gap of the infinite periodic FCC lattice.

Then, finite periodic FCC lattices composed of 4×2×2, 4×4×4 and 8×8×8 unit cells are considered, and their frequency responses are calculated. The input and output points are similarly placed in the center of opposite faces as in Figure 3.11.

Frequency response plots of 4×2×2, 4×4×4 and 8×8×8 FCC lattices are given in Figure 3.22. Stop bands of the 4×2×2, 4×4×4 and 8×8×8 FCC lattices are formed in the normalized frequency ranges 0.652-1.191, 0.650-1.191 and 0.645-1.191, respectively. Thus, these stop band limits are very close to each other and to those of the infinite periodic case shown in Figure 3.20.

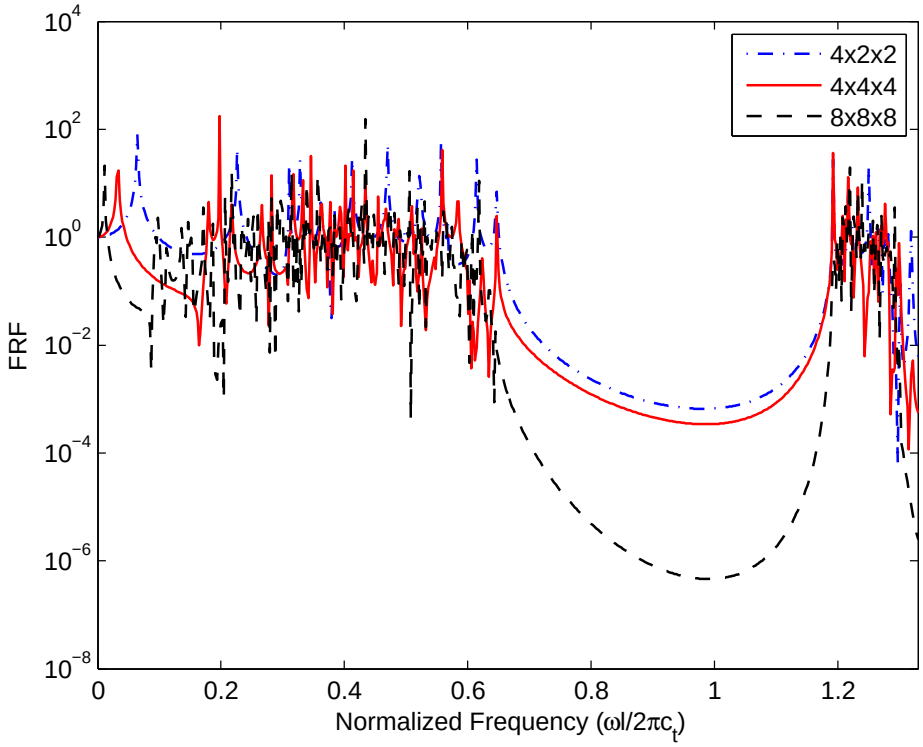
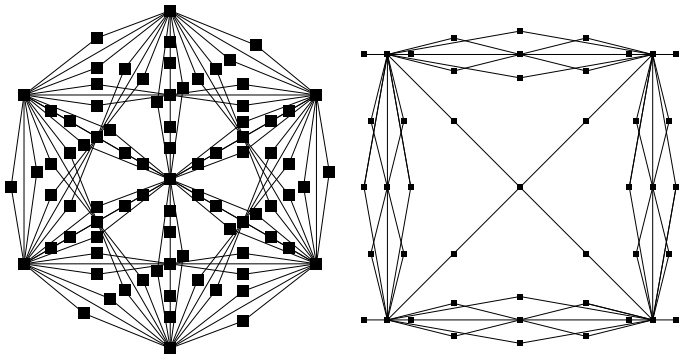


Figure 3.22. Frequency response plots of 4×2×2, 4×4×4 and 8×8×8 arrays of FCC unit cells.

3.6. FCC Lattice with Inertial Amplification Mechanism

In this section, FCC lattice with inertial amplification mechanism is investigated. FCC unit cell with inertial amplification mechanism is shown in Figure 3.23. Inertial amplification mechanisms are added around each spring k and k_c in the FCC unit cell. Due these additions, the static stiffness of the FCC lattice will not change, but its effective inertia will increase as in the BCC lattice.



(a) Isometric View (b) Side View

Figure 3.23. FCC unit cell with inertial amplification mechanism.

Equations of motion for the masses m_1, m_2, m_3 and m_4 are given in Equations 3.31-3.34, respectively. Here, it is assumed that $k_a \to \infty$, so the motion of the masses m_a are coupled to the masses m_1, m_2, m_3 and m_4. There are 24 springs with stiffness k_c in the unit cell and hence 48 m_a's are around these springs. But, these masses are shared with 2 unit cells on each of the 6 faces. There are 12 springs with stiffness k on the edges of each unit cell and hence 24 m_a's are around these springs. But, these masses are shared among 4 unit cells. In total, there are 30 m_a's within each FCC unit cell. As a result, $m_{total} = m + 3m_c + 30m_a$.

$$
\begin{aligned}
-\omega^2 \Bigg\{ \Bigg(m_1 + \sum_{j=1}^{6} R_j \frac{1}{2} m_a \left[e^{i\boldsymbol{\gamma}\cdot\mathbf{a_j}} + 1 + \frac{1 - e^{i\boldsymbol{\gamma}\cdot\mathbf{a_j}}}{\tan^2\theta} \right] \\
+ \sum_{j=7}^{18} R_j \frac{1}{2} m_a \left[1 + \frac{1}{\tan^2\theta} \right] \Bigg) \mathbf{u}^{(n,1)} \\
+ \left(\sum_{j=7}^{10} R_j \frac{1}{2} m_a \left[e^{i\boldsymbol{\gamma}\cdot\mathbf{a_j}} - \frac{e^{i\boldsymbol{\gamma}\cdot\mathbf{a_j}}}{\tan^2\theta} \right] \right) \mathbf{u}^{(n,2)} \\
+ \left(\sum_{j=11}^{14} R_j \frac{1}{2} m_a \left[e^{i\boldsymbol{\gamma}\cdot\mathbf{a_j}} - \frac{e^{i\boldsymbol{\gamma}\cdot\mathbf{a_j}}}{\tan^2\theta} \right] \right) \mathbf{u}^{(n,3)} \\
+ \left(\sum_{j=15}^{18} R_j \frac{1}{2} m_a \left[e^{i\boldsymbol{\gamma}\cdot\mathbf{a_j}} - \frac{e^{i\boldsymbol{\gamma}\cdot\mathbf{a_j}}}{\tan^2\theta} \right] \right) \mathbf{u}^{(n,4)} \Bigg\} \\
+ k \left(\sum_{j=1}^{6} R_j \left[1 - e^{i\boldsymbol{\gamma}\cdot\mathbf{a_j}} \right] \right) \mathbf{u}^{(n,1)} + k_c \Bigg\{ \sum_{j=7}^{10} R_j \left[\mathbf{u}^{(n,1)} - \mathbf{u}^{(n,2)} e^{i\boldsymbol{\gamma}\cdot\mathbf{a_j}} \right] \\
+ \sum_{j=11}^{14} R_j \left[\mathbf{u}^{(n,1)} - \mathbf{u}^{(n,3)} e^{i\boldsymbol{\gamma}\cdot\mathbf{a_j}} \right] + \sum_{j=15}^{18} R_j \left[\mathbf{u}^{(n,1)} - \mathbf{u}^{(n,4)} e^{i\boldsymbol{\gamma}\cdot\mathbf{a_j}} \right] \Bigg\} = 0
\end{aligned}
\tag{3.31}
$$

$$
\begin{aligned}
-\omega^2 \Bigg\{ \Bigg(m_2 + \sum_{j=7}^{10} R_j \frac{1}{2} m_a \left[1 + \frac{1}{\tan^2\theta} \right] \Bigg) \mathbf{u}^{(n,2)} \\
+ \left(\sum_{j=7}^{10} R_j \frac{1}{2} m_a \left[e^{i\boldsymbol{\gamma}\cdot\mathbf{a_j}} - \frac{e^{i\boldsymbol{\gamma}\cdot\mathbf{a_j}}}{\tan^2\theta} \right] \right) \Bigg\} \mathbf{u}^{(n,1)} \\
+ k_c \left(\sum_{j=7}^{10} R_j \left[\mathbf{u}^{(n,2)} - \mathbf{u}^{(n,1)} e^{i\boldsymbol{\gamma}\cdot\mathbf{a_j}} \right] \right) = 0
\end{aligned}
\tag{3.32}
$$

$$-\omega^2\left\{\left(m_3+\sum_{j=11}^{14}R_j\frac{1}{2}m_a\left[1+\frac{1}{\tan^2\theta}\right]\right)\mathbf{u}^{(n,3)}+\left(\sum_{j=11}^{14}R_j\frac{1}{2}m_a\left[e^{i\boldsymbol{\gamma}\cdot\mathbf{a_j}}-\frac{e^{i\boldsymbol{\gamma}\cdot\mathbf{a_j}}}{\tan^2\theta}\right]\right)\right\}\mathbf{u}^{(n,1)}+k_c\left(\sum_{j=11}^{14}R_j\left[\mathbf{u}^{(n,3)}-\mathbf{u}^{(n,1)}e^{i\boldsymbol{\gamma}\cdot\mathbf{a_j}}\right]\right)=0 \quad (3.33)$$

$$-\omega^2\left\{\left(m_4+\sum_{j=15}^{18}R_j\frac{1}{2}m_a\left[1+\frac{1}{\tan^2\theta}\right]\right)\mathbf{u}^{(n,4)}+\left(\sum_{j=15}^{18}R_j\frac{1}{2}m_a\left[e^{i\boldsymbol{\gamma}\cdot\mathbf{a_j}}-\frac{e^{i\boldsymbol{\gamma}\cdot\mathbf{a_j}}}{\tan^2\theta}\right]\right)\right\}\mathbf{u}^{(n,1)}+k_c\left(\sum_{j=15}^{18}R_j\left[\mathbf{u}^{(n,4)}-\mathbf{u}^{(n,1)}e^{i\boldsymbol{\gamma}\cdot\mathbf{a_j}}\right]\right)=0 \quad (3.34)$$

Phononic band structure of the FCC lattice with inertial amplification is obtained as seen in Figure 3.24 when Equations 3.31-3.34 are solved for ω by using $\boldsymbol{\gamma}$ values on the exterior boundary of Brillouin zone of FCC lattice along the path $X-U-L-\Gamma-X-W-K$ (see Figure 2.9d).

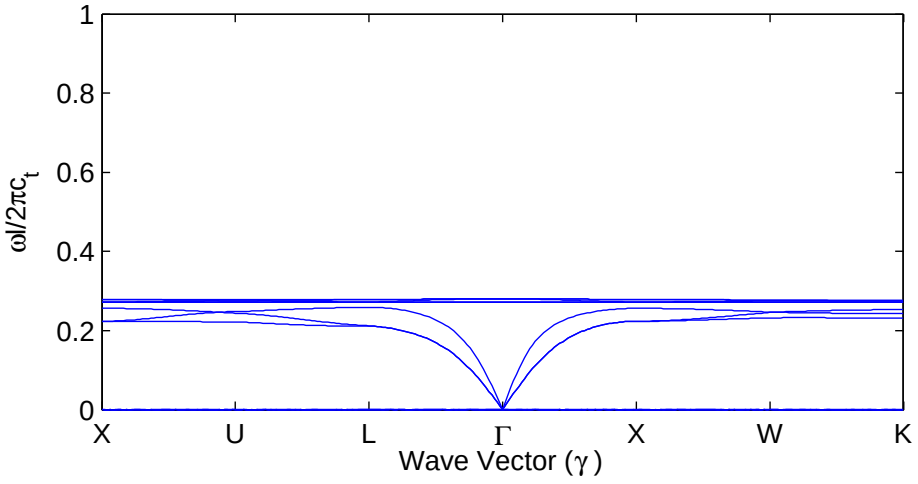


Figure 3.24. Phononic band structure of the FCC lattice with inertial amplification mechanism.

Consider the case where $3m_c/m_{total} = 1/5$, $m/m_{total} = 1/5$ and $30m_a/m_{total} = 3/5$. The phononic band structure for this case is shown in Figure 3.24, in which there is a semi-infinite band gap above the 12 branches. In Figure 3.20, band gap occurs between the 6^{th} and the 7^{th} branches in the normalized frequency range 0.635-1.191. Moreover, the highest frequency in Figure 3.20 is 1.287. In Figure 3.24, due to inertial amplification, all 12 branches are suppressed to lower frequencies so that the semi-infinite band gap starts at 0.281.

The effect of amplifier mass ratio on the band gap of the infinite periodic FCC lattice with inertial amplification is shown in Figure 3.25. Here, instead of rigid links, finite stiffness links are used in the inertial amplification mechanisms to show an upper limit for the band gaps. The upper limit is obtained using Equation 3.16. As amplifier mass ratio goes to one, the stop band frequency ranges become quite low, i.e., 0.177-0.466. However, the normalized bandwidth for the FCC lattice converge to 0.897, which is quite large.

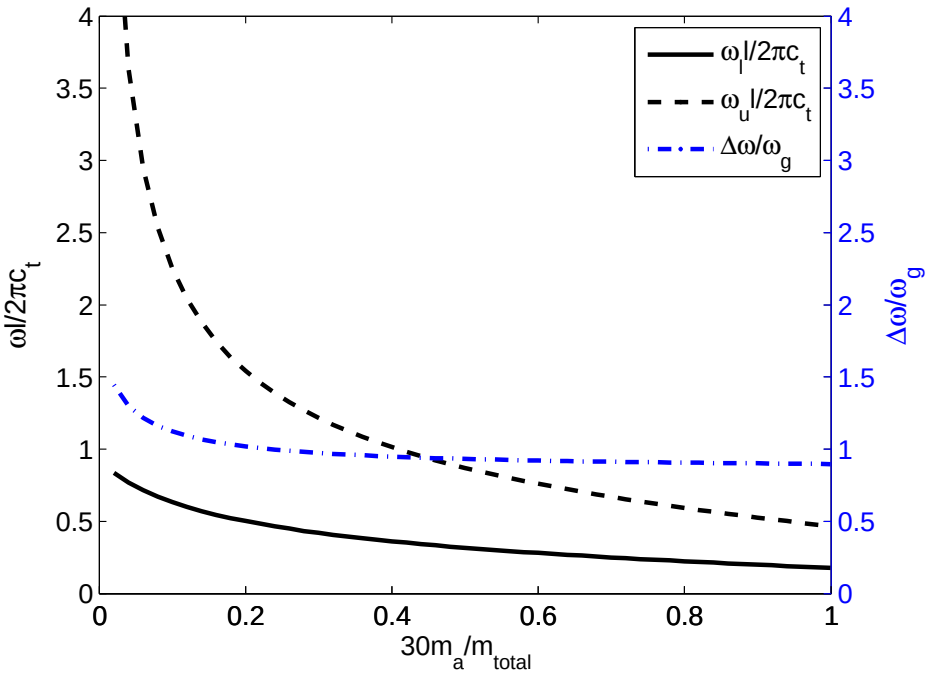


Figure 3.25. Effect of amplifier mass ratio ($30m_a/m_{total}$) on the band gap of the infinite periodic FCC lattice. $k_a/k = 10$, $\theta = \pi/18$ and $m/3m_c = 1$.

Finite periodic FCC lattices with inertial amplification are considered in this

section. The frequency responses of 4×2×2, 4×4×4 and 8×8×8 FCC lattices with inertial amplification are calculated. The input and output points are also placed in the center of opposite faces of the FCC lattices as in Figure 3.11.

Frequency response plots of 4×2×2, 4×4×4 and 8×8×8 FCC lattices are given in Figure 3.26. Lower limits of the stop bands for the 4×2×2, 4×4×4 and 8×8×8 FCC lattices are at 0.278, 0.279 and 0.280, respectively. Thus, all the FCC stop band lower limits are very close to those of the infinite periodic case. However, the depth of the stop bands increase as the number of unit cells in these lattices increase, especially along the excitation direction. Furthermore, as $k_a/k \to \infty$, there is no upper limit for the stop bands.

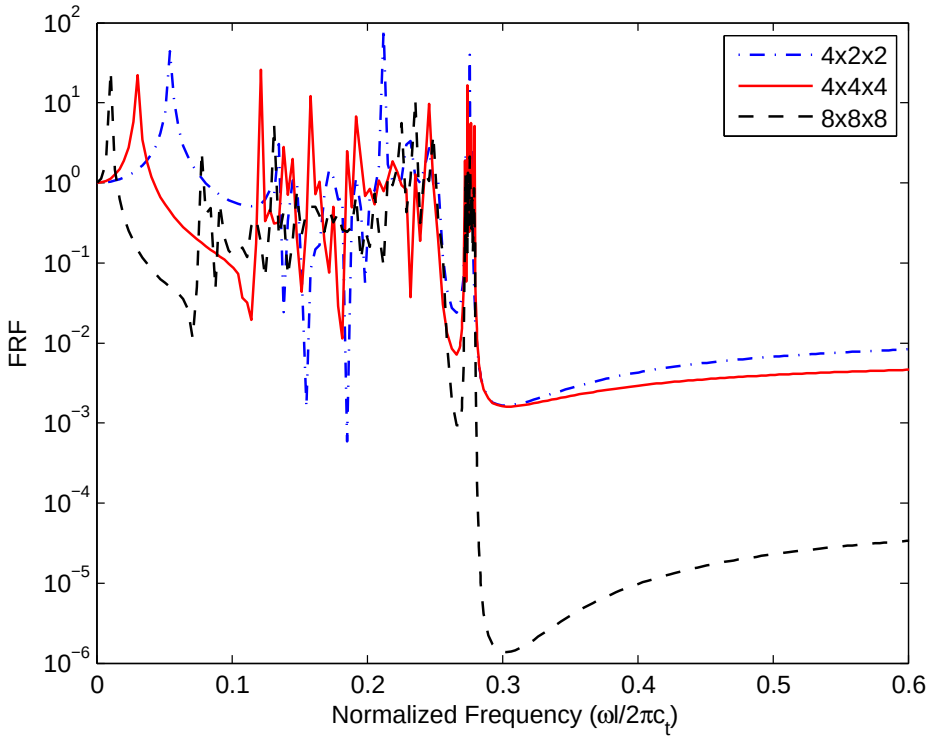


Figure 3.26. Frequency response plots of 4×2×2, 4×4×4 and 8×8×8 arrays of FCC unit cells with inertial amplification mechanism.

Finally, the effect of finite stiffness amplification mechanisms on the stop band limit of the FCC lattice is investigated. Figure 3.27 shows the FRF plot for the 8×8×8 FCC lattice, in which the k_a/k ratio is taken as 10. For the FCC lattice, the stop band is formed in the normalized frequency range $0.263 - 0.759$. Note that Equation

3.16 also gives the upper limit as 0.759. Moreover, the normalized bandwidth for the FCC lattice is 0.971. To sum up, wide and deep stop band is obtained with the use of moderately stiff inertial amplifiers in the FCC lattice.

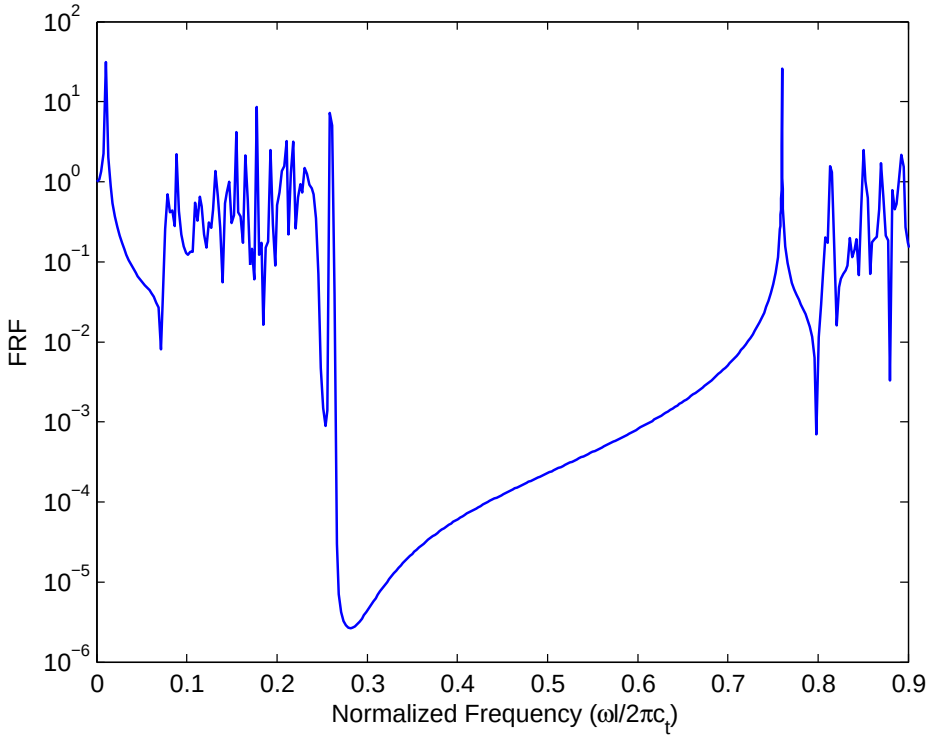


Figure 3.27. FRF plot of the 8×8×8 FCC lattice with inertial amplification where $k_a/k = 10$, $\theta = \pi/18$, $3m_c/m_{total} = 1/5$, $m/m_{total} = 1/5$ and $30m_a/m_{total} = 3/5$.

4. DESIGN AND ANALYSIS OF 3D DISTRIBUTED PARAMETER MODELS

In this chapter, 3D structures are formed using distributed parameter inertial amplification mechanisms. First, a BCC lattice is created using inertial amplification mechanisms. The BCC lattice is required to design two inertial amplification mechanisms with different lengths which have the same band gap properties. Since the aim of this study is to obtain wide low frequency band gaps, it is hard to optimize two different mechanisms for wide band gaps at the same frequency range. In order to overcome this problem, octahedron structure is also investigated since it can be formed using identical inertial amplification mechanisms.

4.1. BCC Lattice

In [46], a distributed parameter inertial amplification mechanism is designed and analyzed. However, a 2D structure is built which is capable of isolating only in-plane vibrations. In this section, BCC lattice is built which can isolate vibrations also in the out-of-plane direction. So, finite element analysis will be performed using 3D shell elements in order to investigate out-of-plane modes during design process. In order to create BCC lattice using distributed parameter inertial amplification mechanisms, it is required to design two building block inertial amplification mechanisms with length l and $\frac{\sqrt{3}}{2}l$. First, two building blocks of the BCC lattice are designed which have similar stop band limits. Then, BCC lattice is formed using these building blocks and its stop band is investigated.

4.1.1. Design of the Building Block Mechanisms

Figure 4.1 shows the parameters of the building block inertial amplification mechanism. These parameters will be modified in order obtain two mechanisms with different lengths but similar stop bands.

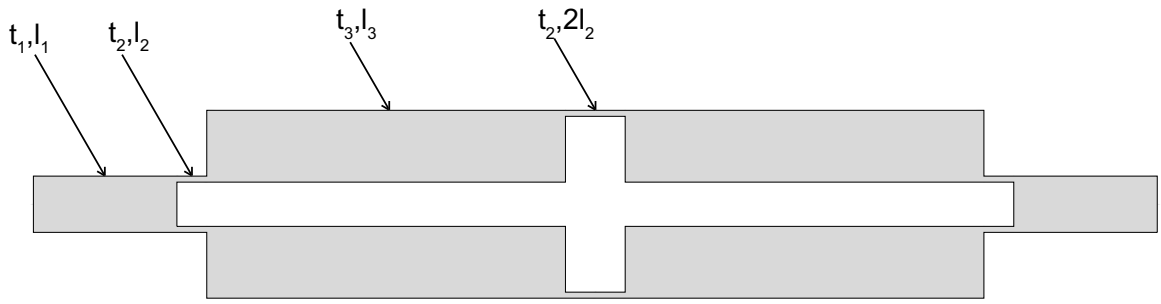
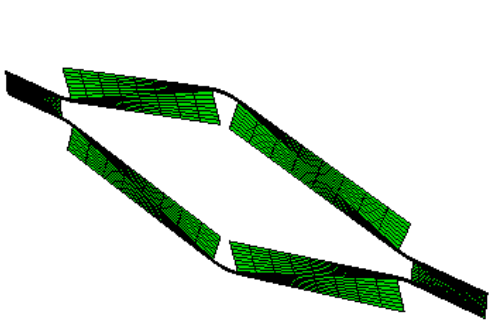


Figure 4.1. Inertial amplification mechanism. Here, l_i and t_i are length and thickness of the ith beam for $i = 1, 2, 3$.

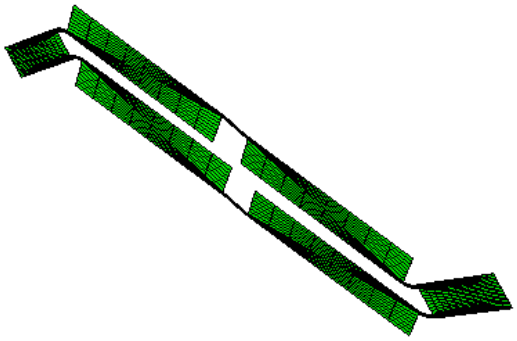
First, a mechanism with length $\frac{\sqrt{3}}{2}l$ is designed. Parameters of this mechanism are $t_1 = 4.7$mm, $l_1 = 12$mm, $t_2 = 0.5$mm, $l_2 = 2.5$mm, $t_3 = 6$mm and $l_3 = 30$mm. Modal analysis of the mechanism is performed with a commercial finite element software (ABAQUS). 4 node shell elements (S4) are used in this analysis. Pinned and roller boundary conditions are applied to left and right ends of the mechanism . First 4 mode shapes of the mechanism are given in Figure 4.2a-d. In-plane modes are seen in Figure 4.2a-c and out-of-plane mode is seen in Figure 4.2d.

Consequently, frequency response analysis is performed in order to see transmission of vibration from one end to other. Roller boundary conditions are applied to the end points and 4 node shell elements (S4) are used for this analysis. Frequency response plot of the mechanism is seen in Figure 4.2e. Here, it is seen that there is a band gap between the first and second natural frequencies.

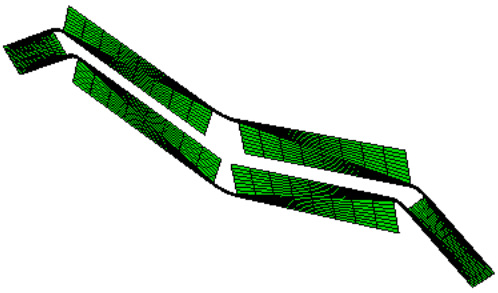
Secondly, a mechanism with length l is designed. In this new mechanism, first and second modes need to be placed at the same frequencies with those of the first mechanism. Parameters of this mechanism are $t_1 = 5.4$mm, $l_1 = 13.9$mm, $t_2 = 0.57$mm, $l_2 = 1.8$mm, $t_3 = 6.9$mm and $l_3 = 37$mm. First 4 mode shapes of this mechanism are seen in Figure 4.3a-d. Band gaps of these mechanisms occur between the first and second natural frequencies. Band gap of the BCC structure built with these mechanisms are expected to coincide with the band gaps of building block mechanisms.



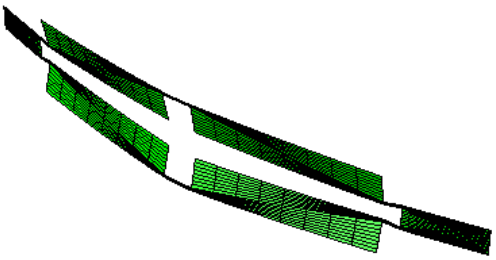
(a) $\omega_1 = 263$ Hz



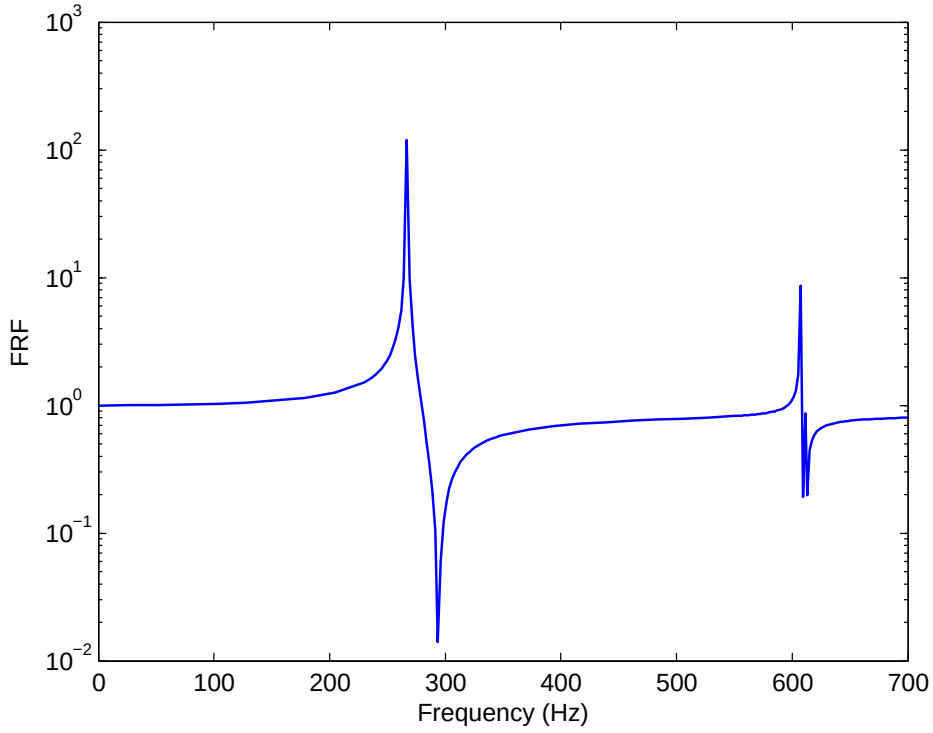
(b) $\omega_2 = 600$ Hz



(c) $\omega_3 = 604$ Hz

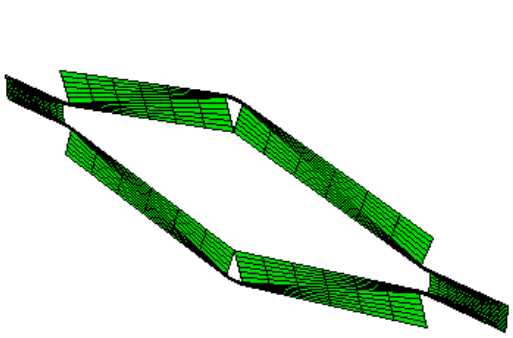


(d) $\omega_4 = 860$ Hz

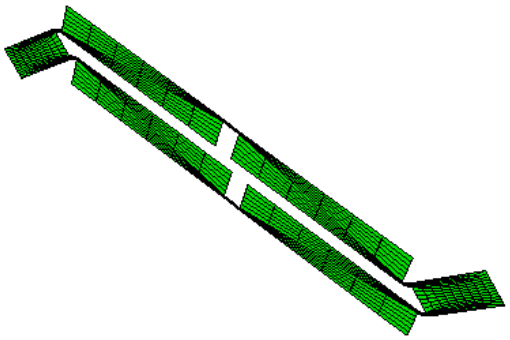


(e)

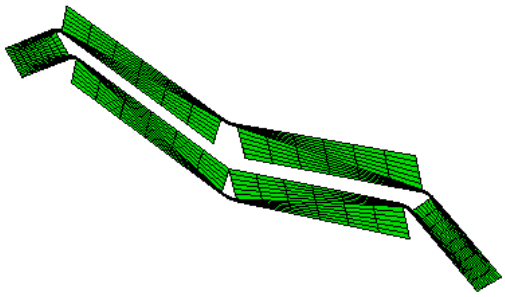
Figure 4.2. (a-d) First 4 mode shapes of the inertial amplification mechanism with length $\sqrt{3}l/2$. (e) Frequency response of the mechanism with length $\sqrt{3}l/2$.



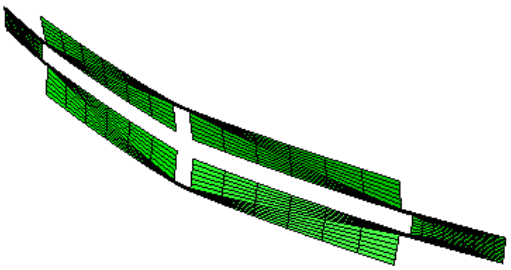
(a) $\omega_1 = 265$ Hz



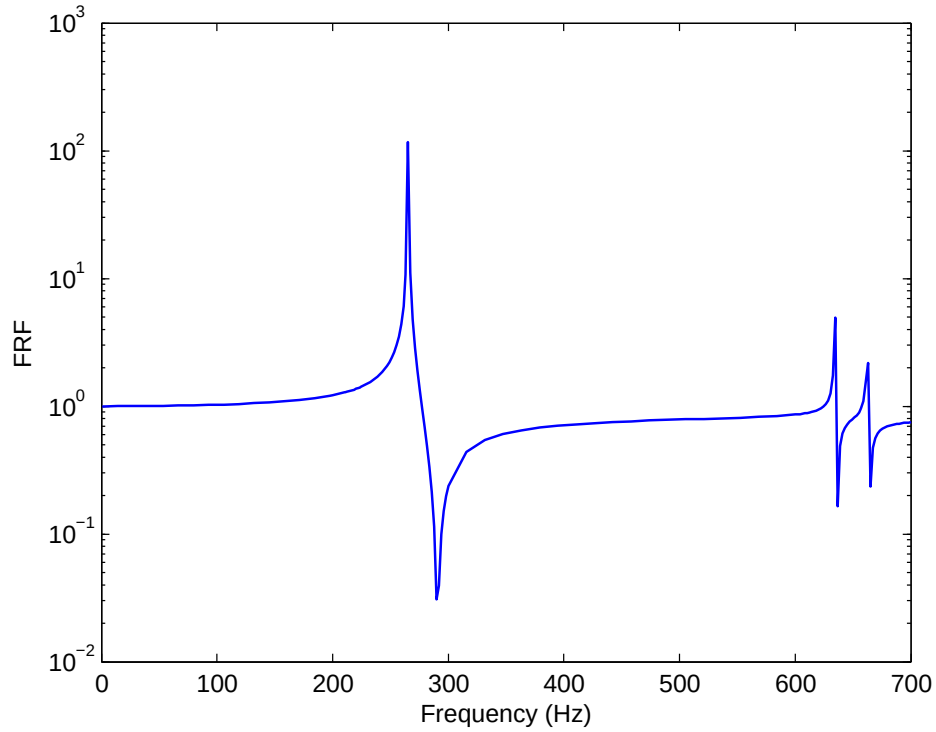
(b) $\omega_2 = 636$ Hz



(c) $\omega_3 = 664$ Hz



(d) $\omega_4 = 711$ Hz



(e)

Figure 4.3. (a-d) First 4 mode shapes of the inertial amplification mechanism with length l. (e) Frequency response of the mechanism with length l.

Frequency response plot of the mechanism with length l is also given in Figure 4.3e. There is a band gap between the first and second natural frequencies. First natural frequencies of the mechanisms with length l and $\frac{\sqrt{3}}{2}l$ are the same but there is small difference between the second natural frequencies. Thus, band gaps of these mechanisms which are used to build the body-centered cubic structure are quite closer to each other.

4.1.2. Distributed Parameter Model of the BCC Lattice

In the previous chapter, lumped parameter model of the BCC lattice is investigated. Now, it is created using distributed parameter inertial amplification mechanisms. The model of BCC lattice can be seen in Figure 4.4. It is formed by using the mechanisms with the lengths l and $\sqrt{3}l/2$.

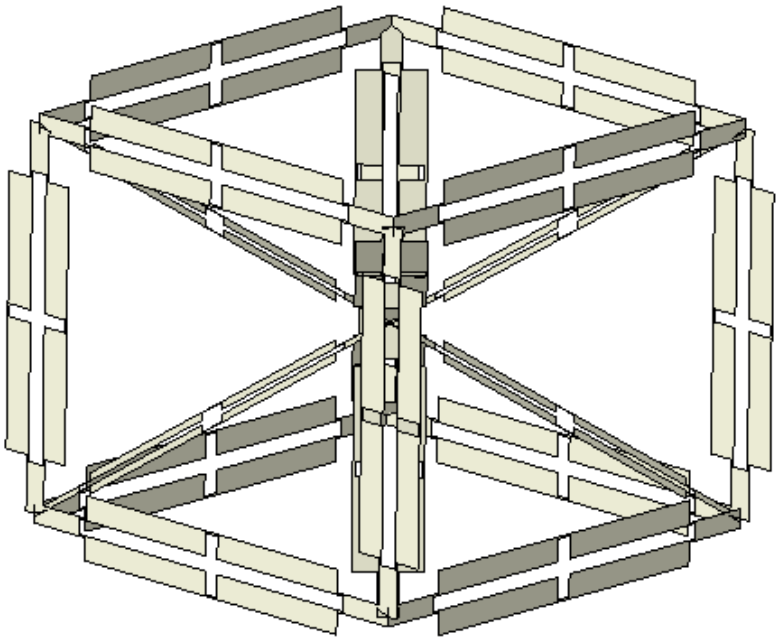


Figure 4.4. BCC lattice with distributed parameter inertial amplification mechanism.

First, modal analysis is performed since it requires less computational time. It is determined that band gap occurs in between 21^{st} and 22^{nd} modes. The analysis is repeated using various element types and mesh size to determine the most appropriate mesh size for the frequency response analysis which requires more computational time.

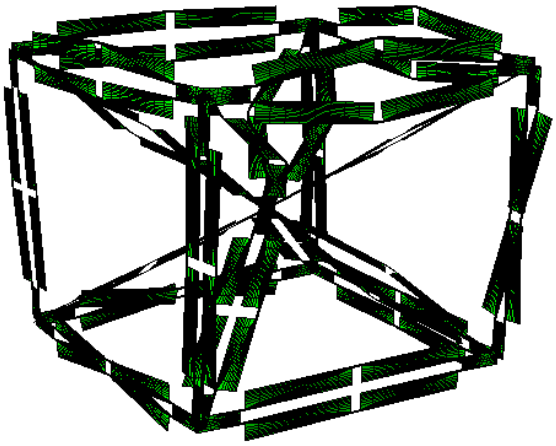
Table 4.1. Mesh convergence study for the finite element model.

Element Type	**Mesh Size**	ω_{21}/ω_{22}	**CPU Time**	**# of Elements**
Linear	0.2 mm	294/636	48 minute	601 000
Linear	0.3 mm	294/640	6 minute	262 000
Linear	0.4 mm	300/642	2.5 minute	93 000
Linear	8 elements per edge	304/674	1.3 minute	33 000
Quadratic	8 elements per edge	296/642	2.3 minute	33 000

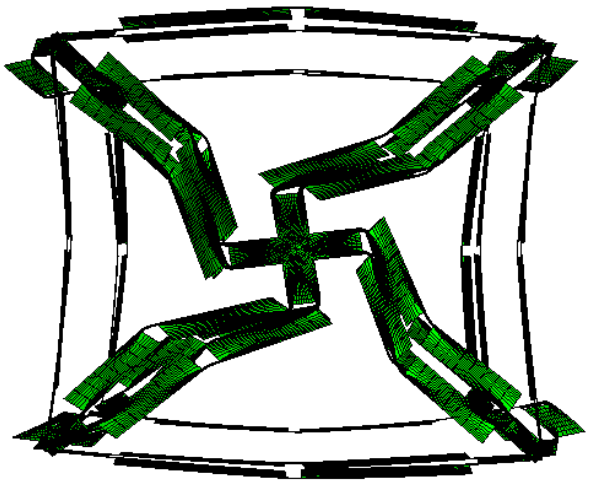
Table 4.1 shows the mesh convergence study for the finite element model of the BCC lattice. It is determined that using different mesh size for each edge instead of using fixed size elements on the entire model requires less CPU time for converged result. To that end, 8 elements are used on each edge. It is also found that using quadratic shell elements (S8R) instead of linear ones gives better results with reasonable increase in CPU time.

21^{st}, 22^{nd} and 26^{th} mode shapes of the BCC lattice can be seen in Figure 4.5a-c. Notice that, in 21^{st} mod shape, each element deforms as in the mode shape seen in Figure 4.2a, in 22^{nd} mod shape, each element deforms as in the mode shape seen in Figure 4.2b and in 26^{th} mod shape, each element deforms as in the mode shape seen in Figure 4.2d.

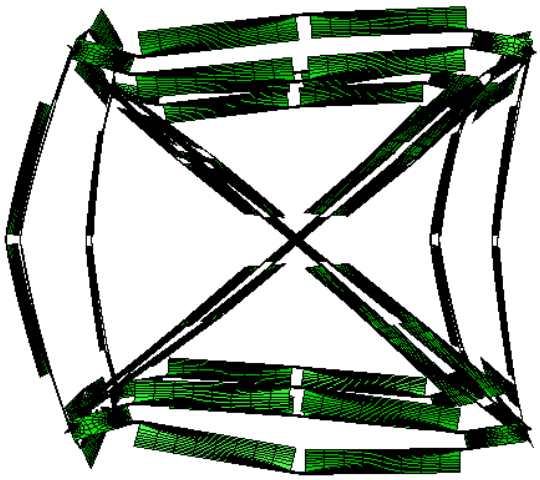
Then, frequency response analysis is performed in order to see stop band of the BCC lattice which is given in Figure 4.6. It is seen that the band gap occurs in between the frequency range 296-642 Hz. This band gap is very close to the band gap of each building block mechanisms. Notice that, if band gaps of building block mechanisms in Figure 4.2 and 4.3 are widened, the band gap of three-dimensional structure built with them will also be wide. However, since the BCC lattice requires optimization of the band structure of the two different mechanism, it is beneficial to use a structure which can be built using identical building blocks which can be octahedron structure. Following section will focus on the octahedron structure.



(a) $\omega_{21} = 296$ Hz



(b) $\omega_{22} = 642$ Hz



(c) $\omega_{26} = 754$ Hz

Figure 4.5. (a) 21^{st}, (b) 22^{nd} and (c) 26^{th} mode shapes of the BCC structure.

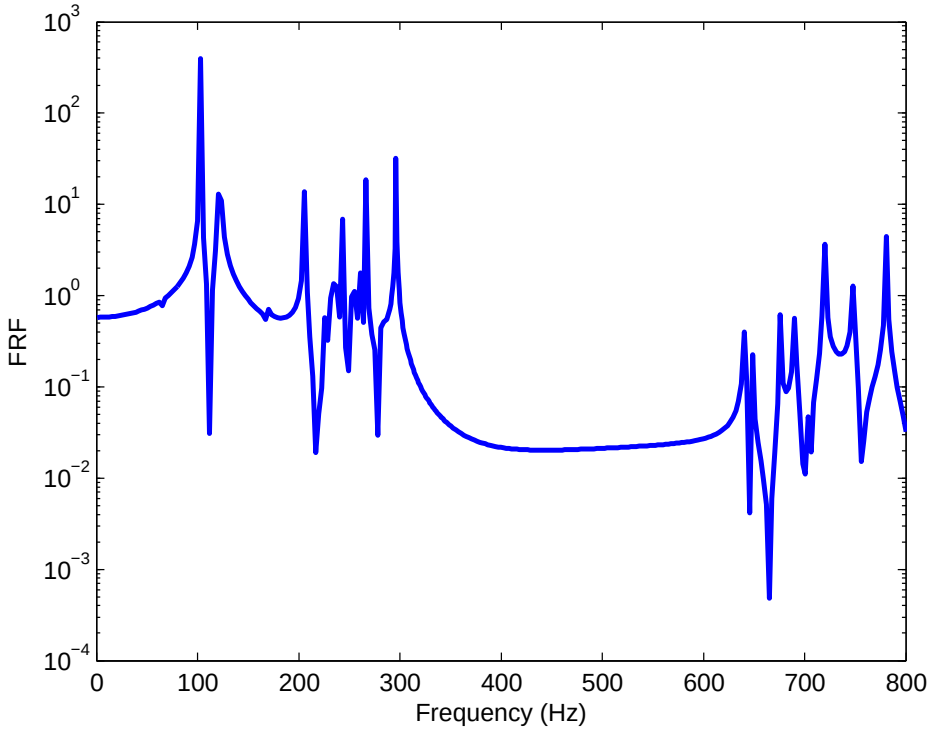


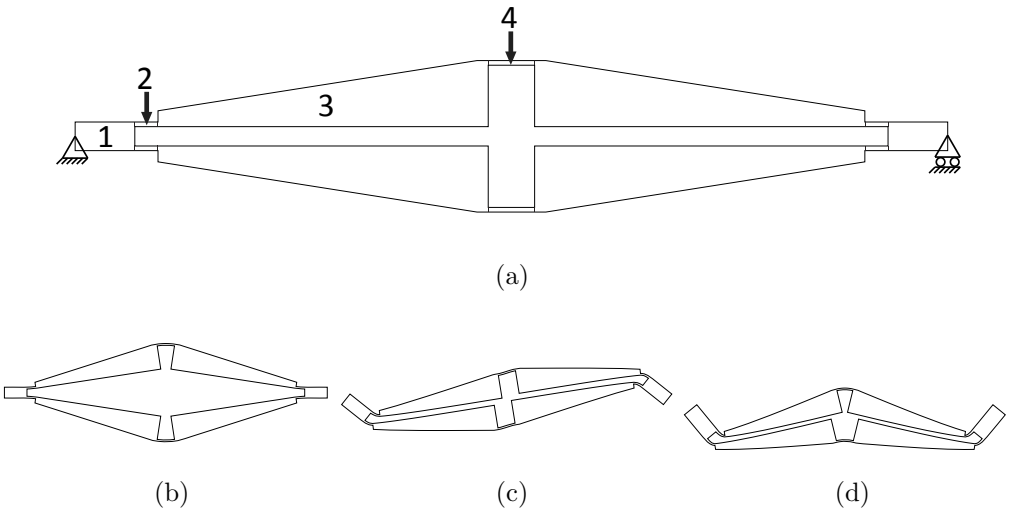
Figure 4.6. Frequency response plot of the distributed parameter BCC structure.

4.2. Octahedron Structure

In this section, first, a building block for the octahedron structure will be designed. Then, an octahedron structure and an array of octahedron structures will be formed using the building block mechanism and their frequency responses will be obtained.

The inertial amplification mechanism shown in Figure 4.7a will be the building block of octahedron structure. Here, thicknesses of the second and fourth segments are small, hence they act like flexure hinges.

In [46], it was shown that a vibration stop band is formed between the first two natural frequencies of an inertial amplification mechanism. Moreover, the first antiresonance frequency of the mechanism determines the stop band depth. Therefore, these natural frequencies need to be calculated for the inertial amplification mechanism shown in Figure 4.7a. Figures 4.7b-d show the first three vibration modes of the inertial



(a)

(b) (c) (d)

Figure 4.7. (a) The inertial amplification mechanism, and its (b) first, (c) second and (d) third vibration modes.

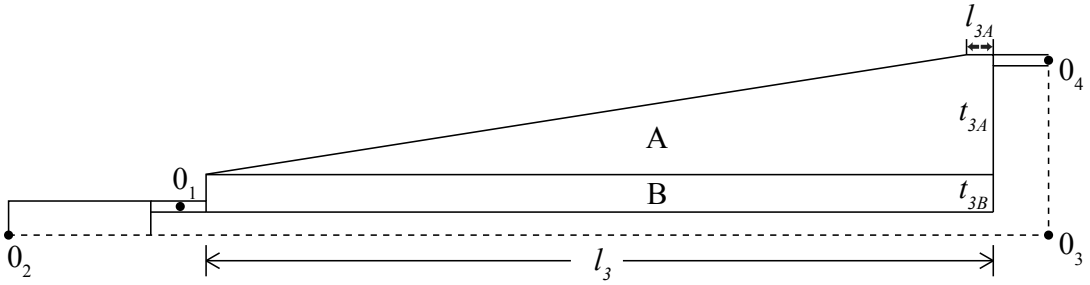
amplification mechanism. In [46], a similar mechanism was used to form a 2D phononic band gap structure. However, in this study, the third segment shown in Figure 4.7a has trapezoidal shape whereas it was in rectangular shape in [46]. Therefore, kinetic energies of the vibration modes will be different than those in [46]. Nevertheless, potential energy calculations are based on the properties of the thin beam sections (second and fourth) and the calculations in [46] can be used.

4.2.1. Analytical Model of the Building Block Mechanism

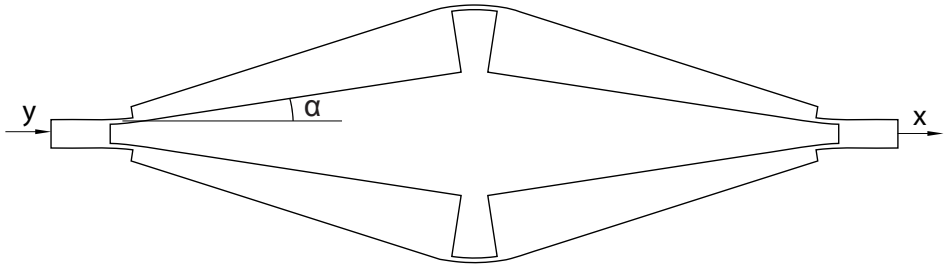
In the first mode, trapezoid's center of mass will translate more compared to that of a rectangle, which increases the kinetic energy in this mode, that in turn reduces its natural frequency. On the other hand, in the second and third modes, trapezoid's center of mass will translate less compared to that of a rectangle, which decreases the kinetic energy in these modes, that in turn increases their natural frequencies. As the first stop band will be formed between the first two natural frequencies of the mechanism [46], trapezoidal shaped third segments will enable a wider stop band.

Inertia of the third beam segment need to be determined for kinetic energy calculations. In Figure 4.7, l_i and t_i are length and thickness of the ith beam for $i = 1, 2, 4$ and Figure 4.8 shows the dimensions regarding the third beam segment. For the ana-

lytical calculations, l_{3A} in Figure 4.8 is taken as zero, which gives that the third beam is in trapezoidal shape.



(a)



(b)

Figure 4.8. (a) Quarter of the inertial amplification mechanism. (b) First mode of the mechanism. Here, α is the angle of the third beam segment, y is the input and x is the output displacement.

For the first mode seen in Figure 4.8b, the third beam rotates about the point O_1 in Figure 4.8a and its inertia (I_{O_1}) is:

$$I_{O_1} = I_{O_1A} + I_{O_1B} \tag{4.1}$$

where

$$I_{O_1A} = m_{3A}\left(\frac{t_{3A}^2 + l_3^2}{12} + \left(\frac{l_3 + l_2}{2}\right)^2 + \left(\frac{t_{3A} - t_2}{2}\right)^2\right), \tag{4.2}$$

$$I_{O_1B} = m_{3B}\left(\frac{t_{3B}^2 + l_3^2}{18} + \left(\frac{2l_3}{3} + \frac{l_2}{2}\right)^2 + \left(\frac{t_{3B}}{3} + t_{3A} - \frac{t_2}{2}\right)^2\right) \tag{4.3}$$

and m_{3A} and m_{3B} are the masses of the sections denoted by A and B in Figure 4.8.

Now, assuming small oscillations, total rotational kinetic energy of the third beam segments (four of them) can be obtained as in [46].

$$T_r = 4 \times \frac{1}{2} I_{O_1} \dot{\alpha}^2 = 2 I_{O_1} \dot{\alpha}^2 \tag{4.4}$$

where

$$\alpha = \frac{x - y}{2t_3 - t_2 - t_4}. \tag{4.5}$$

Total translational kinetic energy of the first beam segments (two of them) and third beam segments (four of them) can be written as:

$$T_t = \frac{1}{2} m_1 \dot{x}^2 + \frac{1}{2} m_1 \dot{y}^2 + 4 \times \frac{1}{2} m_3 \left(\frac{\dot{x} + \dot{y}}{2} \right)^2. \tag{4.6}$$

Total kinetic energy can be obtain by adding Equations 4.4 and 4.6 as follows:

$$T = 2 I_{O_1} \frac{(\dot{x} - \dot{y})^2}{(2t_3 - t_2 - t_4)^2} + \frac{1}{2} m_1 (\dot{x}^2 + \dot{y}^2) + \frac{1}{2} m_3 (\dot{x} + \dot{y})^2. \tag{4.7}$$

Total potential energy of the inertial amplification mechanism is the sum of the strain energies of the bending flexure hinges (second and fourth beam segments). The four flexure hinges with thickness t_2 and the two flexure hinges with thickness t_4 are assumed to bend into circular arcs subtending angles α and 2α, respectively. Thus, the total potential energy of these flexure hinges can be obtained as

$$V = \frac{2EI_2}{l_2} \alpha^2 + \frac{4EI_4}{l_4} \alpha^2. \tag{4.8}$$

Using Equation 4.5 in Equation 4.8, the total potential energy can be obtained as:

$$V = \frac{2EI_2(x-y)^2}{l_2(2t_3 - t_2 - t_4)^2} + \frac{4EI_4(x-y)^2}{l_4(2t_3 - t_2 - t_4)^2}. \tag{4.9}$$

It is also known that potential energy of a system with equivalent stiffness (k) under displacement ($x - y$) is:

$$V = \frac{1}{2}k(x-y)^2. \tag{4.10}$$

Then, k can be obtained by equating Equations 4.9 and 4.10 as

$$k = \frac{4EI_2}{l_2(2t_3 - t_2 - t_4)^2} + \frac{8EI_4}{l_4(2t_3 - t_2 - t_4)^2}. \tag{4.11}$$

Equation of motion is obtained by Lagrange method using $L = T - V$ as follows:

$$\frac{d}{dt}\left(\frac{\partial L}{\partial \dot{x}}\right) - \frac{\partial L}{\partial x} = 0 \tag{4.12}$$

$$\left(\frac{4I_{O_1}}{(2t_3 - t_2 - t_4)^2} + m_1 + m_3\right)\ddot{x} + kx = \left(\frac{4I_{O_1}}{(2t_3 - t_2 - t_4)^2} - m_3\right)\ddot{y} + ky \tag{4.13}$$

The effective mass of the mechanism (m_e) is the term that multiplies the $\ddot{x}$ term, i.e.,

$$m_e = \frac{4I_{O_1}}{(2t_3 - t_2 - t_4)^2} + m_1 + m_3. \tag{4.14}$$

Moreover, overall mass of the mechanism is given in Equation 4.15. Here, mass

of the flexure hinges (second and fourth beam segments) are neglected.

$$m = 2m_1 + 4m_3 \tag{4.15}$$

Using Equations 4.14 and 4.15, the equation of motion given in Equation 4.13 can be simplified as:

$$m_e\ddot{x} + kx = \left(m_e - \frac{m}{2}\right)\ddot{y} + ky \tag{4.16}$$

Finally, the first resonance (ω_{p1}) and antiresonance (ω_{z1}) frequencies of the mechanism are obtained as follows:

$$\omega_{p1} = \sqrt{\frac{k}{m_e}} \tag{4.17}$$

$$\omega_{z1} = \sqrt{\frac{k}{m_e - \frac{m}{2}}} \tag{4.18}$$

The second resonance frequency of the inertial amplification mechanism in the current work can be calculated by modifying the second resonance frequency formulation given in [46], i.e.,

$$\omega_{p2} = \sqrt{\frac{\frac{2EI_2}{l_2}(1+r)^2}{I_{O_2} + 2r^2 I_{O_3}}} \tag{4.19}$$

where

$$r = \frac{l_1 + \frac{l_2}{2}}{l_3 + \frac{l_2 + l_4}{2}}. \tag{4.20}$$

In Equation 4.19, I_{O_2} is inertia of the first beam segments about the point O_2 and I_{O_3} is inertia of the third beam segments about the point O_3 (see Figure 4.8a). As in [46], I_{O_2} can be calculated as

$$I_{O_2} = \frac{m_1 l_1^2}{3}. \tag{4.21}$$

In the current work, I_{O_3} is different than the one in [46] as the third beam segments have trapezoidal shape and therefore, I_{O_3} can be calculated as

$$I_{O_3} = I_{O_3A} + I_{O_3B} \tag{4.22}$$

where

$$I_{O_3A} = m_{3A}\left(\frac{t_{3A}^2 + l_3^2}{12} + \left(\frac{l_3 + l_2}{2}\right)^2 + \left(\frac{t_{3A} + t_1}{2} - t_2\right)^2\right) \tag{4.23}$$

and

$$I_{O_3B} = m_{3B}\left(\frac{t_{3B}^2 + l_3^2}{18} + \left(\frac{l_3}{3} + \frac{l_4}{2}\right)^2 + \left(\frac{t_{3B}}{3} + t_{3A} + \frac{t_1}{2} - t_2\right)^2\right). \tag{4.24}$$

4.2.2. Computational Model of the Building Block Mechanism

A finite element model (FEM) of the inertial amplification mechanism as seen in Figure 4.9 is created to verify the analytical model. 3D finite elements need to be utilized since 3D structures will be created using the inertial amplification mechanisms.

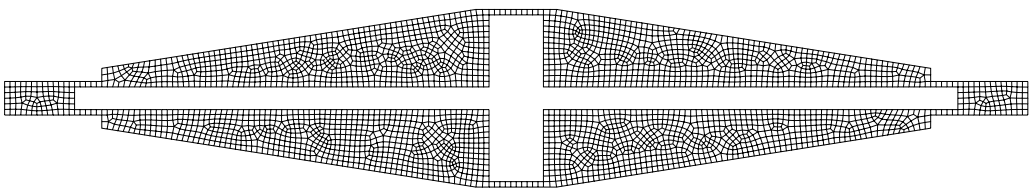


Figure 4.9. Finite element model of the inertial amplification mechanism.

In the modal analysis of the mechanism, 3D 8 node quadratic shell elements (S8R) are used instead of 3D solid elements, considering computational efficiency.

4.2.3. Optimization of the Building Block Mechanism

The inertial amplification mechanism is optimized to obtain a wide stop band. Figure 4.10a shows the rigid link mechanism equivalent of half of the inertial amplification mechanism with flexible links (see Figure 4.7a). Notice that left halves of the second and third modes of the inertial amplification mechanism (see Figure 4.10b-c) are quite similar. It is determined that these modes will occur in the same frequency if l_1 is chosen such that O_2 in Figure 4.10a is the instant center of rotation for link 1 and the ground link, which is ensured by Equation 4.30.

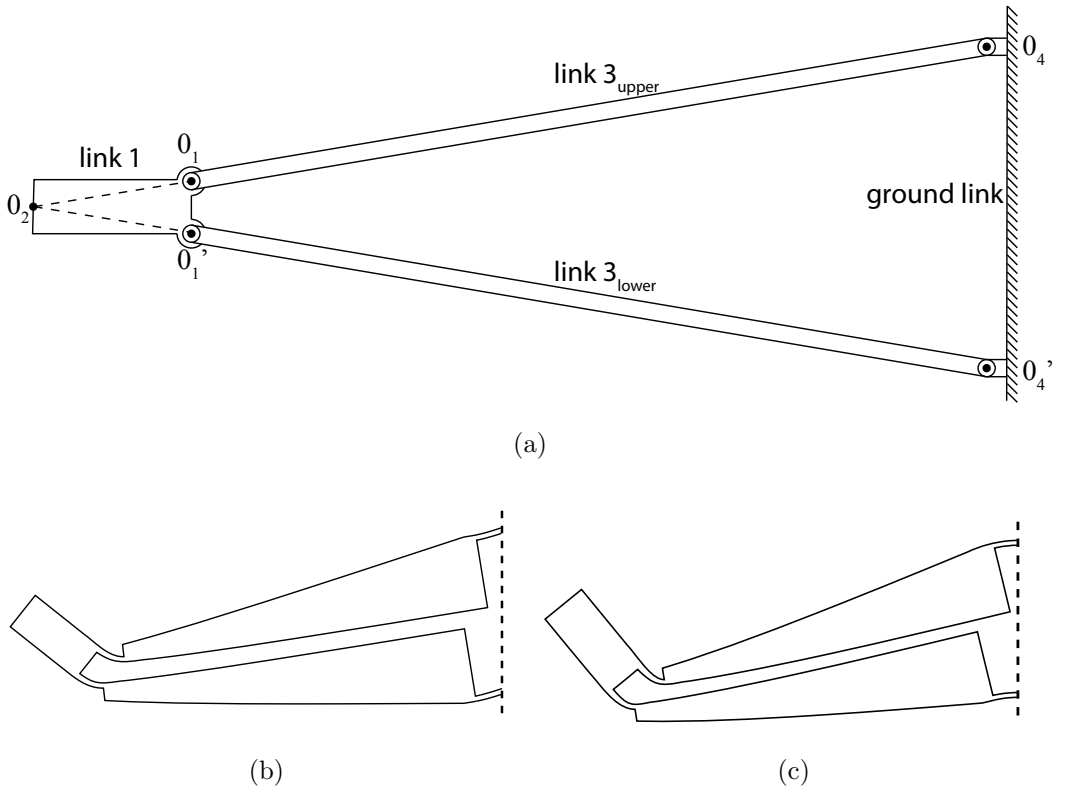


Figure 4.10. (a) Rigid link mechanism equivalent of half of the inertial amplification mechanism showing O_2 as the instant center of rotation for link 1 and the ground link. (b) Half of the mechanism in the second mode and (c) in the third mode.

3D structures with embedded inertial amplification mechanisms will be manufactured using a 3D printer for molten polymer deposition. ρ and E are the density and

elastic modulus of the polymer material that is used in 3D printing. The first stop band occurs in between the first and second resonance frequencies. When Equations 4.17 and 4.19 are solved for different t_i values, it is found that t_1, t_2 and t_4 should attain small values in order to widen the stop band. When the building block mechanisms are assembled in 3D, they connect through beam 1 of each mechanism. To have a firm connection, t_1 is chosen as 3.7mm. Moreover, t_2 and t_4 are chosen as 0.6mm by considering manufacturing accuracy. Increasing the length of the flexure hinges (l_2 and l_4), lowers the stop band frequency range, but it also reduces the overall stiffness of the structure (see Equation 4.11). Besides, if the aspect ratio (l_2/t_2 or l_4/t_4) in these beams are large, local buckling problems may occur. Furthermore, Equations 4.17 and 4.19 show that a large l_2/t_2 ratio results in a smaller w_{p2}/w_{p1} ratio. In order to prevent local buckling problems and have large stop band width, $l_2 = 5t_2$ is used as a constraint. $l_4 = 2l_2$ is also taken as a constraint. In Figure 4.8b, each flexure hinge with thicknesses t_2 and t_4 are assumed to bend into circular arcs subtending angles α and 2α, respectively. Thus, this constraint ensures that these flexure hinges have the same stress level in the first vibration mode.

After all these stated constraints, t_{3A} and t_{3B} are the only free variables. Finally, the optimization problem can be defined as follows:

min ω_{p1}/ω_{p2}
Free variables: t_{3A}, t_{3B}
Fixed variables: $t_1 = 3.7$ mm, $t_2 = t_4 = 0.6$ mm
Material properties: $\rho = 1170$ kg/m^3, $E = 2.495$ GPa
Constraints:

$$t_3 = t_{3A} + t_{3B} \tag{4.25}$$

$$l_2 = 5t_2 \tag{4.26}$$

$$l_3 = 5t_3 \tag{4.27}$$

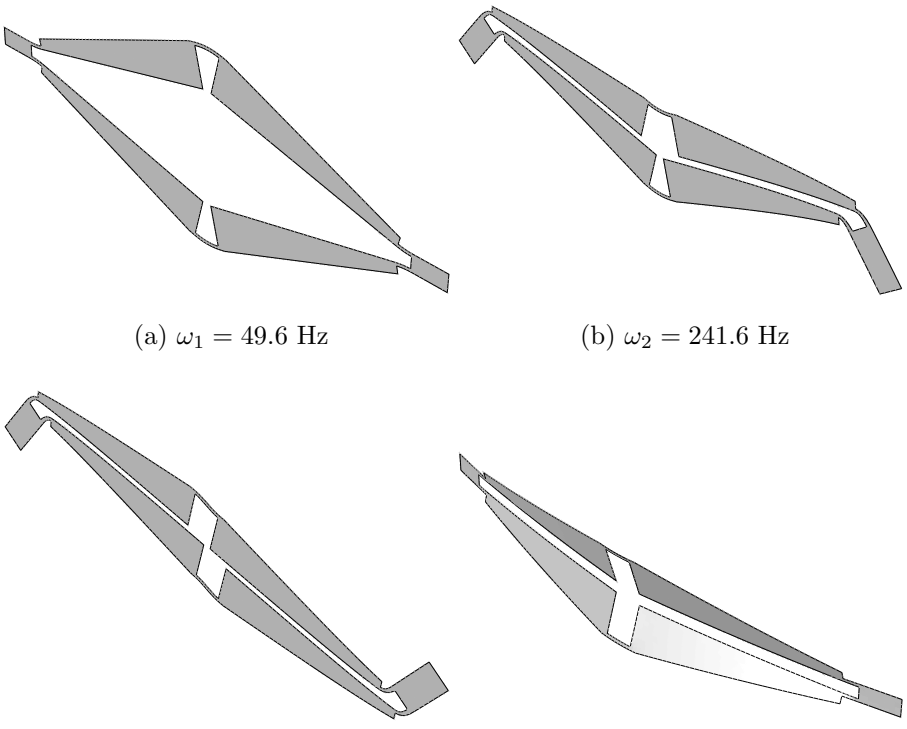
$$l_{3A} = t_{3B} - t_2 \tag{4.28}$$

$$l_4 = 2l_2 \tag{4.29}$$

$$l_1 = \frac{(\frac{l_2}{2} + l_3 + l_4)}{(t_3 - \frac{t_2}{2} - \frac{t_4}{2})}(\frac{t_1}{2} - t_2 + t_3 - \frac{t_4}{2}) - l_2 - l_3 - l_4 \tag{4.30}$$

The optimization problem is solved by using Newton's method and genetic algorithm. Both methods converged to the following results: $t_{3A} = 2.05$ mm, $t_{3B} = 6.49$ mm.

In order to have a wide stop band in the 3D structure, the out-of-plane mode of the mechanism is placed a little bit higher than the natural frequencies of the second and third modes by selecting the out-of-plane thickness (b) as 9 mm. The first four mode shapes of the optimized mechanism are seen in Figure 4.11. Notice that the instant center principle enabled that the second and third modes occur in very close frequencies.



(a) $\omega_1 = 49.6$ Hz (b) $\omega_2 = 241.6$ Hz

(c) $\omega_3 = 248.2$ Hz (d) $\omega_4 = 259.5$ Hz

Figure 4.11. First four mode shapes of the optimized inertial amplification mechanism.

Analytical and numerical resonance and antiresonance frequency results are given in Table 4.2. Here, the analytical results are obtained using Equations 4.17, 4.18 and 4.19. In Table 4.2 the frequency results are quite close. In line with [46], a stop band will form between ω_{p1} and ω_{p2}. Notice that the use of trapezoidal shaped third beam segment enabled a very wide stop band with $\omega_{p2}/\omega_{p1} = 4.87$ for the finite element model and the corresponding gap/midgap ratio is 1.31. This is a very wide stop band considering that gap/midgap ratios are lower than 1 in many studies ([24,28,32,34,46]).

Table 4.2. Comparison of analytical and numerical resonance and antiresonance frequency results.

	Analytical (Hz)	**FEM (Hz)**
$\boldsymbol{\omega_{p1}}$	54.8	49.6
$\boldsymbol{\omega_{z1}}$	59.1	53.2
$\boldsymbol{\omega_{p2}}$	242.0	241.6

It is expected that the stop band of the inertial amplification mechanism will occur in between 49.6 Hz and 241.6 Hz. In Figure 4.12a, frequency response function (FRF) plots of arrays of inertial amplification mechanisms are depicted. Here, FRF is defined as output to input acceleration ratio. It is seen that the stop band frequency range do not change as the number of unit cells in the 1D array increases, but only stop band depth increases.

The highest FRF value within the stop band for one unit cell can be estimated by $\omega_{p1}^2/\omega_{z1}^2$ [46]. By using Equations 4.17 and 4.18, the highest FRF value within the stop band can be calculated as 0.86. In Figure 4.12a, it is 0.87 for $n_{units} = 1$ which is consistent with the analytical result.

In order to obtain band structure of the infinitely periodic inertial amplification mechanism, mass (**M**) and stiffness (**K**) matrices of the inertial amplification mechanism are generated using the finite element model. Equation of motion of the inertial

amplification mechanism is

$$\omega^2 \mathbf{M}\boldsymbol{u} = \mathbf{K}\boldsymbol{u}, \tag{4.31}$$

where ω is the frequency and $\boldsymbol{u}$ is the displacement vector. For an infinitely periodic array, left nodes are related to right nodes by

$$u_L^j = u_R^j e^{-i\gamma a}, \tag{4.32}$$

where where u_L^j is the displacement of the j^{th} left node, u_R^j is the displacement of the j^{th} right node, a is the length of the mechanism and γ is the wave number.

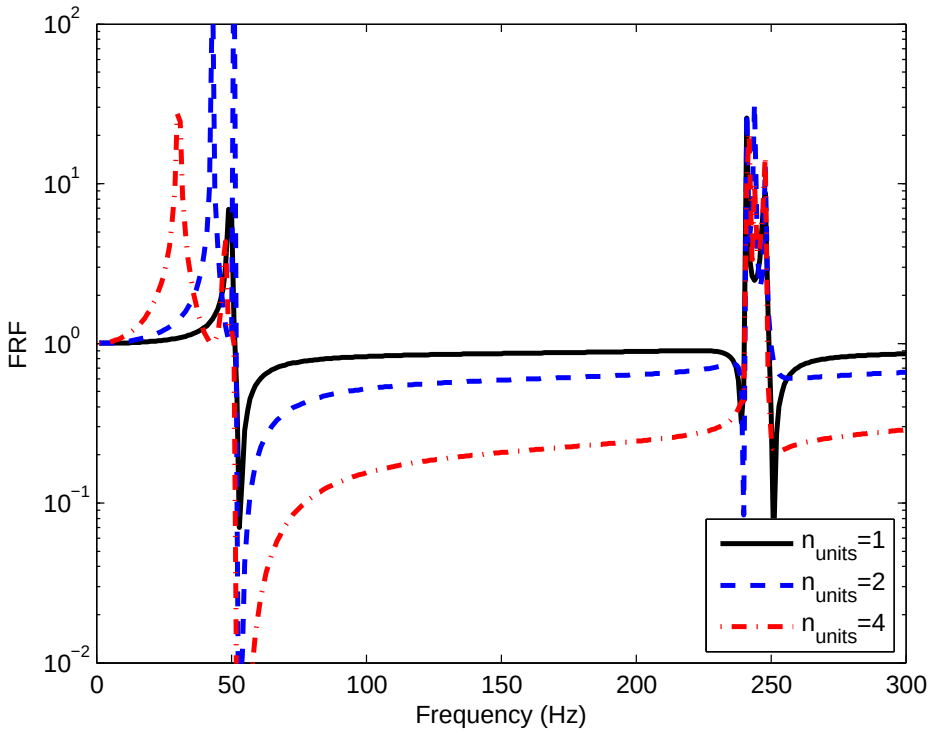
After substituting Equation 4.32 into Equation 4.31, mass ($\tilde{\mathbf{M}}$) and stiffness ($\tilde{\mathbf{K}}$) matrices of the infinitely periodic inertial amplification mechanism are obtained. Band structure of the infinitely periodic inertial amplification mechanism is obtained by solving the eigenvalue problem (see Equation 4.33) for γ from 0 to π/a.

$$\det\left(\tilde{\mathbf{K}}(\gamma) - \omega^2\tilde{\mathbf{M}}\right) = 0 \tag{4.33}$$

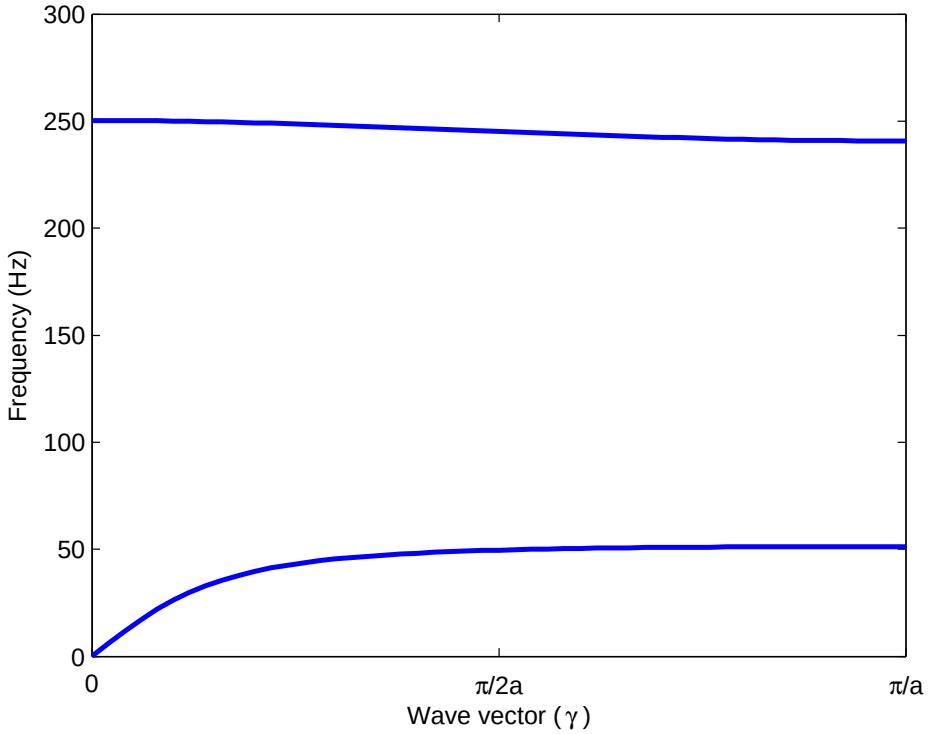
Band structure of the infinitely periodic inertial amplification mechanism is given in Figure 4.12b, which shows that the first band gap is formed in the frequency range 51.3-240.7 Hz, which agree with the stop band frequency range of the finite 1D arrays.

4.2.4. Modification of the Building Block Mechanism for 3D Assembly

An octahedron structure is built using the optimized inertial amplification mechanisms as seen in Figure 4.13. Modal analysis of the octahedron structure is performed using FEM. Natural frequencies of the octahedron structure in the vicinity of the stop band frequency range of the building block mechanism (49.6-241.6 Hz) are listed in Table 4.3. One can see that additional modes (8th-12th) occur within the stop band.



(a)



(b)

Figure 4.12. (a) Frequency response of the finite periodic inertial amplification mechanism with various number of unit cells. (b) Band structure of the infinitely periodic inertial amplification mechanism. Here, a represents the length of the mechanism.

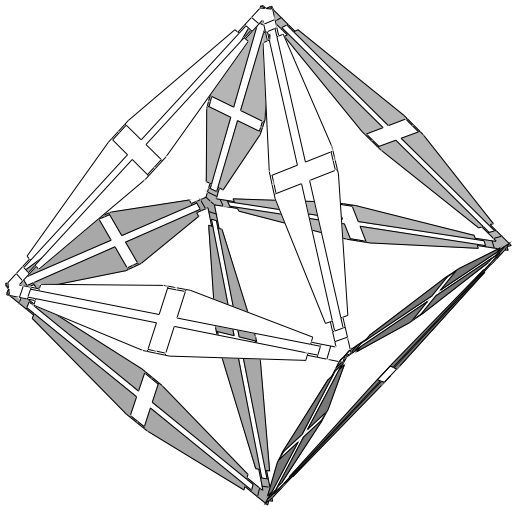


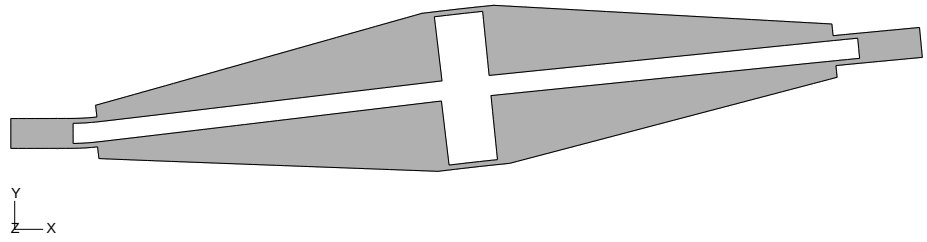
Figure 4.13. The octahedron structure formed using the uniform thickness optimized inertial amplification mechanisms.

Table 4.3. Natural frequencies of the octahedron structure.

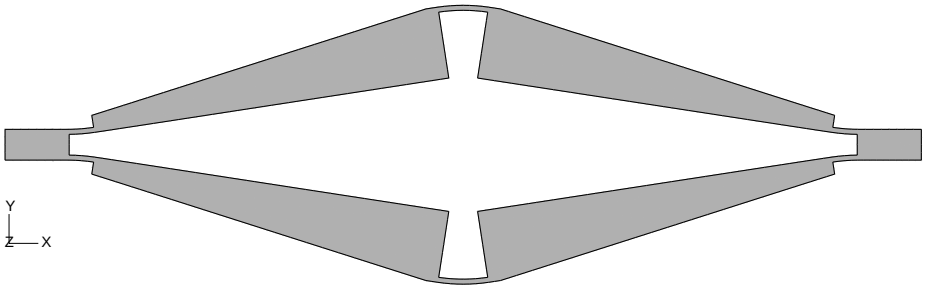
Mode Number	**Frequency (Hz)**
7	49.6
8-10	56.6
11,12	64.0
13	267.2

In [46], when inertial amplification mechanisms are used to form a 2D periodic structure, the pinned-roller boundary conditions (BCs) ensured that the building block mechanism and the 2D periodic structure have the same stop band frequency range. However, this is not the case for a 3D periodic structure as the building block mechanisms can also bend in the out-of-plane direction when the structure is excited within the stop band. Hence, unlike 1D or 2D assembly of the building block mechanisms, the first vibration stop band in a 3D assembly not necessarily span the interval between the first two resonance frequencies of the building block mechanism. For the building block mechanism, if the resistance to out-of-plane bending for fixed-free BCs can be reduced, it is expected that the additional modes within the stop band of the 3D assembly will disappear.

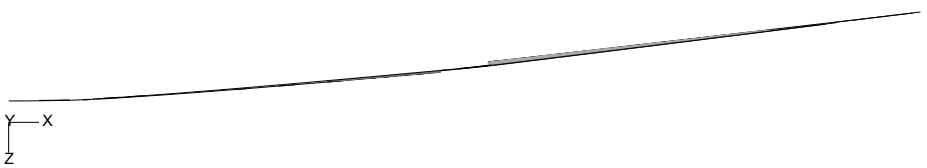
Figure 4.14 shows the first three modes of the inertial amplification mechanism. Notice that the third mode is an out-of-plane mode and it resides in the stop band frequency range. To eliminate the additional modes within the stop band of the octahedron structure, this out-of-plane mode of the building block mechanism should be placed at a lower frequency. This can be achieved by lowering the out-of-plane thickness of the ends. However, lowering this frequency also lowers the upper limit of the stop band of the octahedron structure. In order not to lower the upper limit significantly while eliminating the additional modes within the stop band, this out-of-plane mode is placed at 25 Hz by reducing the out-of-plane thickness of the ends from 9mm to 1.8mm (see Figure 4.15b). Natural frequencies of the modified mechanism are listed in Tables 4.4 and 4.5.



(a) $\omega_1 = 14.2$ Hz

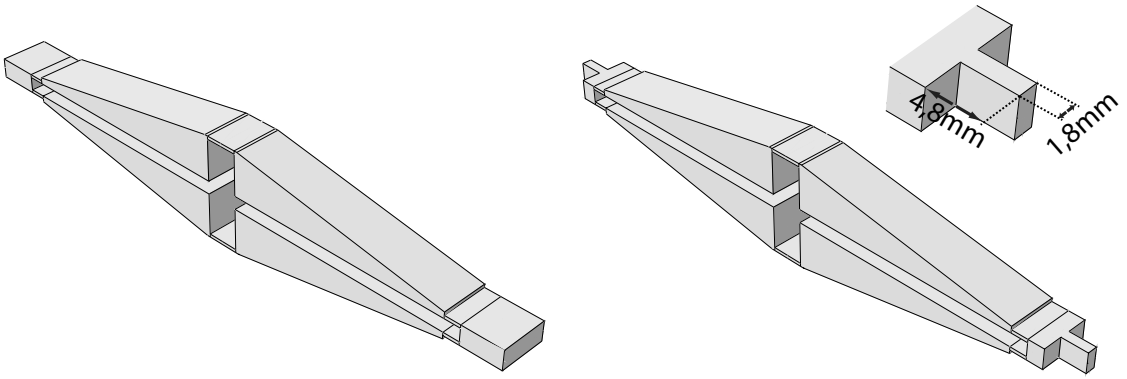


(b) $\omega_2 = 49.6$ Hz



(c) Out-of-plane mode, $\omega_3 = 110.2$ Hz

Figure 4.14. First three mode shapes of the optimized mechanism with fixed-free BCs.



(a) (b)

Figure 4.15. (a) The optimized mechanism that can only be used for 1D or 2D assembly. (b) The optimized mechanism with its two ends modified for 3D assembly.

Table 4.4. Natural frequencies of the modified mechanism with pinned-roller boundary conditions.

	Frequency (Hz)
$\boldsymbol{\omega_1}$	49.6
$\boldsymbol{\omega_2}$	240.7
$\boldsymbol{\omega_3}$	246.0
$\boldsymbol{\omega_4}$	249.9

Table 4.5. Natural frequencies of the modified mechanism with fixed-free boundary conditions.

	Frequency (Hz)
$\boldsymbol{\omega_1}$	14.2
$\boldsymbol{\omega_2}$	25.7
$\boldsymbol{\omega_3}$	49.6
$\boldsymbol{\omega_4}$	214.6

4.2.5. Octahedron Structure

Another octahedron structure is assembled using the modified inertial amplification mechanisms as seen in Figure 4.16a. In this structure, no vibration mode occurs

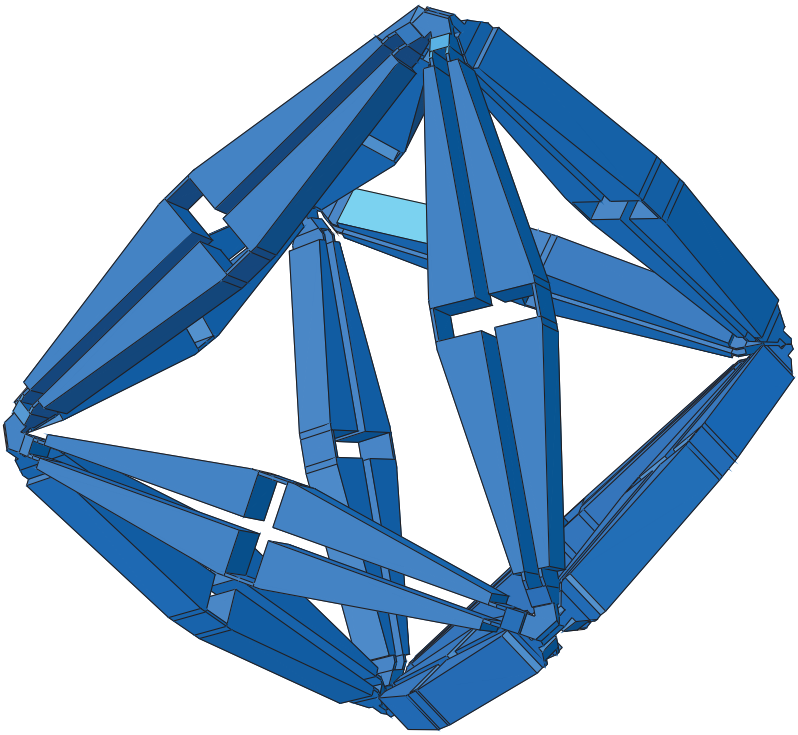
within the stop band frequency range of the building block mechanism. The first stop band of this structure will occur between 12th (50.4 Hz) and 13th (233.0 Hz) modes.

Frequency response of the octahedron structure is seen in Figure 4.16b. Stop band occurs in the same frequency range with the stop band of the modified inertial amplification mechanism.

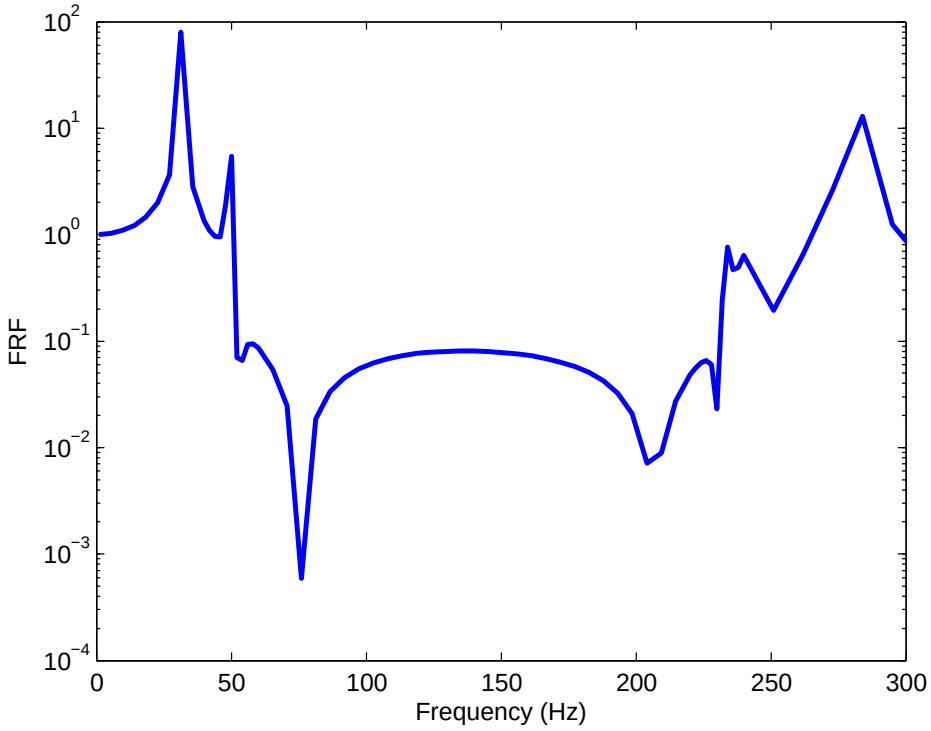
4.2.6. 2×3 Array of Octahedron Structures

A 2×3 array of octahedron structures is built using the modified inertial amplification mechanisms as seen in Figure 4.17a. The first stop band of this 3D structure will occur between 66th (51.90 Hz) and 67th (218.03 Hz) modes.

Frequency response of the 2×3 array of octahedron structures is seen in Figure 4.17b. Stop band occurs in the same frequency range with the octahedron structure. Notice that very wide and deep band gap occurs using moderate number unit cells.

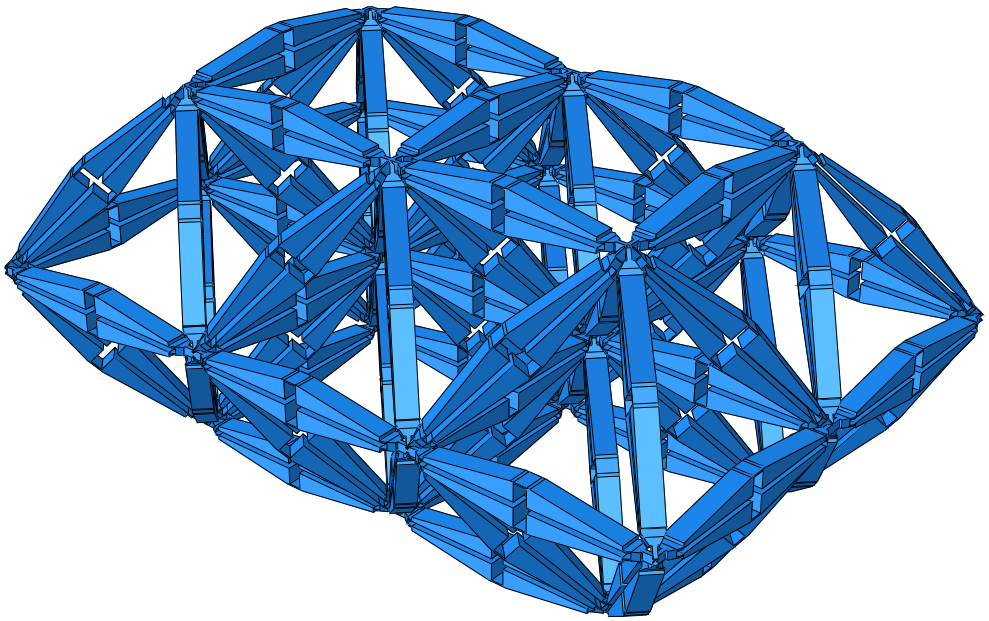


(a)

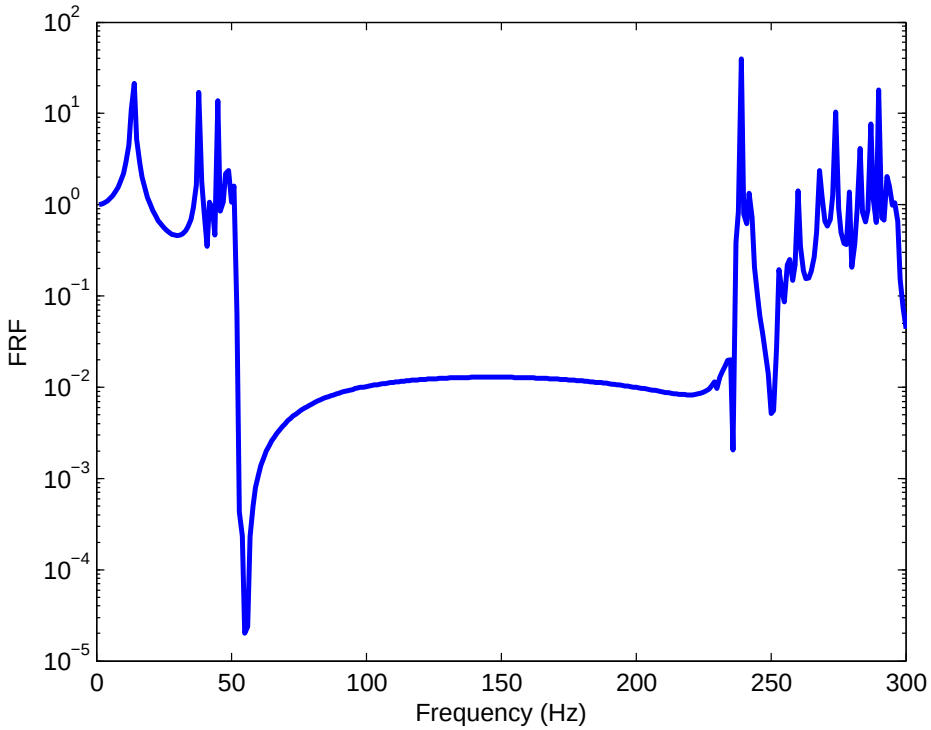


(b)

Figure 4.16. (a) The octahedron structure formed using the optimized inertial amplification mechanisms with modified ends. (b) Frequency response of the octahedron structure.



(a)

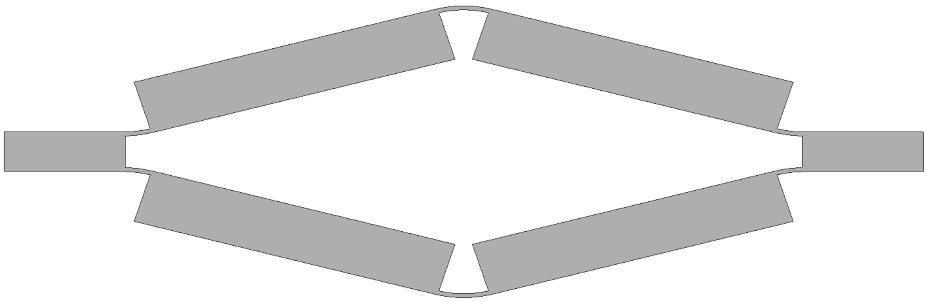


(b)

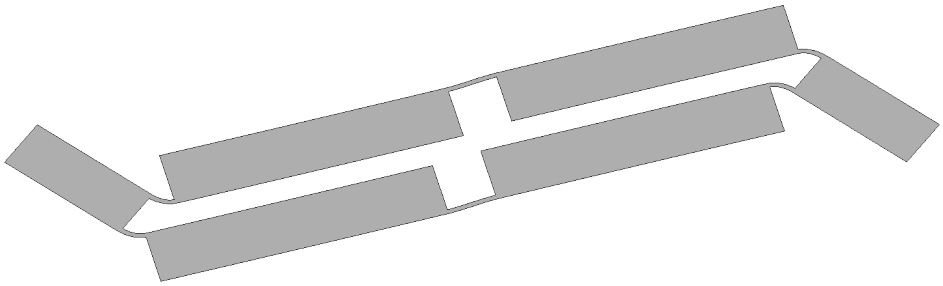
Figure 4.17. (a) 2×3 array of octahedron structures. (b) Frequency response of the 2×3 array of octahedron structures.

5. DESIGN AND ANALYSIS OF THE INERTIAL AMPLIFICATION MECHANISMS WITH ULTRA WIDE BAND GAP

In this chapter, a new inertial amplification mechanism is designed in order to obtain the widest possible band gap. In the design process, first two mode shapes of the inertial amplification mechanism seen in Figure 5.1 are investigated. Since the band gap occurs in between the first and second resonance frequencies, it is possible to obtain larger band gaps by changing the frequencies of these modes.



(a) $\omega_1 = 267$ Hz



(b) $\omega_2 = 600$ Hz

Figure 5.1. First and second mode shapes of the inertial amplification mechanism.

Notice that, in the second mode, the upper and lower thick beams can easily slide relative to each other as seen in Figure 5.1b. If this sliding mode is prevented, it will be possible to obtain a larger band gap. In order to ground this theory, rigid link equivalent of the inertial amplification mechanism is also given in Figure 5.2.

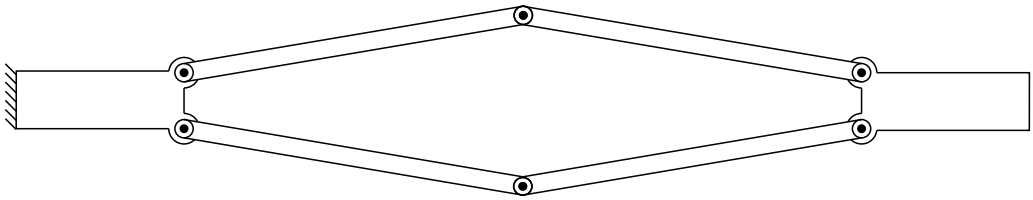


Figure 5.2. Rigid link equivalent of the inertial amplification mechanism. Here, $DOF = 3$.

Degree of freedom (DOF) of a rigid link mechanism can be calculated using Gruebler's equation:

$$DOF = 3(n-1) - 2j_1 - j_2 \tag{5.1}$$

where n is number of links and j_i is the number of joints with i degree of freedom.

Using Equation 5.1, DOF of the rigid link mechanism seen in Figure 5.2 is calculated as 3 (where $n = 6$, $j_1 = 6$ and $j_2 = 0$). In order to decrease the degree of freedom and let the mechanism only move as in the first mode seen in Figure 5.1a, a new rigid link mechanism seen in Figure 5.3 is designed. Notice that DOF of this rigid link mechanism is 1 (where $n = 8$, $j_1 = 10$ and $j_2 = 0$).

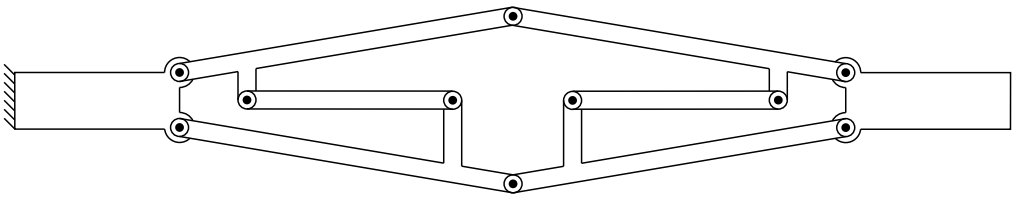


Figure 5.3. Rigid link equivalent of the modified inertial amplification mechanism. Here, $DOF = 1$.

In order to achieve an ultra wide band gap, the inertial amplification mechanism seen in Figure 5.4 is designed which acts like the rigid link mechanism seen in Figure 5.3. Notice that the mechanism seen in Figure 5.1 is modified by adding two slender beams that connect the upper and lower thick beams. In the absence of these slender

beams, the upper and lower thick beams can easily slide relative to each other as seen in Figure 5.1b. As the two slender beams constrain the sliding motion, it is expected that the inertial amplification mechanism shown in Figure 5.4 will have a second vibration mode at a much higher frequency. Moreover, it is also expected that the first vibration modes of the inertial amplification mechanisms with and without the constraining slender beams will occur at similar frequencies. In order to fulfill these requirements, the thicknesses of these slender beams are chosen as 0.2mm.

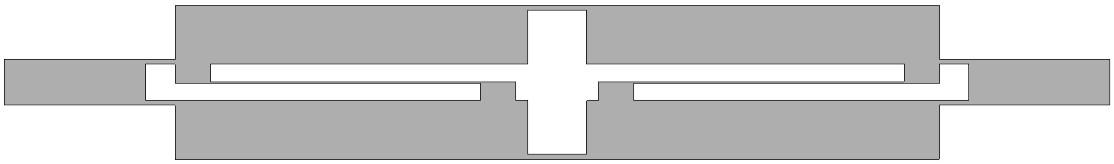
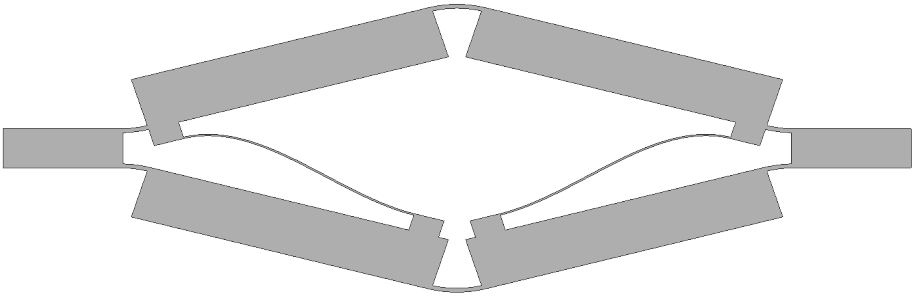
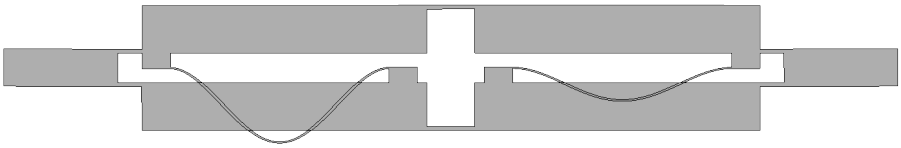


Figure 5.4. The inertial amplification mechanism with the constraining slender beams.

After modal analysis of the mechanism with the constraining slender beams, the first two mode shapes of this mechanism are obtained as seen in Figure 5.5.



(a) $\omega_1 = 240$ Hz



(b) $\omega_2 = 1193$ Hz

Figure 5.5. First and second mode shapes of the inertial amplification mechanism with the constraining slender beams.

It is seen that the sliding mode (see Figure 5.1b) of the upper and lower beams is prevented. Hence, ratio of the first and second natural frequencies of the inertial

amplification mechanism (ω_2/ω_1) is increased from 2.23 to 4.97 by simply adding the constraining beams. However, it is seen that the constraining slender beams are bending in the second mode (see Figure 5.5b). In order to increase the frequency of this mode shape, the middle part of the constraining beams are thickened to 1.64 mm as seen in Figure 5.6. Here, the two ends of the constraining beams are still 0.2 mm thick.

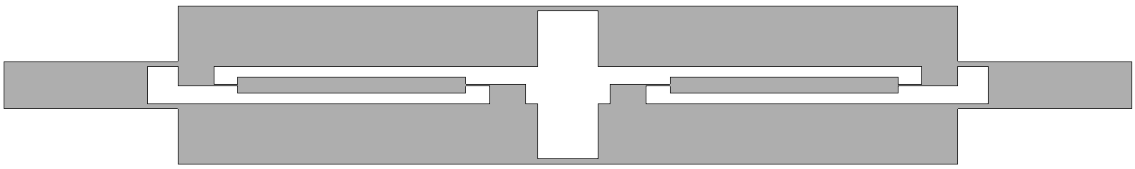
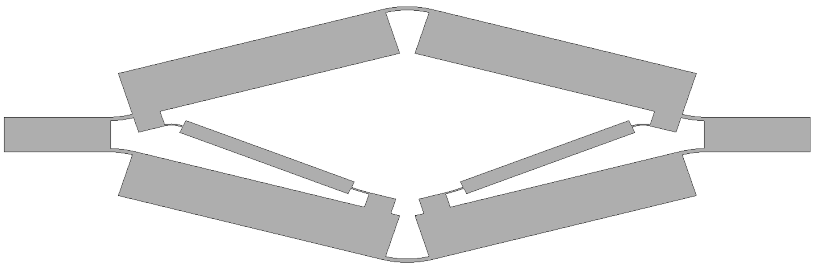
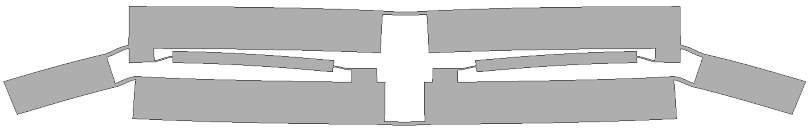


Figure 5.6. The inertial amplification mechanism with the constraining thick beams.

First two mode shapes of the mechanism with the constraining thick beams can be seen in Figure 5.7. It is seen that ω_2/ω_1 ratio is increased from 4.97 to 6.96 by using thick beam connections instead of slender beam connections.



(a) $\omega_1 = 241$ Hz



(b) $\omega_2 = 1681$ Hz

Figure 5.7. First and second mode shapes of the inertial amplification mechanism with the constraining thick beams.

In Table 5.1, comparison of band gap limits can be seen. Notice that very wide band gap can be obtained by adding constraining beams to the inertial amplification mechanism. However, thickness of the constraining beams are determined without

considering other parameters. It would be beneficial to perform an optimization study for other parameters with certain constraints.

Table 5.1. Band gap limits of inertial amplification mechanisms.

	ω_1	ω_2	ω_2/ω_1	BW_a	BW_g
Without the Constraining Beams	267	600	2.28	0.78	0.85
With the Constraining Slender Beams	240	1193	4.97	1.33	1.78
With the Constraining Thick Beams	241	1681	6.96	1.50	2.26

5.1. Optimization of the Inertial Amplification Mechanism with the Constraining Thick Beams

For the optimization study, model of the inertial amplification mechanism with constraining beams are created with Python script. Optimization study is performed using MATLAB which can modify the variables of the Python script, call the ABAQUS solver and read the modal frequency results.

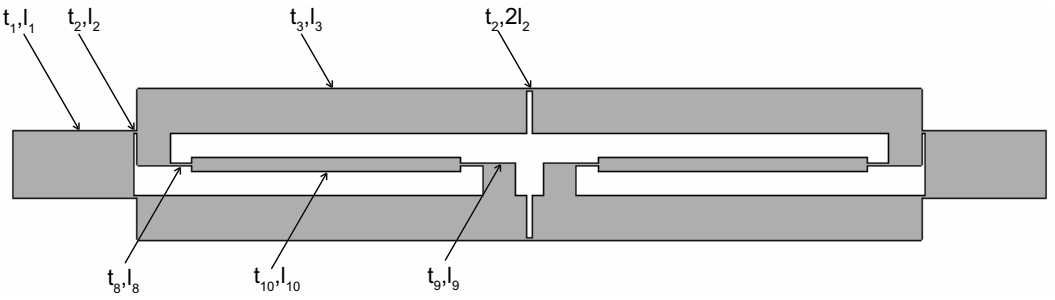


Figure 5.8. Inertial amplification mechanism with constraining thick beams which optimized under m_{tot}, k_{tot} and l_{tot} constraints. Here, t_i and l_i are thickness and length of the ith beam segment, respectively.

First of all, t_1, t_2 and t_3 values are optimized in order to increase ω_2/ω_1 ratio. Total mass (m_{tot}), total stiffness (k_{tot}) and total length (l_{tot}) values are kept constant as $m_{tot} = 0.0657$ kg, $k_{tot} = 575000$ N/m and $l_{tot} = 0.094$ m. In order to meet these three requirements, l_1, l_2 and l_3 should satisfy the constraints given in Equations 5.2-5.4. The optimization problem can be stated as follows:

min ω_{p1}/ω_{p2}

Free variables: t_1, t_2 and t_3

Fixed variables: $l_8 = 2$ mm, $t_8 = 0.2$ mm, $l_9 = 3$ mm and $t_{10} = 1.64$ mm

Material properties: $\rho = 7800$ kg/m^3, $E = 210$ GPa

Constraints:

$$l_1 = \frac{m_{tot}}{2b\rho t_1} - \frac{2Ebt_2^4}{3k_{tot}(t_3 - t_2)^2 t_1} - \frac{2t_3 l_3}{t_1} \tag{5.2}$$

$$l_2 = \frac{Ebt_2^3}{6k_{tot}(t_3 - t_2)^2} \tag{5.3}$$

$$l_3 = \left(l_{tot} - \frac{m_{tot}}{b\rho t_1} + \frac{4Ebt_2^4}{3k_{tot}(t_3 - t_2)^2 t_1} - \frac{2Ebt_2^3}{3k_{tot}(t_3 - t_2)^2} \right) \frac{t_1}{2t_1 - 4t_3} \tag{5.4}$$

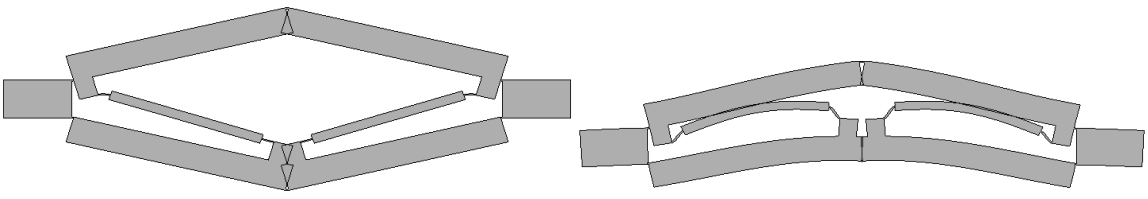
$$l_4 = 2l_2 \tag{5.5}$$

$$t_4 = t_2 \tag{5.6}$$

$$t_9 = (t_1 - 2t_2 + t_8)/2 \tag{5.7}$$

$$l_{10} = l_3 - 2l_9 - 2l_8 - 1 \text{ mm} \tag{5.8}$$

The optimization problem is solved by using Newton's method and genetic algorithm. t_1, t_2 and t_3 values converge to 7.3 mm, 0.2 mm and 4.8 mm, respectively, by both methods. The ω_2/ω_1 ratio is found to be 14.8.



(a) $\omega_1 = 183$ Hz (b) $\omega_2 = 2705$ Hz

Figure 5.9. First and second mode shapes of the inertial amplification mechanism with constraining thick beams which is optimized under m_{tot}, k_{tot} and l_{tot} constraints.

Then, t_1, t_2 and t_3 values are optimized without m_{tot} and k_{tot} constraints in order to create the widest possible band gap using such a mechanism. l_1, l_2 and l_3 constraints

are modified as

$$l_1 = 12 \text{ mm} \tag{5.9}$$

$$l_2 = 5t_2 \tag{5.10}$$

$$l_3 = (l_{tot} - 2l_1 - 4l_2)/2 \tag{5.11}$$

In order to prevent local buckling problems, $l_2 = 5t_2$ constraint is given since there isn't a k_{tot} constraint anymore. Also, l_1 is taken as 12mm in order to ensure firm connection at the ends when periodic arrays are formed.

The optimization problem is repeated with these modified constraints by using Newton's method and genetic algorithm. t_1, t_2 and t_3 values converge to 9.76mm, 0.1mm and 8.92mm, respectively, by both methods. The ω_2/ω_1 ratio is found to be 32.2. The optimized mechanism and its first two mode shapes are given in Figures 5.10 and 5.11, respectively.

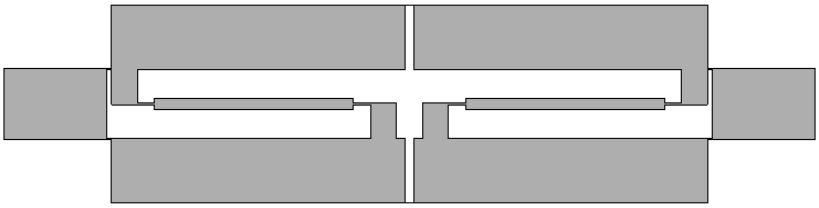
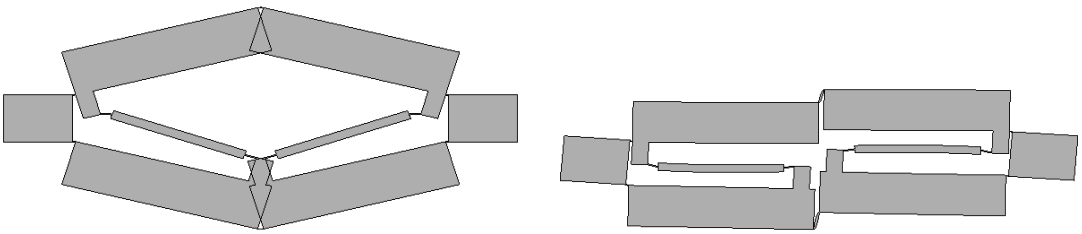


Figure 5.10. Inertial amplification mechanism with constraining thick beams which is optimized without m_{tot} and k_{tot} constraints.



(a) $\omega_1 = 67$ Hz (b) $\omega_2 = 2159$ Hz

Figure 5.11. First and second mode shapes of the inertial amplification mechanism with constraining thick beams which is optimized without m_{tot} and k_{tot} constraints.

Frequency response plot of the optimized mechanism can be seen in Figure 5.12. Notice that there is no resonance peak in between 67-2159 Hz which shows that this mechanism has the ability to isolate vibrations in a very wide frequency range.

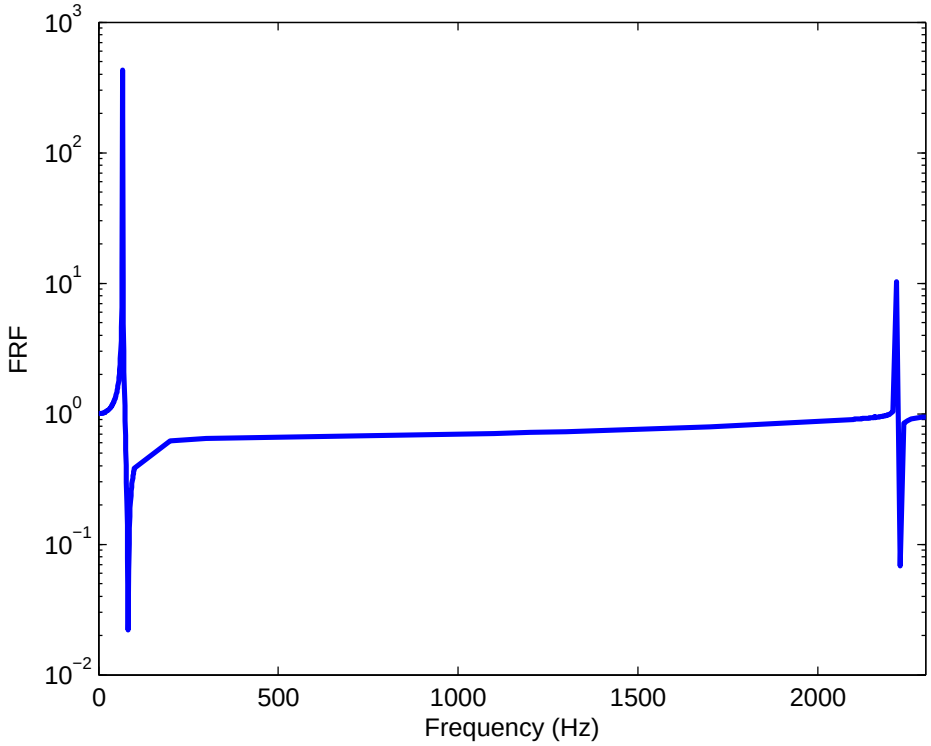


Figure 5.12. Frequency response of the inertial amplification mechanism with constraining thick beams which is optimized without m_{tot} and k_{tot} constraints.

Table 5.2. Comparison of band gap limits of the optimized inertial amplification mechanisms.

	ω_1	ω_2	ω_2/ω_1	BW_a	BW_g
Without the Constraining Beams	267	600	2.28	0.78	0.85
With m_{tot}, k_{tot} and l_{tot} Constraints	183	2705	14.8	1.75	3.59
Without m_{tot}, k_{tot} and l_{tot} Constraints	67	2159	32.2	1.88	5.50

If the mechanisms seen in Figure 5.1 and Figure 5.11 are compared, it is seen that ω_2/ω_1 ratio is increased from 2.28 to 32.2 after the optimization studies. Therefore, it is expected that the three-dimensional lattices built with these optimized inertial amplification mechanisms also have a wide phononic band gap in between 67-2159 Hz.

5.2. Optimization of the Inertial Amplification Mechanism with the Constraining Slender Beams Considering Manufacturing Constraints

Up to this point, in order to obtain the widest possible band gap, different inertial amplification mechanisms with constraining beams are analyzed without considering prototype manufacturing. At this point, manufacturing and operational constraints are considered in the optimization study.

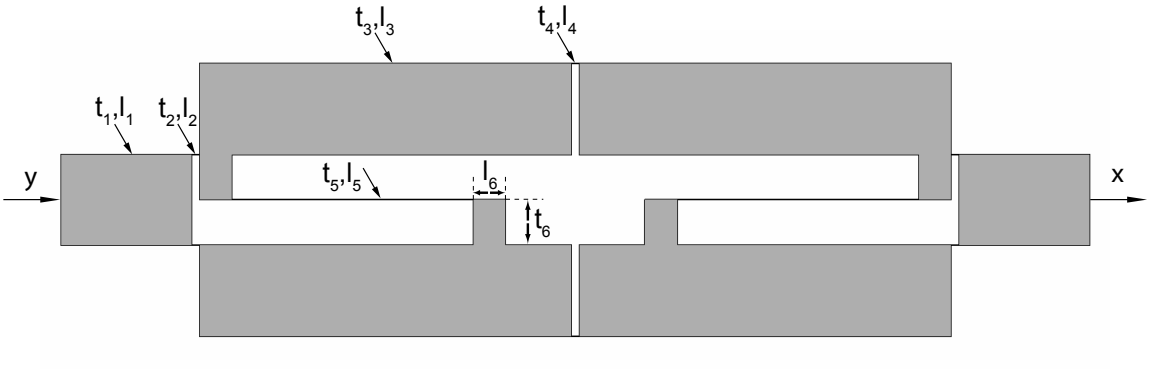


Figure 5.13. Dimensions of the inertial amplification mechanism with constraining slender beams. Here, y is the input and x is the output displacement. Also, t_i and l_i represent the thickness and length of the ith beam segment.

Cross-sections of each thick beams are chosen equal so that it is possible to cut each beam from the same aluminum beam. In order to widen the stop band t_1, t_2 and t_4 should attain small values. Considering manufacturing accuracy, t_2 and t_4 are chosen as 0.2 mm. In order to fit the constraining beams between the upper and lower thick beams, t_1 is chosen as 30 mm. Finally, t_3 is also chosen as 30 mm. Also, to obtain the widest possible band gap, remaining free variables of the inertial amplification mechanism seen in Figure 5.13 is optimized. After all these stated constraints, the optimization problem can be stated as follows:

min ω_{p1}/ω_{p2}

Free variables: $l_1,\ l_3,\ l_5,\ t_5,\ l_6$

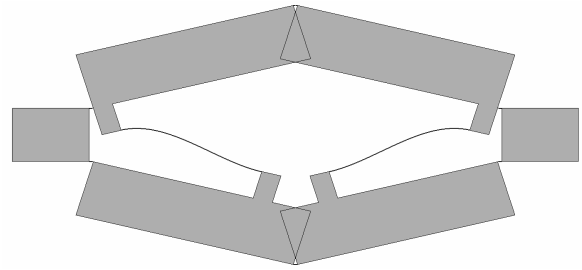
Fixed variables: $t_1 = t_3 = 30$ mm, $t_2 = t_4 = 0.2$ mm

Material properties: $\rho = 7800$ kg/m^3, $E = 210$ GPa

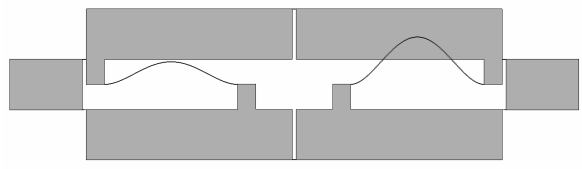
Constraints: $l_2 = l_4 = 10t_2$, $t_6 = (t_1 - 2t_2 + t_5)/2$

After the optimization study, values of l_1, l_3, l_5, t_5, and l_6 are found to be 36 mm, 102 mm, 66 mm, 0.25 mm, and 9 mm, respectively.

The first two mode shapes of the optimized unit cell mechanism can be seen in Figure 5.14. Notice that the upper limit of the band gap is determined by the bending modes of the constraining beams (see Figure 5.14b). If the thicknesses of these constraining beams are increased, the frequency of the bending mode will be larger. However, this will also increase the frequency of the first mode. As a result, BW_g would decrease.



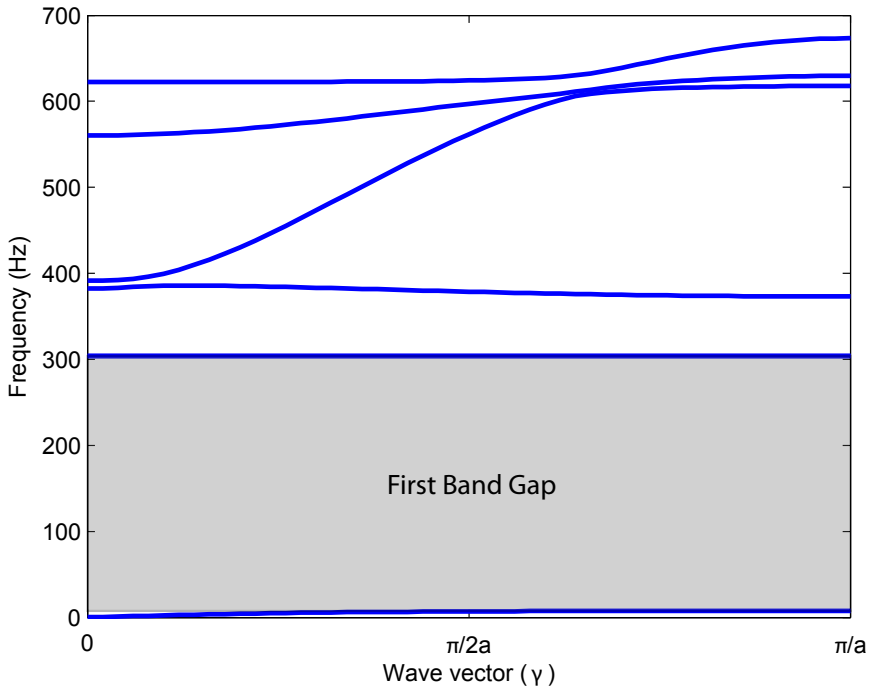
(a) $\omega_1 = 6.9$ Hz



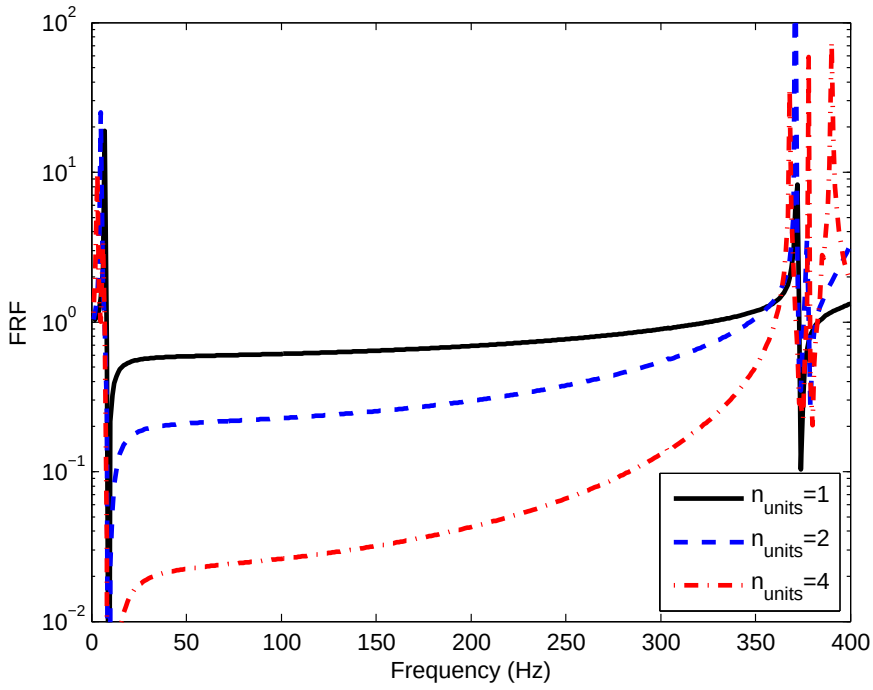
(b) $\omega_2 = 303.6$ Hz

Figure 5.14. First and second vibration modes of the optimized inertial amplification mechanism using 2D model.

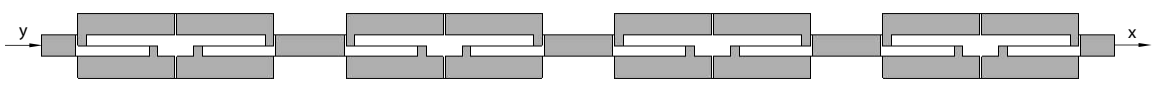
In order to obtain band structure of the infinite periodic array of the inertial amplification mechanism, mass ($\boldsymbol{M}$) and stiffness ($\boldsymbol{K}$) matrices of the unit cell mechanism are generated as in the previous chapter. After substituting Equation 4.32 into Equation 4.31, modified mass ($\tilde{\boldsymbol{M}}$) and stiffness ($\tilde{\boldsymbol{K}}$) matrices are obtained. Equation 4.33 is solved for γ from 0 to π/a in order to obtain band structure of the infinite periodic array of the unit cell mechanism.



(a)



(b)



(c)

Figure 5.15. (a) Band structure of the infinitely periodic array. (b) Frequency responses of finite periodic arrays with various number of unit cells. (c) Finite periodic array with 4 unit cells.

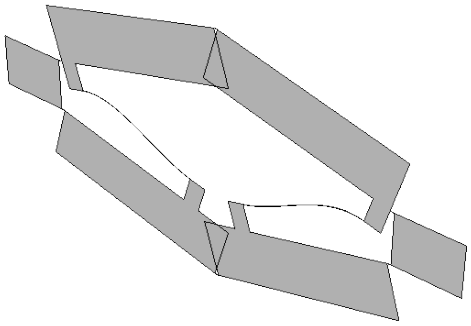
It is expected that the stop band of the unit cell mechanism will occur in between the first (6.9 Hz) and second (303.6 Hz) modes. Band structure of the infinitely periodic array is given in Figure 5.15a, which shows that the first band gap is formed in the frequency range $7.8 - 303.6$ Hz as expected. In Figure 5.15b, frequency response function (FRF) plots of finite periodic arrays of the unit cell are depicted. Here, FRF is defined as output to input acceleration ratio ($|\ddot{x}(\omega)/\ddot{y}(\omega)|$). It is seen that the stop band frequency range does not change as the number of unit cells in the one-dimensional array increases, but only the stop band gets deeper. It is seen that the stop band is formed in the frequency range $7.8-373$ Hz, which is larger than the band gap frequency range of the infinite case as the upper limit increased from 303.6 Hz to 373 Hz. The vibration mode at 303.6 Hz (see Figure 5.14b) is absent in the FRF plot because, in this mode, the constraining beams vibrate transversely without causing any displacement at the end sections where FRF is calculated.

In the manufactured prototype, upper limit will be determined by the out-of-plane mode. It is beneficial to examine the optimized inertial amplification mechanism using 3D shell elements in order to see upper limit out-of-plane mode. Out-of-plane thickness is chosen as 30 mm. In Figure 5.16, first three mode shapes of the inertial amplification mechanism can be seen. Notice that an out-of-plane mode occurs in between band gap frequency range as seen Figure 5.16b. This mode determines the upper limit of the band gap.

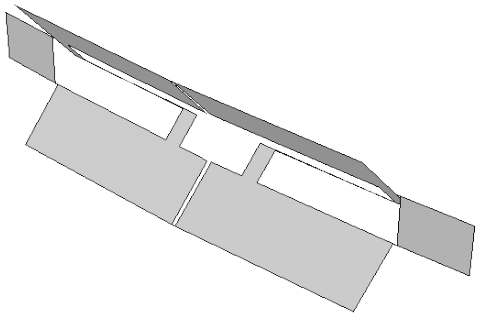
Table 5.3. Frequency limits of the first band gap of the inertial amplification mechanism with constraining beams.

	ω_l	ω_u	ω_u/ω_l	BW_a	BW_g
2D Model	6.91 Hz	303.6 Hz	38.9	1.90	6.08
3D Shell Model	6.95 Hz	164.7 Hz	23.7	1.84	4.66

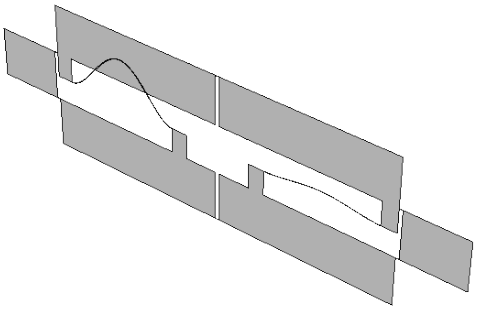
Nevertheless, the band gap obtained for this optimized inertial amplification mechanism with constraining slender beams is very wide. It is expected that if a 3D structure is built using such a mechanism and with the help of the assembly techniques introduced in previous chapter, it will also have very wide band gap.



(a) $\omega_1 = 6.95$ Hz



(b) $\omega_2 = 164.7$ Hz



(c) $\omega_3 = 275.0$ Hz

Figure 5.16. First, second and third vibration modes of the optimized inertial amplification mechanism using 3D shell model.

6. MANUFACTURING AND EXPERIMENTAL VERIFICATION

In this chapter, manufacturing processes of the distributed parameter models which are designed and analyzed in the previous two chapters are explained. Then, their experimental frequency responses are obtained and compared with numerical ones. First, manufacturing and experimental verification of the octahedron structure and the 2×3 array of octahedron structures are performed. Then, the ultra wide band gap structure is manufactured and existence of ultra wide band gap in such a structure is verified.

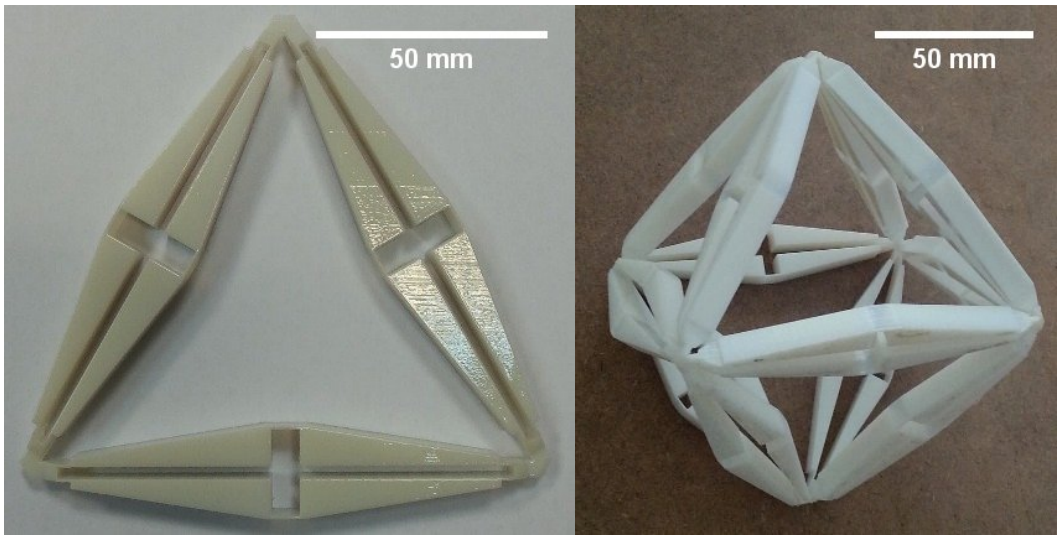
6.1. Manufacturing of the Octahedron Structures

Manufacturing of the designed 3D octahedron structures using a conventional machining method is very hard since there are thin sections oriented in various directions in 3D space. However, 3D printers can easily handle intricate designs in 3D. Therefore, the octahedron structure and the 2×3 array of octahedron structures are manufactured using a 3D printer. Figure 6.1 shows manufactured 2×3 array of octahedron structures inside the 3D printer.



Figure 6.1. Manufacturing of the octahedron structure with 3D printer.

Octahedron structure can be manufactured using four equilateral triangles with appropriate edge angles. First, these equilateral triangles are manufactured using a 3D printer (see Figure 6.2a). Then, octahedron structure is built by combining four of these equilateral triangles as seen in Figure 6.2b.



(a) (b)

Figure 6.2. (a) Equilateral triangles and (b) the octahedron structure.

Building the octahedron structure using equilateral triangles takes too much time. Thus, the 2×3 array of octahedron structures is manufactured as a whole structure using a 3D printer as seen in Figure 6.3.

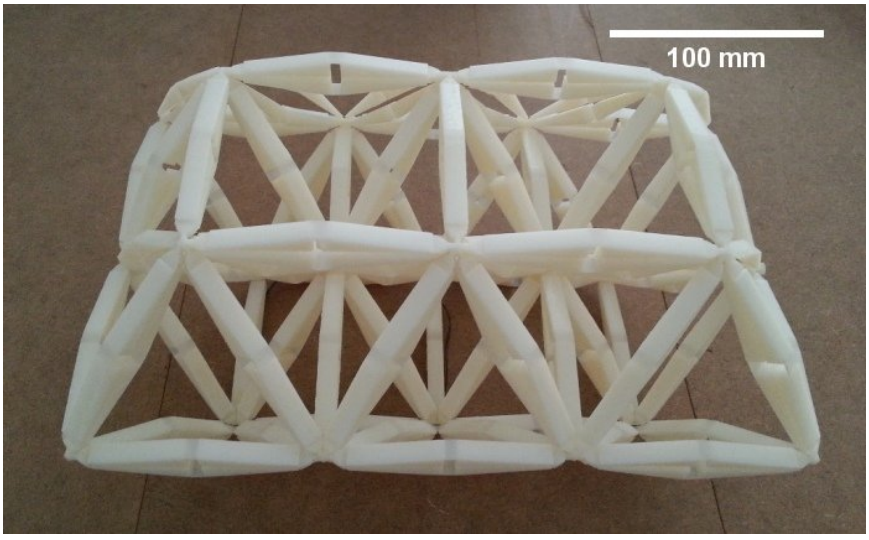


Figure 6.3. The 2×3 array of the octahedron structures.

6.2. Experimental Verification of the Octahedron Structures

Experimental setup of the octahedron structure is seen in Figure 6.4. Here, the hanged octahedron structure is excited from one end, where input acceleration is measured by an impedance head and a laser vibrometer is pointed to the other end for measuring the output velocity. Both input and output are monitored using a data acquisition device that is connected to a computer. Hanning window is used in this experiment to reduce spectral leakage. Frequency response of the structure is calculated using H_1 estimation [67].

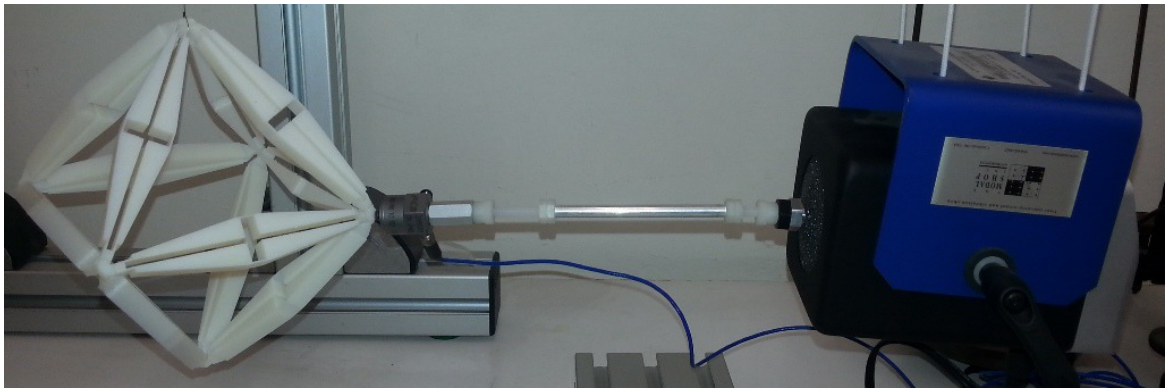


Figure 6.4. Experimental setup of the octahedron structure.

Frequency response of the octahedron structure is obtained experimentally and by FEM in longitudinal direction as seen in Figure 6.5. There is a slight upward frequency shift in the experimental result. This shift is mainly caused by dimensional inaccuracy and variability in the material parameters (i.e., ρ and E) during 3D printing. The 3D printer has 16 μm layer deposition accuracy when polymer is deposited on polymer. However, to form the holes in the structure, wax is also deposited and accuracy in the polymer-wax interface is decreasing, which creates dimensional inaccuracy especially in the thin sections of the structure. However, in all FEM calculations nominal values for the mechanism dimensions and material parameters are used. Finally, in the FEM, polymer material is assumed to be linear as small amplitude excitations are applied during testing. Yet, small amount of nonlinearity in the material properties may also add to the mismatch between numerical and experimental results. Nevertheless, the numerical and experimental FRF results are quite close.

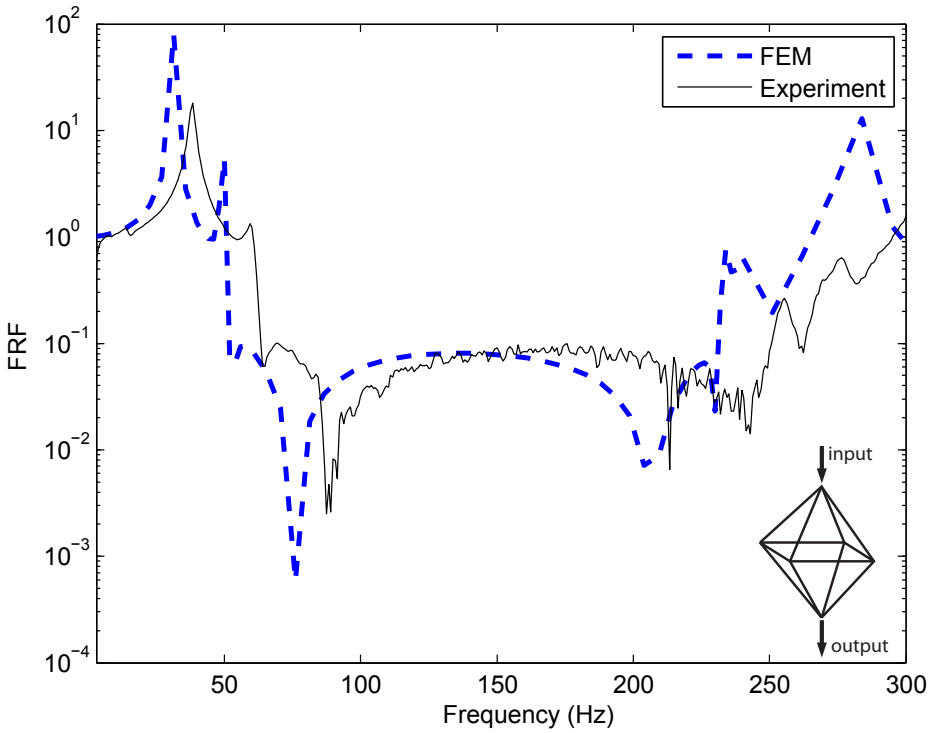


Figure 6.5. Experimental and numerical frequency responses of the octahedron structure in longitudinal direction.

Experimental setup of the 2×3 array of octahedron structures is also seen in Figure 6.6. Experimental frequency response of the 2×3 array of octahedron structures can be obtained via a similar procedure followed for the octahedron structure.

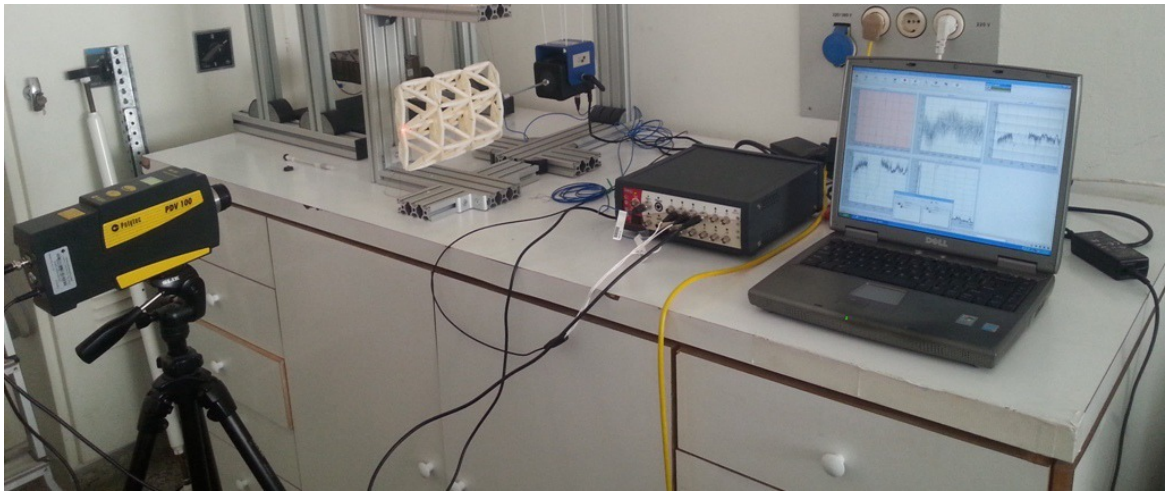


Figure 6.6. Experimental setup of the 2×3 array of octahedron structures.

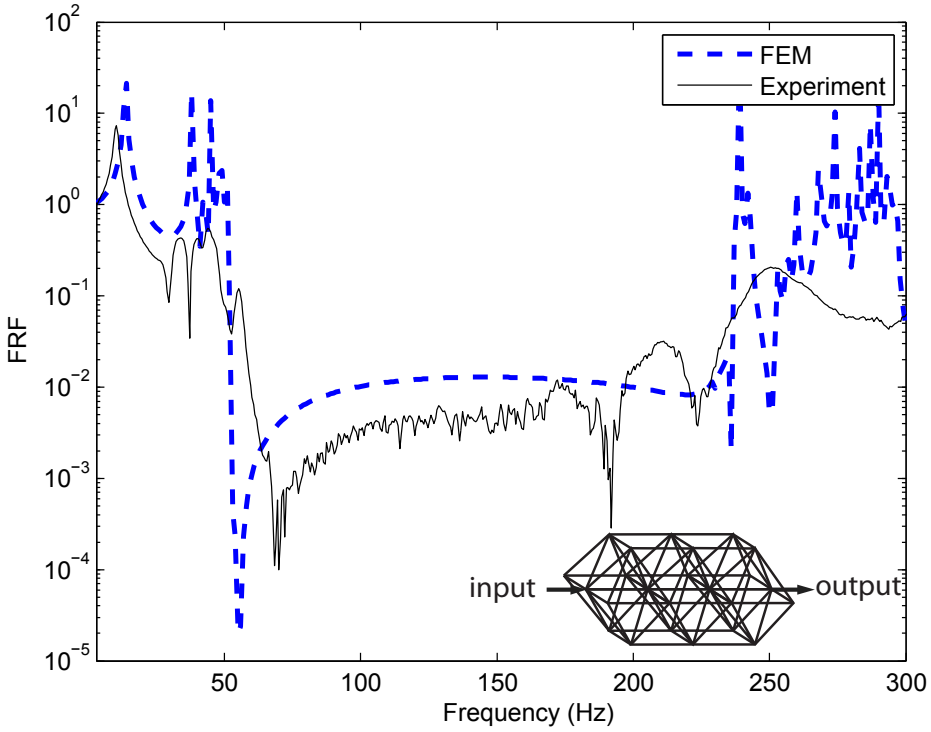
Experimental and numerical frequency response results of the 2×3 array of octahedron structures are given in Figure 6.7a. It is seen that the experimental and numerical FRF results are quite similar. Especially, the resonant peaks that set the limits for the stop band appear at similar frequencies. However, as there is no damping in the FEM result, the peak magnitudes do not match well.

In order to match the resonance peak values in the experimentally obtained FRF, structural damping is added to the FE model. Figure 6.7b shows that structural damping ratio $\eta = 0.03$ yields similar peak values for the resonances in the experimental and numerical FRF plots.

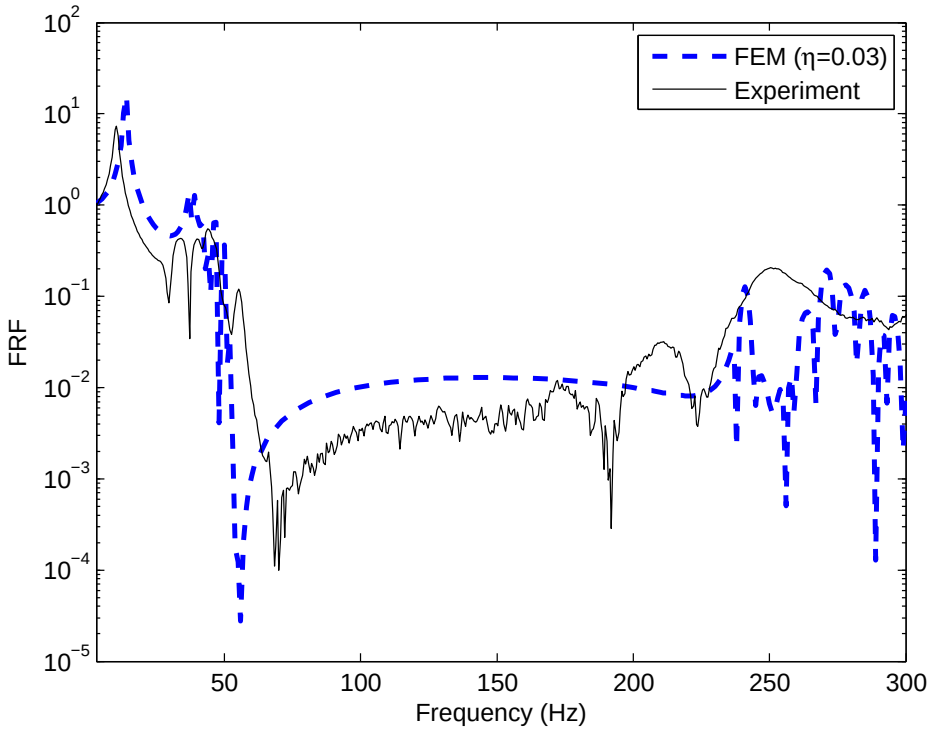
Finally, the 2×3 octahedron array is also excited in an oblique axis, which makes 55° with the x, y and z axes, to generate excitations in all axes. Frequency response of the structure is obtained numerically (Figure 6.8a) and experimentally (Figure 6.8b). In the numerical and experimental results, it is seen that the resonant peaks that set the lower limit for the first stop band occur at similar frequencies. But the resonant peaks of upper limit are not as clear as the ones of the lower limit due to damping. Moreover, experimental results deviate from the numerical results at high frequencies due to variability in material parameters (ρ and E) and dimensional inaccuracies during 3D printing. Nevertheless, both finite element and experimental results show a wide vibration stop band at similar frequencies. Hence, the 3D structure is capable of isolating excitations in longitudinal and two transverse directions in a very wide frequency range.

6.3. Manufacturing of the Ultra Wide Band Gap Structure

Prototype of the ultra wide band gap structure is manufactured using steel flexure hinges and extruded aluminum beams with special cross-sections as seen in Figure 6.9. The reason of using aluminum beams is that they can be cut easily in desired dimensions. Use of the nuts and bolts through the channels on the aluminum beam is fairly easy to use. In this prototype, flexible links are fixed using special rectangular washers and bolts. These rectangular washers are cut out from aluminum sheets in the

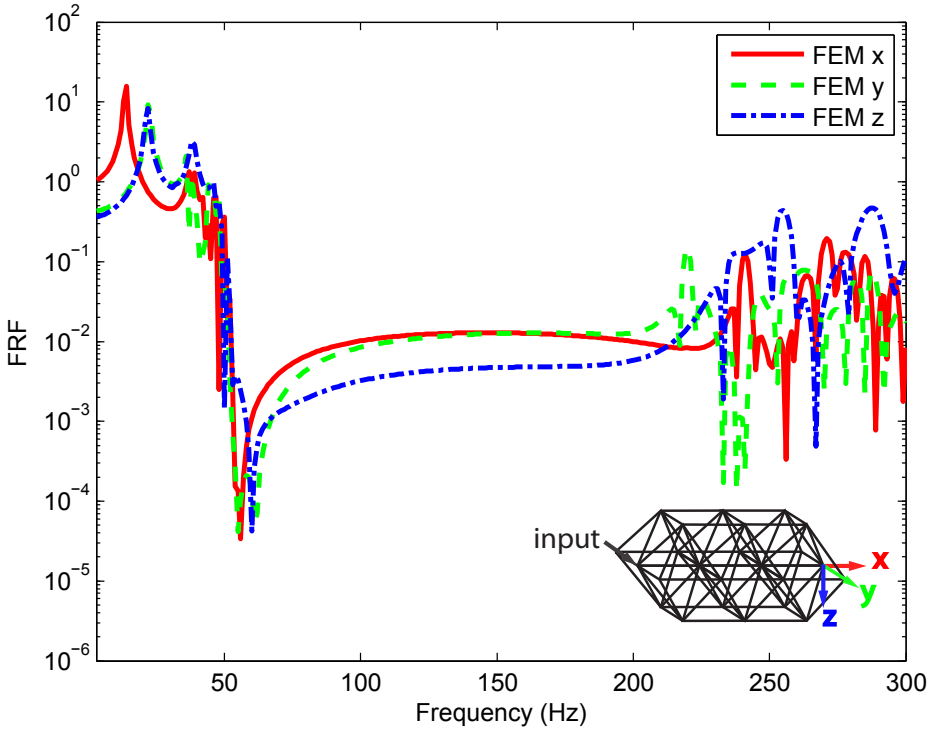


(a)

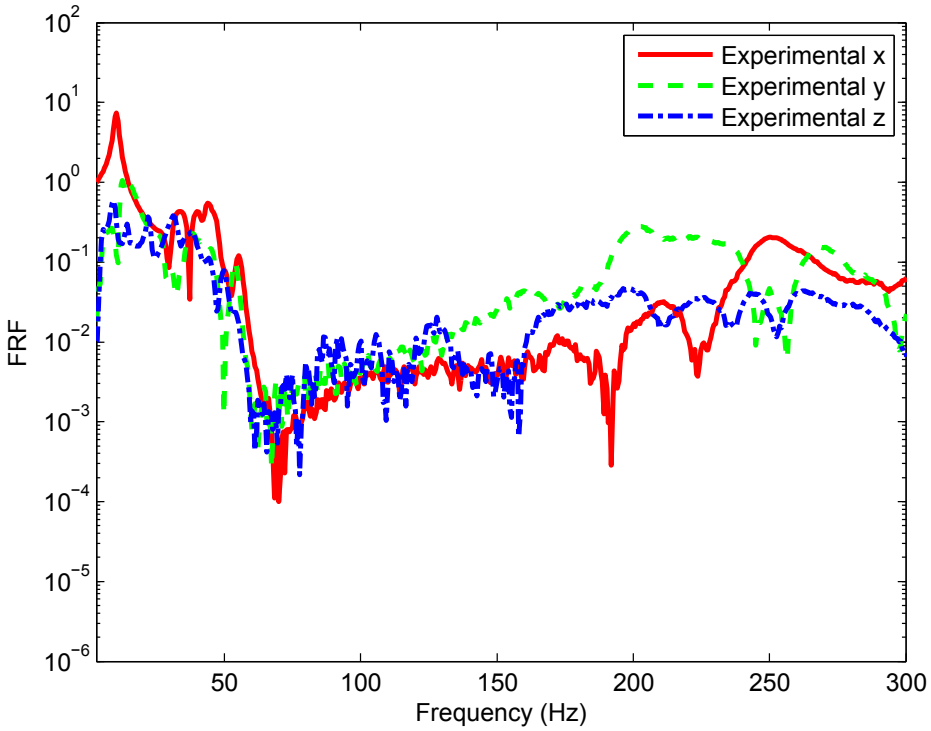


(b)

Figure 6.7. Experimental and numerical frequency responses of the 2×3 octahedron array in longitudinal direction. Here, the numerical FRF result is obtained (a) for the undamped case and (b) for $\eta = 0.03$.



(a)



(b)

Figure 6.8. Frequency responses of the 2×3 octahedron array in longitudinal (x) and two transverse (y and z) directions. (a) FEM results for $\eta = 0.03$, (b) experimental results.

appropriate dimensions and drilled. In this way, spring steels and bars are united in a straight line. This allows bending of the spring steels from this line in either direction.



Figure 6.9. The prototype of the inertial amplification mechanism with ultra wide band gap.

6.4. Experimental Verification of the Ultra Wide Band Gap Structure

In the previous chapter, an ultra wide band gap was obtained using an inertial amplification mechanism with constraining beams. In the numerical studies, material properties were taken as $\rho = 7800$ kg/m^3 and $E = 210$ GPa. However, ultra wide band gaps can also be obtained by using different materials. A prototype of the ultra wide band gap mechanism is manufactured as seen in Figure 6.9. In this mechanism, thick aluminum beams ($\rho = 2680$ kg/m^3 and $E = 69$ GPa) are connected via steel flexure hinges ($\rho = 7800$ kg/m^3 and $E = 210$ GPa).



Figure 6.10. Excitation and measurement points for the ultra wide band gap structure.

The numerical frequency response of this structure is obtained using finite element method. To obtain the experimental frequency response, the prototype is hanged by

elastic cords and excited from one end via a shaker (see Figure 6.11). Input acceleration is measured by an impedance head and an accelerometer is placed at the other end for measuring the output acceleration. Excitation and measurement points are shown in Figure 6.10. Hanning window is used in this experiment to reduce spectral leakage. Frequency response of the structure is calculated using H_1 estimation [67]. Figure 6.12 shows the experimental and numerical frequency response results. The first stop band occurs in between 13 to 274 Hz in the numerical FRF whereas it occurs in between 11 to 268 Hz in the experimental FRF. Therefore, a close match is observed between the numerical and experimental frequency response results.

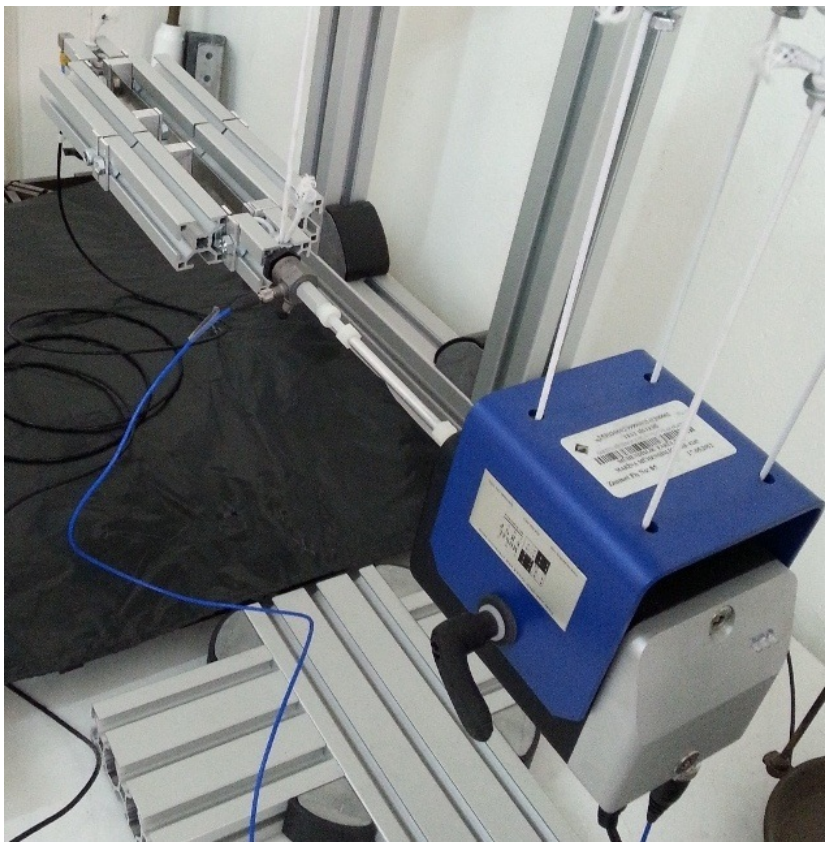


Figure 6.11. Experimental setup for the ultra wide band gap structure.

These results validate that the inertial amplification mechanism with constraining beams is capable of generating ultra wide stop bands. Note that the inertial amplification mechanisms are scalable. Thus, its band gap frequency range can be shifted by changing its dimensions or material properties. As a result, vibration isolators or

elastic wave filters working at various frequency ranges can be generated using this mechanism.

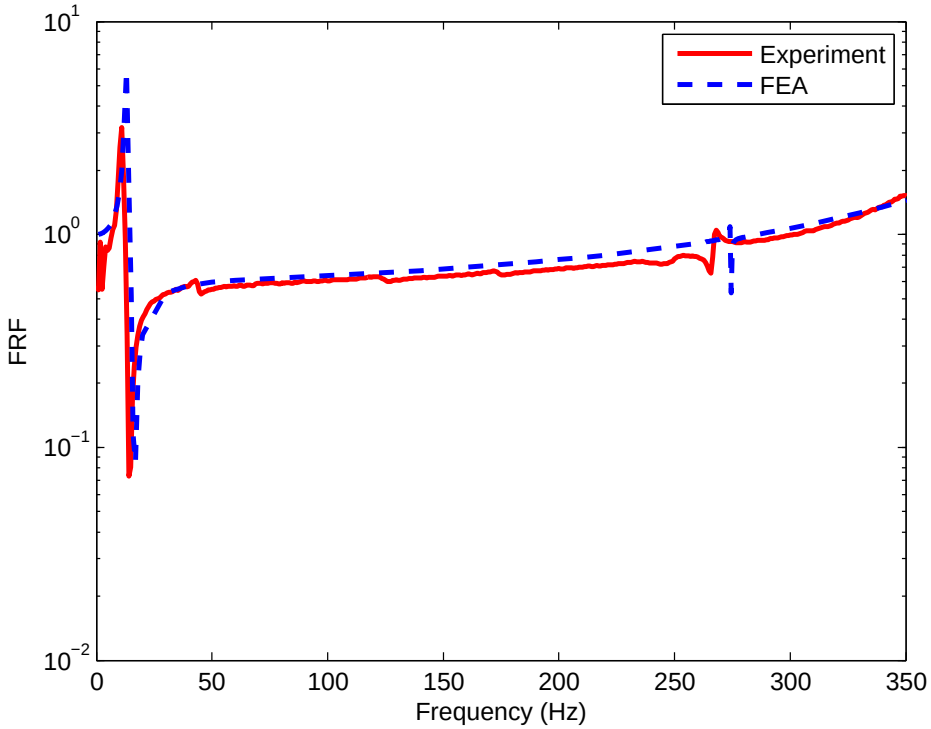


Figure 6.12. Experimental and numerical frequency response results of the ultra wide band gap structure.

Table 6.1. Numerical and experimental band gap limits of the ultra wide band gap mechanism.

	ω_l	ω_u	ω_u/ω_l	BW_a	BW_g
FEA with Steel Thick Beams	6.9 Hz	164.7 Hz	23.7	1.84	4.66
FEA with Al Thick Beams	13 Hz	274 Hz	21.07	1.82	4.37
Experiment	11 Hz	268 Hz	24.5	1.83	4.75

7. CONCLUSIONS

In this study, three-dimensional (3D) structures with embedded inertial amplification mechanisms are designed and analyzed. First of all, infinite and finite periodic SC, BCC and FCC lattices composed of springs and masses are investigated. For the infinite periodic lattices, band gaps are formed at various frequency ranges by changing the ratio of the masses within their unit cells. There is a semi-infinite band gap, which is above the three branches, in the phononic band structure of the SC lattice. When inertial amplification mechanisms with rigid amplifier links are embedded to this lattice, a semi-infinite band gap is formed which starts at a lower frequency. In the BCC lattice, a band gap can be formed between the 3^{rd} and 4^{th} branches for most of the mass ratios, however, in the FCC lattice a band gap can be formed for a limited range of mass ratios. In order to obtain large bandwidth in BCC and FCC lattices, one of the masses in their unit cells should approach to zero. However, when all mass ratios are considered, the BCC lattice offers larger bandwidths. Furthermore, band gaps at lower frequencies can be obtained by using a BCC lattice. When inertial amplification mechanisms are added to both BCC and FCC lattices, the band gaps are formed at much lower frequencies. More importantly, it is shown that the normalized bandwidths of these lattices remain large for all amplifier mass ratios. However, the BCC lattice with inertial amplification slightly outperforms the FCC lattice with inertial amplification in terms of obtaining wider band gaps at lower frequencies. Finally, instead of rigid links, finite stiffness links are utilized in the amplification mechanisms. In that case, the inertial amplification induced phononic band gaps have upper limits. Yet, for moderate stiffness values, these upper limits are quite high. Thus, quite wide low frequency band gaps can be obtained for SC, BCC and FCC lattices with embedded inertial amplification mechanisms.

For the finite periodic lattices, as the number of unit cells increase, especially along the excitation direction, the depth of the stop bands increase. However, it is shown that inertial amplification method can yield wide and deep stop bands at low frequencies using moderate number of unit cells in both BCC and FCC lattices.

In order to physically realize these three-dimensional lattices, a distributed parameter inertial amplification mechanism is designed. To that end, the resonance and antiresonance frequencies of the inertial amplification mechanism that will be the building block of the 3D structures are attained analytically and by finite element method. In order to obtain a wide vibration stop band, the dimensions of the building block mechanism are optimized. It is seen that the analytical and numerical resonance and antiresonance frequency results of the optimized mechanism are similar. Then, one-dimensional finite and infinite arrays of mechanisms are formed. It is demonstrated that vibration stop bands of these structures coincide and they are formed between the first two resonance frequencies of the building block mechanism. Using the optimized inertial amplification mechanism, an octahedron structure is built. It is revealed that unlike 1D or 2D assembly of the building block mechanisms, the first vibration stop band in a 3D assembly not necessarily span the interval between the first two resonance frequencies of the building block mechanism. To enforce this condition, end segments of the mechanism are redesigned. Using this modified inertial amplification mechanism, finite element models of an octahedron structure and a 2×3 array of octahedron structures are formed and these structures are manufactured using a 3D polymer printer. The experimental and numerical frequency responses yielded stop bands at similar frequencies. Moreover, to match the resonant peak magnitudes, structural damping is added to the finite element model. Finite element analysis for excitations in longitudinal and two transverse directions show that wide and deep vibration stop bands at low frequencies are obtained. Finally, the numerical frequency response results are validated with the experimental results.

Also, a new inertial amplification mechanism is designed by adding constraining beams that reduce the degree of freedom of the equivalent rigid link mechanism. Consequently, the upper limit frequency of the first band gap is increased significantly. Thus, it is possible to create ultra wide band gaps using this new mechanism. An optimization study is conducted to maximize the first phononic gap. Analysis of both one-dimensional finite and infinite arrays show ultra wide gaps, which surpass the ones that can be obtained by conventional band gap generation methods. The unit cell mechanism is manufactured and its seen that the experimental and numerical fre-

quency response results coincide. Therefore, it shown that the unit cell designed in this study has the capability of preventing propagation of vibrations in ultra wide frequency ranges.

To sum up, it is shown that 3D structures built with inertial amplification mechanisms have the capability of preventing propagation of vibrations coming from all directions in a very wide frequency range.

As future work, 3D structures can be built using the ultra wide band gap mechanisms with constraining beams. Also, these 3D structures can be investigated for possible application areas. Furthermore, it is seen that length of the flexure hinges used in the mechanism affect the band gap frequency range significantly. It may be possible to create active vibration isolation structures, which has the ability to modify the band gap frequency range depending on the excitation.

REFERENCES

1. Kushwaha, M. S., "Classical band structure of periodic elastic composites", *International Journal of Modern Physics B*, Vol. 10, No. 09, pp. 977–1094, 1996.

2. Yu, D., J. Wen, H. Shen, Y. Xiao, and X. Wen, "Propagation of flexural wave in periodic beam on elastic foundations", *Physics Letters A*, Vol. 376, No. 4, pp. 626–630, 2012.

3. Shen, H., J. Wen, D. Yu, and X. Wen, "The vibrational properties of a periodic composite pipe in 3D space", *Journal of Sound and Vibration*, Vol. 328, No. 1, pp. 57–70, 2009.

4. Xiuchang, H., J. Aihua, Z. Zhiyi, and H. Hongxing, "Design and optimization of periodic structure mechanical filter in suppression of foundation resonances", *Journal of Sound and Vibration*, Vol. 330, No. 20, pp. 4689–4712, 2011.

5. Sun, J. H. and T. T. Wu, "Propagation of acoustic waves in phononic-crystal plates and waveguides using a finite-difference time-domain method", *Physical Review B*, Vol. 76, No. 10, p. 104304, 2007.

6. Cervera, F., L. Sanchis, J. Sanchez-Perez, R. Martinez-Sala, C. Rubio, F. Meseguer, C. López, D. Caballero, and J. Sánchez-Dehesa, "Refractive acoustic devices for airborne sound", *Physical Review Letters*, Vol. 88, No. 2, p. 023902, 2001.

7. Hussein, M. I., K. Hamza, G. M. Hulbert, and K. Saitou, "Optimal synthesis of 2D phononic crystals for broadband frequency isolation", *Waves in Random and Complex Media*, Vol. 17, No. 4, pp. 491–510, 2007.

8. Kushwaha, M., P. Halevi, L. Dobrzynski, and B. Djafari-Rouhani, "Acoustic band structure of periodic elastic composites", *Physical Review Letters*, Vol. 71, No. 13, pp. 2022–2025, 1993.

9. Goffaux, C. and J. Vigneron, "Theoretical study of a tunable phononic band gap system", *Physical Review B*, Vol. 64, No. 7, p. 075118, 2001.

10. Sigmund, O. and J. S. Jensen, "Systematic design of phononic band–gap materials and structures by topology optimization", *Philosophical Transactions of the Royal Society of London. Series A: Mathematical, Physical and Engineering Sciences*, Vol. 361, No. 1806, pp. 1001–1019, 2003.

11. Phani, A. S., J. Woodhouse, and N. A. Fleck, "Wave propagation in two-dimensional periodic lattices", *The Journal of the Acoustical Society of America*, Vol. 119, No. 4, pp. 1995–2005, 2006.

12. Yilmaz, C., G. M. Hulbert, and N. Kikuchi, "Phononic band gaps induced by inertial amplification in periodic media", *Physical Review B*, Vol. 76, No. 5, p. 054309, 2007.

13. Yilmaz, C. and G. M. Hulbert, "Theory of phononic gaps induced by inertial amplification in finite structures", *Physics Letters A*, Vol. 374, No. 34, pp. 3576–3584, 2010.

14. Robillard, J., O. Matar, J. Vasseur, P. Deymier, M. Stippinger, A. Hladky-Hennion, Y. Pennec, and B. Djafari-Rouhani, "Tunable magnetoelastic phononic crystals", *Applied Physics Letters*, Vol. 95, No. 12, p. 124104, 2009.

15. Spadoni, A., M. Ruzzene, S. Gonella, and F. Scarpa, "Phononic properties of hexagonal chiral lattices", *Wave Motion*, Vol. 46, No. 7, pp. 435–450, 2009.

16. Tee, K., A. Spadoni, F. Scarpa, and M. Ruzzene, "Wave propagation in auxetic tetrachiral honeycombs", *Journal of Vibration and Acoustics*, Vol. 132, p. 031007, 2010.

17. Yu, D., Y. Liu, G. Wang, L. Cai, and J. Qiu, "Low frequency torsional vibration gaps in the shaft with locally resonant structures", *Physics Letters A*, Vol. 348,

No. 36, pp. 410–415, 2006.

18. Xiao, Y., B. R. Mace, J. Wen, and X. Wen, "Formation and coupling of band gaps in a locally resonant elastic system comprising a string with attached resonators", *Physics Letters A*, Vol. 375, No. 12, pp. 1485–1491, 2011.

19. Leamy, M. J., "Exact wave-based Bloch analysis procedure for investigating wave propagation in two-dimensional periodic lattices", *Journal of Sound and Vibration*, Vol. 331, No. 7, pp. 1580–1596, 2012.

20. Wang, Y.-Z., F.-M. Li, W.-H. Huang, X. Jiang, Y.-S. Wang, and K. Kishimoto, "Wave band gaps in two-dimensional piezoelectric/piezomagnetic phononic crystals", *International Journal of Solids and Structures*, Vol. 45, No. 14, pp. 4203–4210, 2008.

21. Jensen, J. S., "Phononic band gaps and vibrations in one-and two-dimensional mass-spring structures", *Journal of Sound and Vibration*, Vol. 266, No. 5, pp. 1053–1078, 2003.

22. Liu, L. and M. I. Hussein, "Wave motion in periodic flexural beams and characterization of the transition between Bragg scattering and local resonance", *Journal of Applied Mechanics*, Vol. 79, No. 1, p. 011003, 2012.

23. Zhang, X., Z. Liu, and Y. Liu, "The optimum elastic wave band gaps in three dimensional phononic crystals with local resonance", *The European Physical Journal B*, Vol. 42, No. 4, pp. 477–482, 2004.

24. Economou, E. and M. Sigalas, "Stop bands for elastic waves in periodic composite materials", *The Journal of the Acoustical Society of America*, Vol. 95, No. 4, pp. 1734–1740, 1994.

25. Sprik, R. and G. Wegdam, "Acoustic band gaps in composites of solids and viscous liquids", *Solid State Communications*, Vol. 106, No. 2, pp. 77–81, 1998.

26. Kushwaha, M., B. Djafari-Rouhani, L. Dobrzynski, and J. Vasseur, "Sonic stop-bands for cubic arrays of rigid inclusions in air", *The European Physical Journal B*, Vol. 3, No. 2, pp. 155–161, 1998.

27. Suzuki, T. and P. K. Yu, "Complex elastic wave band structures in three-dimensional periodic elastic media", *Journal of the Mechanics and Physics of Solids*, Vol. 46, No. 1, pp. 115–138, 1998.

28. Sainidou, R., N. Stefanou, and A. Modinos, "Formation of absolute frequency gaps in three-dimensional solid phononic crystals", *Physical Review B*, Vol. 66, No. 21, p. 212301, 2002.

29. Wang, Y., F. Li, K. Kishimoto, Y. Wang, and W. Huang, "Wave band gaps in three-dimensional periodic piezoelectric structures", *Mechanics Research Communications*, Vol. 36, No. 4, pp. 461–468, 2009.

30. Liu, Z., C. Chan, P. Sheng, A. Goertzen, and J. Page, "Elastic wave scattering by periodic structures of spherical objects: Theory and experiment", *Physical Review B*, Vol. 62, No. 4, pp. 2446–2457, 2000.

31. Wang, Y., F. Li, K. Kishimoto, Y. Wang, and W. Huang, "Band gaps of elastic waves in three-dimensional piezoelectric phononic crystals with initial stress", *European Journal of Mechanics-A*, Vol. 29, No. 2, pp. 182–189, 2010.

32. Kafesaki, M., M. Sigalas, and E. Economou, "Elastic wave band gaps in 3-D periodic polymer matrix composites", *Solid State Communications*, Vol. 96, No. 5, pp. 285–289, 1995.

33. Hsieh, P., T. Wu, and J. Sun, "Three-dimensional phononic band gap calculations using the FDTD method and a PC cluster system", *IEEE Transactions on Ultrasonics, Ferroelectrics and Frequency Control*, Vol. 53, No. 1, pp. 148–158, 2006.

34. Zhang, X., Z. Liu, Y. Liu, and F. Wu, "Elastic wave band gaps for three-

dimensional phononic crystals with two structural units", *Physics Letters A*, Vol. 313, No. 5, pp. 455–460, 2003.

35. Davis, B. L. and M. I. Hussein, "A three-dimensional lumped parameter model of nanoscale phononiccrystals", *Proceedings of ASME DETC2009*, Vol. 1, pp. 285–290, 2009.

36. Liu, Z., X. Zhang, Y. Mao, Y. Zhu, Z. Yang, C. Chan, and P. Sheng, "Locally resonant sonic materials", *Science*, Vol. 289, No. 5485, pp. 1734–1736, 2000.

37. Hornreich, R., M. Kugler, S. Shtrikman, and C. Sommers, "Phonon band gaps", *Journal de Physique I*, Vol. 7, No. 3, pp. 509–519, 1997.

38. Lu, Z., J. A. Murakowski, C. A. Schuetz, S. Shi, G. J. Schneider, and D. W. Prather, "Three-dimensional subwavelength imaging by a photonic-crystal flat lens using negative refraction at microwave frequencies", *Physical review letters*, Vol. 95, No. 15, p. 153901, 2005.

39. Liu, Z., C. Chan, and P. Sheng, "Three-component elastic wave band-gap material", *Physical Review B*, Vol. 65, No. 16, p. 165116, 2002.

40. Goffaux, C. and J. Sánchez-Dehesa, "Two-dimensional phononic crystals studied using a variational method: Application to lattices of locally resonant materials", *Physical Review B*, Vol. 67, No. 14, p. 144301, 2003.

41. Gang, W., S. Li-Hui, L. Yao-Zong, and W. Ji-Hong, "Accurate evaluation of lowest band gaps in ternary locally resonant phononic crystals", *Chinese Physics*, Vol. 15, No. 8, p. 1843, 2006.

42. Hirsekorn, M., P. Delsanto, N. Batra, and P. Matic, "Modelling and simulation of acoustic wave propagation in locally resonant sonic materials", *Ultrasonics*, Vol. 42, No. 1, pp. 231–235, 2004.

43. Wang, G., X. Wen, J. Wen, L. Shao, and Y. Liu, "Two-dimensional locally resonant

phononic crystals with binary structures", *Physical Review Letters*, Vol. 93, No. 15, p. 154302, 2004.

44. Zhu, R., X. Liu, G. Hu, C. Sun, and G. Huang, "A chiral elastic metamaterial beam for broadband vibration suppression", *Journal of Sound and Vibration*, Vol. 333, No. 10, pp. 2759–2773, 2014.

45. Baravelli, E. and M. Ruzzene, "Internally resonating lattices for bandgap generation and low-frequency vibration control", *Journal of Sound and Vibration*, Vol. 332, No. 25, pp. 6562–6579, 2013.

46. Acar, G. and C. Yilmaz, "Experimental and numerical evidence for the existence of wide and deep phononic gaps induced by inertial amplification in two-dimensional solid structures", *Journal of Sound and Vibration*, Vol. 332, No. 24, pp. 6389–6404, 2013.

47. Taniker, S. and C. Yilmaz, "Phononic gaps induced by inertial amplification in BCC and FCC lattices", *Physics Letters A*, Vol. 377, No. 31, pp. 1930–1936, 2013.

48. Taniker, S. and C. Yilmaz, "Inertial amplification induced phononic band gaps in SC and BCC lattices", *International Mechanical Engineering Congress & Exposition ASME-IMECE, San Diego, CA*, 2013.

49. Mennitto, G. and M. Buehler, "CARL: A compliant articulated robot leg for dynamic locomotion", *Robotics and Autonomous Systems*, Vol. 18, No. 3, pp. 337–344, 1996.

50. Pollard, A., "The mechanical amplification of small displacements", *Journal of Scientific Instruments*, Vol. 15, p. 37, 1938.

51. Jacobsen, S., "Rotary-to-linear and linear-to-rotary motion converters", February 11 1975, US Patent 3,864,983.

52. Bettini, P., A. Airoldi, G. Sala, L. Di Landro, M. Ruzzene, and A. Spadoni, "Com-

posite chiral structures for morphing airfoils: Numerical analyses and development of a manufacturing process", *Composites Part B: Engineering*, Vol. 41, No. 2, pp. 133–147, 2010.

53. Tee, K., A. Spadoni, F. Scarpa, and M. Ruzzene, "Vibroacoustics and wave propagation of novel chiral honeycombs", *Proceedings of the Society of Photo-Optical Instrumentation Engineers*, Vol. 6928, pp. 69280J–1, 2008.

54. Li, J., Y. Wang, and C. Zhang, "Finite element method for analysis of band structures of three dimensonal phononic crystals", *Ultrasonics Symposium, 2008. IUS 2008. IEEE*, pp. 1468–1471, IEEE, 2008.

55. Tanaka, Y., S. Tamura, A. Akimov, A. Pevtsov, S. Kaplan, A. Dukin, V. Golubev, D. Yakovlev, and M. Bayer, "Phononic properties of opals", *Journal of Physics: Conference Series*, Vol. 92, p. 012107, IOP Publishing, 2007.

56. Kohrs, T. and B. Petersson, "Wave propagation in light weight profiles with truss-like cores: Wavenumber content, forced response and influence of periodicity perturbations", *Journal of sound and vibration*, Vol. 304, No. 3-5, pp. 691–721, 2007.

57. Hutchinson, R. and N. Fleck, "The structural performance of the periodic truss", *Journal of the Mechanics and Physics of Solids*, Vol. 54, No. 4, pp. 756–782, 2006.

58. El-Raheb, M., "Frequency response of a two-dimensional trusslike periodic panel", *The Journal of the Acoustical Society of America*, Vol. 101, p. 3457, 1997.

59. Abu-Saba, E., W. McGinley, and R. Montgomery, "Dynamic Analysis of Truss-Beam System", *Journal of Aerospace Engineering*, Vol. 4, No. 4, pp. 347–354, 1991.

60. Sheng, Y. and J. Gong, "Modeling and experimental modal analysis of active truss structure", *Electric Information and Control Engineering (ICEICE), 2011 International Conference on*, pp. 2338–2342, IEEE, 2011.

61. Kittel, C., *Introduction to Solid State Physics*, John Wiley & Sons, Inc., New York, 8th edition, 2005.

62. Brillouin, L., *Wave Propagation and Group Velocity*, Academic Press, New York, 1960.

63. Brillouin, L., *Wave Propagation in Periodic Structures*, McGraw-Hill, New York, 1946.

64. Chen, J. J., H. L. W. Chan, and J. C. Cheng, "Large one-dimensional band gaps in three-component phononic crystals plates", *Physics Letters A*, Vol. 366, No. 4, pp. 493–496, 2007.

65. Bilal, O. R. and M. I. Hussein, "Ultrawide phononic band gap for combined in-plane and out-of-plane waves", *Physical Review E*, Vol. 84, No. 6, p. 065701, 2011.

66. Williams, A. and F. J. Taylor, *Electronic Filter Design Handbook*, McGraw-Hill Professional, NY, USA, 2006.

67. Ewins, D. J., *Modal Testing: Theory and Practice*, Research Studies Press, Baldock, 2000.